

Stephen F. Austin State University

SFA ScholarWorks

Electronic Theses and Dissertations

12-2016

Characterization and Delineation of Karst Geohazards Along RM652 Using Electrical Resistivity Tomography, Culberson County, Texas

Adam F. Majzoub

Stephen F Austin State University, adam.majzoub@gmail.com

Follow this and additional works at: <https://scholarworks.sfasu.edu/etds>



Part of the [Construction Engineering and Management Commons](#), [Environmental Engineering Commons](#), [Environmental Indicators and Impact Assessment Commons](#), [Environmental Monitoring Commons](#), [Geology Commons](#), [Geomorphology Commons](#), [Geophysics and Seismology Commons](#), [Geotechnical Engineering Commons](#), [Hydrology Commons](#), [Other Earth Sciences Commons](#), [Sedimentology Commons](#), [Speleology Commons](#), and the [Tectonics and Structure Commons](#)

Tell us how this article helped you.

Repository Citation

Majzoub, Adam F., "Characterization and Delineation of Karst Geohazards Along RM652 Using Electrical Resistivity Tomography, Culberson County, Texas" (2016). *Electronic Theses and Dissertations*. 50.
<https://scholarworks.sfasu.edu/etds/50>

This Thesis is brought to you for free and open access by SFA ScholarWorks. It has been accepted for inclusion in Electronic Theses and Dissertations by an authorized administrator of SFA ScholarWorks. For more information, please contact cdsscholarworks@sfasu.edu.

Characterization and Delineation of Karst Geohazards Along RM652 Using Electrical Resistivity Tomography, Culberson County, Texas

Creative Commons License



This work is licensed under a [Creative Commons Attribution-Noncommercial-No Derivative Works 4.0 License](https://creativecommons.org/licenses/by-nc-nd/4.0/).

**Characterization and Delineation of Karst Geohazards Along RM652 Using
Electrical Resistivity Tomography, Culberson County, Texas**

By

Adam Majzoub, Bachelor of Science

Presented to the Faculty of the Graduate School of
Stephen F. Austin State University
In Partial Fulfillment
Of the requirements

For the Degree of
Master of Science

STEPHEN F. AUSTIN STATE UNIVERSITY

December 2016

**Characterization and Delineation of Karst Geohazards Along RM652 Using
Electrical Resistivity Tomography, Culberson County, Texas**

By

Adam Majzoub, Bachelor of Science

APPROVED:

Dr. Wesley Brown, Thesis Director

Dr. Kevin Stafford, Committee Member

Dr. Melinda Faulkner, Committee Member

Dr. Joseph Musser, Committee Member

Richard Berry, D.M.A
Dean of the Graduate School

ABSTRACT

The Delaware Basin of West Texas and southeastern New Mexico is the major western subdivision of the Permian Basin and a northern extension of the Chihuahuan Desert. The major evaporite unit within the Delaware Basin is the Castile Formation, which consists of gypsum/anhydrite and is highly susceptible to dissolution and karsting. Manifestations of karst within the Castile outcrop are abundant and include sinkholes, subsidence features and caves, both epigene and hypogene in origin.

Land reconnaissance surveys conducted during the summer of 2015 documented abundant karst landforms in close proximity to a major thoroughfare, RM 652, in Culberson County, Texas. 2D electrical resistivity surveys were conducted at sixteen sites to characterize and delineate karst related hazards, both laterally and vertically, associated with the road. Data was collected with a SuperSting (R8/IP) multi-electrode earth resistivity meter with a dipole-dipole array type. Resistivity data collected was processed using EarthImager 2D to produce inverted profile sections of each site. Two dimensional electrical resistivity tomography was shown to be effective in detecting karst features in the shallow subsurface within the study area.

ACKNOWLEDGEMENTS

I take this opportunity to express my appreciation to the many people who made my work on this thesis possible. First of all, I thank my advisors, Dr. Kevin Stafford and Dr. Wesley Brown, who were unfailingly supportive of my endeavors and provided excellent guidance. I am also sincerely grateful to all committee members who oversaw this work. I give special thanks to Dr. I-Kuai Hung of the Forestry Department at Stephen F. Austin State University for his invaluable input.

I am also grateful for the comradery and efforts of the other students that I was privileged to work with Jon Ehrhart, Jessica Shields, and Ingrid Eckhoff.

Finally, I am profoundly thankful for the constant encouragement I received from my parents, Fayez and Deborah Majzoub, my four sisters and my lifelong friend, Eric Thorn. Thank you all.

TABLE OF CONTENTS

ABSTRACT.....	i
ACKNOWLEDGEMENTS.....	ii
TABLE OF CONTENTS	iii
LIST OF FIGURES.....	v
LIST OF APPENDIX FIGURES.....	vii
LIST OF EQUATIONS.....	xii
LIST OF TABLES.....	xiii
PREFACE	xiv
CHARACTERIZATION AND DELINEATION OF GYPSUM KARST GEOHAZARDS USING 2-D ELECTRICAL RESISTIVITY TOMOGRAPHY IN CULBERSON COUNTY, TEXAS, USA.....	
ABSTRACT.....	1
INTRODUCTION.....	2
GEOLOGIC SETTING.....	5
ELECTRICAL RESISTIVITY METHODS.....	8
SITE ANALYSES AND INTERPRETATIONS.....	12
SITE 1 (110-METER SURVEY).....	12
SITE 2.....	14
SITE 3.....	15

SITE 4.....	19
SITE 1 (220-METER SURVEY).....	19
KARST PROCESSES DELINEATED BY RESISTIVITY ANALYSES.....	22
CONCLUSIONS.....	25
ACKNOWLEDGEMENTS.....	27
REFERENCES.....	28
APPENDIX (A) LITERATURE REVIEW.....	30
INTRODUCTION.....	31
STRUCTURAL HISTORY OF THE DELAWARE BASIN.....	35
STRATIGRAPHY.....	39
GUADALUPIAN STRATIGRAPHY.....	40
OCHOAN STATIGRAPHY.....	43
KARST OF THE DELAWARE BASIN.....	46
RESISTIVITY.....	53
REFERENCES.....	62
APPENDIX (B) METHODOLOGY.....	66
METHODS.....	67
REFERENCES.....	82
APPENDIX (C) RESULTS AND SITE DESCRIPTIONS.....	83
VITA	106

LIST OF FIGURES

Figure 1: Map of study area showing geographic relationship of the Delaware Basin to Texas with major features of geologic in the region. Study area in upper figure is enlarged as a simplified geology map in the lower portion. Circled features 1, 2, 3 and 4 correlate with location of resistivity *Site 1*, *Site 2*, *Site 3* and *Site 4*, respectively..... 3

Figure 2. A) Schematic showing layout configuration of each survey conducted. Four cable sections were used with 56 electrodes at each survey site. B) Schematic showing configuration for dipole-dipole array with four electrodes. k represents the geometric factor, C1 and C2 are current electrodes, P1 and P2 are potential electrodes and a represents the electrode spacings..... 9

Figure 3: A) *Site 1* inverted and interpreted inverted section (dipole-dipole array, 56 electrodes at 2-meter spacing with total survey length of 110 meters). RMS error= 5.73%, L2 norm= 0.70, iteration= 5. Scale = 1:1; B) *Site 2* inverted and interpreted inverted section (dipole-dipole array, 56 electrodes at 2-meter spacing with total survey length is 110 meters). RMS error= 4.63%, L2 norm= 0.76, iteration= 4. Scale=1:1..... 13

Figure 4: A) *Site 1*. LiDAR images showing location of cave entrances proximal to survey site. B: *Site 2* LiDAR image showing proximal entrenched arroyo. Dashed lines represent approximate location of electrical resistivity surveys..... 14

Figure 5 A) *Site 3* inverted section and interpreted inverted section (dipole-dipole array, 56 electrodes roll-along survey at 1-meter spacing). RMS error= 7.39%, L2 norm= 0.80, iteration= 6, Scale= 1:1; B) *Site 4* inverted section and interpreted section (dipole-dipole array, 56 electrodes roll-along survey at 1-meter spacing). RMS error= 8.99%, L2 norm= 0.85, iteration= 8, Scale=1:1. 16

Figure 6. A) LiDAR image of *Site 3* with multiple cave entrances observed and documented on the surface with conduits trending laterally underneath the road. B) LiDAR image of *Site 4* with highly fractured gypsum bedrock on surface. Dashed lines represent approximate survey locations..... 17

Figure 7: Aerial photo showing extent of surveyed caves (solid white fills) and surface lineaments (dashed white lines) that represent near-vertical fractures at survey *Site 3*..... 18

Figure 8: *Site 1* inverted and interpreted inverted ERT profile (dipole-dipole array, 56 electrodes at 4-meter electrode spacing). RMS error= 6.88%, L2 norm= 0.90. Iteration= 7. Scale= 1:1 20

LIST OF APPENDIX FIGURES

Figure A1. Map of study area and surrounding counties.	31
Figure A2. Location of study area showing outcrops of Castile and Rustler formations. (from Stafford 2008c).	33
Figure A3. Stratigraphic section from north to south through the Delaware basin showing the major units in the study area (from Stafford 2015, adapted from Scholle et al., 2004).....	41
Figure A4. Density map showing the spatial distribution of karst manifestations of the Castile Formation in the study area (from Stafford et al., 2008b).....	47
Figure A5. Diagrammatic depiction of the formation of breccia pipes. Dark arrows represent upward movement of low density undersaturated fluids and light colored arrows represent the descending high density oversaturated fluids (from Stafford, 2015).	50
Figure A6. Diagrammatic representation of formation of blanket zones of breccia through intrastratal dissolution of halite layers (from Stafford, 2015)	51
Figure A7. Simplified diagram of electrode placement in a 2-D resistivity survey and current flow paths (from Musset and Khan, 2000)	55
Figure A8. Common array configurations and corresponding geometric factors. C is the current electrode and P is the potential electrode. Current travels from the C electrode and resistivity is measured by the P electrode (from Mussett and Khan, 2000).....	56
Figure A9. Contour plot showing resistivity sensitivity changes between electrode pairs in a dipole-dipole array (from Loke, 1999).	58
Figure A10. Inverted sections from resistivity survey conducted along interstate 70 in Frederick County, Maryland. Sections show the three common array configurations. Dipole-dipole array was determined to be the most effective in characterizing the sinkhole in the area (from Zhou et al., 2002).....	60
Figure B1: Map of study area and approximate locations of each resistivity survey.....	68

Figure B2: Super Sting R8 resistivity meter produced by Advanced Geosciences. Image shows the SuperSting console, switchbox, and marine batteries for power supply. Cables are connected to electrodes along a survey line (not shown).....	68
Figure B3: Parameters for dipole-dipole survey set with the command file creator option in Advanced Geosciences administrator software. Image shows a simulated version of survey data collected with the given parameters.	70
Figure B4: Simplified electrode configuration for dipole-dipole array. k represents the geometric factor. Where “ n ” is the distance ratio between dipole separation, and “ a ” is the spacing between transmitting and receiving electrodes.....	71
Figure B5: Schematic of in field survey setup. Resistivity meter and switchbox were placed at the low address section. The switchbox, produced by Advanced Geosciences, allows for positioning of resistivity meter at the low address section rather than middle of survey.....	72
Figure B6: Annotated photo of in field 56-electrode setup along survey site.....	73
Figure B7: Schematic of roll-along survey. Figure shows advancement at 25 percent or one quarter of survey length. In this study, roll-along was advanced 50 percent or half the survey length. <i>Image modified from</i> (AGI, 2016).....	74
Figure B8: Schematic of survey with 50 percent overlap at site <i>Res16_P13</i> . Total length is 220 meters at 2-meter electrode spacing.....	75
Figure B9: Initial settings from EarthImager 2D. All criteria and parameters for inversion are set to default <i>Surface</i> settings which is recommended for most resistivity data.....	77
Figure B10: Image shows inversion settings for all data collected in this study. All settings are default <i>surface</i> settings in Earth Imager.	78
Figure B11: Data misfit histogram for site <i>Res16_P13</i> . Image taken from EarthImager 2D inversion software. Blue vertical line is adjustable and marks the threshold of data misfit removal.....	79
Figure B12: Data misfit cross plot for site <i>Res16_P13</i> . Data points are plotted along a best fit line which is the predicted apparent resistivity ‘y-axis’ versus the measured apparent resistivity ‘x-axis’.....	80

Figure B13: Terrain file for site <i>Res16</i> . Elevation data was extracted from DEM of study area in ArcGIS. Tape measurement locations of each electrode were inputted (2-meter increments) followed by approximate elevation in meters from DEM.....	81
Figure C1: Map of study area showing approximate location of each resistivity survey site.....	84
Figure C2: Survey site P 30. 56 electrode dipole-dipole array with 2-meter spacing (total length 112 meters). Note that maximum resistivity reading in inverted sections is 1560 ohm-m. RMS error 3.01%.....	85
Figure C3: Survey site P 31. 56 electrode dipole-dipole array with 2-meter spacing (total length 112 meters). Note that maximum resistivity reading in inverted sections is 780 ohm-m. RMS error 2.69%.....	86
Figure C4: Survey site Res8_P23. 56 electrode dipole-dipole array roll-along survey with 1-meter spacing (total length 196 meters). Note that maximum resistivity reading in inverted sections is 100k ohm-m. RMS error 9.52%.....	87
Figure C5: Survey site Res8_P23. 56 electrode dipole-dipole array with 4-meter spacing (total length 224 meters). Note that maximum resistivity reading in inverted sections is 100k ohm-m. RMS error 6.41%.....	88
Figure C6: Survey site Res14_P22. 56 electrode dipole-dipole array with 2-meter spacing (total length 112 meters). Note that maximum resistivity reading in inverted sections is 100k ohm-m. RMS error 4.95%.....	89
Figure C7: Survey site P21. 56 electrode dipole-dipole array with 2-meter spacing (total length 112 meters). Note that maximum resistivity reading in inverted sections is 100k ohm-m. RMS error 6.31%.....	90
Figure C8: Survey site Res1_Tree. 56 electrode dipole-dipole array with 2-meter spacing (total length 112 meters). Note that maximum resistivity reading in inverted sections is 100k ohm-m. RMS error 4.62%	91
Figure C9: Survey site Res1_Tree. 56 electrode dipole-dipole array with 4-meter spacing (total length 224 meters). Note that maximum resistivity reading in inverted sections is 100k ohm-m. RMS error 4.78%.....	92

Figure C10: Survey site Res18_P17. 56 electrode dipole-dipole array with 2-meter spacing (total length 112 meters). Note that maximum resistivity reading in inverted sections is 100k ohm-m. RMS error 5.20%	93
Figure C11: Survey site Res2. 56 electrode dipole-dipole array roll-along survey with 1-meter spacing (total length 112 meters). Note that maximum resistivity reading in inverted sections is 100k ohm-m. RMS error 6.64%	94
Figure C12: Survey site Res2. 56 electrode dipole-dipole array with 4-meter spacing (total length 224 meters). Note that maximum resistivity reading in inverted sections is 100k ohm-m. RMS error 8.39%	95
Figure C13: Survey site Res6_P16. 56 electrode dipole-dipole array with 4-meter spacing (total length 224 meters). Note that maximum resistivity reading in inverted sections is 100k ohm-m. RMS error 14.15%	96
Figure C14: Survey site Res16_P13. 56 electrode dipole-dipole array with 2-meter spacing (total length 112 meters). Note that maximum resistivity reading in inverted sections is 1000 ohm-m. RMS error 3.43%	97
Figure C15: Survey site Res16_P13. 56 electrode dipole-dipole array with 2-meter spacing (total length 112 meters). Note that maximum resistivity reading in inverted sections is 1000 ohm-m. RMS error 3.50%	98
Figure C16: Survey site Res15_P11. 56 electrode dipole-dipole array with 2-meter spacing (total length 112 meters). Note that maximum resistivity reading in inverted sections is 78,044 ohm-m. RMS error 3.72%	99
Figure C17: Survey site Res12_P10. 56 electrode dipole-dipole array with 4-meter spacing (total length 224 meters). Note that maximum resistivity reading in inverted sections is 100k ohm-m. RMS error 4.44%.....	100
Figure C18: Survey site Res5b_P09. 56 electrode dipole-dipole array with 2-meter spacing (total length 112 meters). Note that maximum resistivity reading in inverted sections is 100k ohm-m. RMS error 4.02%	101
Figure C19: Survey site Res5b_P09. 56 electrode dipole-dipole array with 4-meter spacing (total length 224 meters). Note that maximum resistivity reading in inverted sections is 100k ohm-m. RMS error 6.96%. Survey conducted in eastbound lane.....	102

Figure C20: Survey site Res7_P04. 56 electrode dipole-dipole array with 2-meter spacing (total length 112 meters). Note that maximum resistivity reading in inverted sections is 36.624 ohm-m. RMS error 2.87%103

Figure C21: Survey site Res4a_P02. 56 electrode dipole-dipole array with 4-meter spacing (total length 224 meters). Note that maximum resistivity reading in inverted sections is 88,187 ohm-m. RMS error 3.36%104

Figure C22: Survey site Res4_P01. 56 electrode dipole-dipole array with 2-meter spacing (total length 112 meters). Note that maximum resistivity reading in inverted sections is 2,907 ohm-m. RMS error 3.88% 105

LIST OF EQUATIONS

Equation 1: $k = n(n+1)(n+2) a$	8
Equation A1: $\frac{\text{Potential or voltage difference (volts)}}{\text{current (amps)}} = \frac{V}{I} = \text{resistance } R \text{ (ohms } \Omega)$	54
Equation A2a: resistance, $R = \text{resistivity } (\rho) \times \frac{\text{length}}{\text{area of cross-section}}$	54
Equation A2b: resistivity, $\rho = \text{resistance} \times \frac{\text{area of cross-section}}{\text{length}}$	54

LIST OF TABLES

Table B1: Survey sites and field parameters..... 69

PREFACE

The Gypsum Plain of the Delaware Basin in west Texas and southeastern New Mexico is a region that has undergone significant karsting. The high solution potential of gypsum along with the complex hydrogeologic system in the study area makes predicting and assessing karst geohazards a difficult task without the aid of near surface geophysical tools. This paper is part of an interdisciplinary study by the Geology Department at Stephen F. Austin State University to characterize and delineate subsurface karst features associated with roadway and infrastructure geohazard. In this study, electrical resistivity tomography was the chosen method to achieve this.

Land traverse surveys were conducted in the summer of 2015 at the request of the Texas Department of Transportation to document surficial karst features that were either directly or indirectly responsible for the continuous road failures that were occurring along Ranch to Market 652. A total of 16 sites were selected for resistivity imaging with data collection conducted during the spring and summer of 2016.

In addition to the following manuscript are appendices which contain additional supporting information, although not specifically referenced in the main manuscript. Appendix A includes a detailed literature review of the geologic setting of the study area. Appendix B presents a detailed discussion of the theory and methodologies incorporated in this study. Appendix C includes all data collected, processed and analyzed in this study.

Characterization and Delineation of Gypsum Karst Geohazards Using 2-D Electrical Resistivity Tomography in Culberson County, Texas, USA

ABSTRACT

The Delaware Basin of West Texas and southeastern New Mexico is the major western subdivision of the Permian Basin and a northern extension of the Chihuahuan Desert. The major evaporite unit within the Delaware Basin is the Castile Formation, which consists of gypsum/anhydrite and is highly susceptible to dissolution and karsting. Manifestations of karst within the Castile outcrop are abundant and include sinkholes, subsidence features and caves, both epigene and hypogene in origin.

Land reconnaissance surveys conducted during 2015 and 2016 documented abundant karst landforms in close proximity to major thoroughfares in Culberson County, Texas. Two dimensional (2D) electrical resistivity surveys were conducted at four sites to characterize and delineate karst related hazards, both laterally and vertically, associated with the road. Data was collected with a SuperSting (R8/IP) multi-electrode earth resistivity meter with a dipole-dipole array configuration. Resistivity data collected was processed using EarthImager 2D to produce inverted profile sections of each site. Two dimensional electrical resistivity tomography was shown to be effective in detecting karst features and geo-hazards in the shallow subsurface within the study area.

INTRODUCTION

The Delaware Basin of West Texas and southeastern New Mexico is the northern most extension of the Chihuahuan desert and is commonly referred to as the Gypsum Plain (Hill, 1996). The study area lies in the northwestern edge of Culberson County, Texas within the Delaware Basin (Figure 1). The major evaporite facies exposed is the Permian Castile Formation, with minor exposure of the Salado and Rustler evaporites / carbonates in the east. Widespread evaporite karst development and associated geo-hazards are common within the Castile Formation outcrop region and are often expressed as sinkholes, subsidence features, and caves with polygenetic origins (Stafford et al., 2008a).

A variety of geophysical methods have long been used to characterize the deep subsurface. Electrical resistivity imaging has been widely and successfully used for geotechnical site investigations to characterize shallow geo-hazard features in various geological settings (e.g. Zhou et al, 2002; Niederleithinger et al., 2012; Metwaly and AlFouzan, 2013; Benson and Yuhr, 2015). Data collected is often displayed as 2-D or 3-D models that show subsurface resistivity distribution.

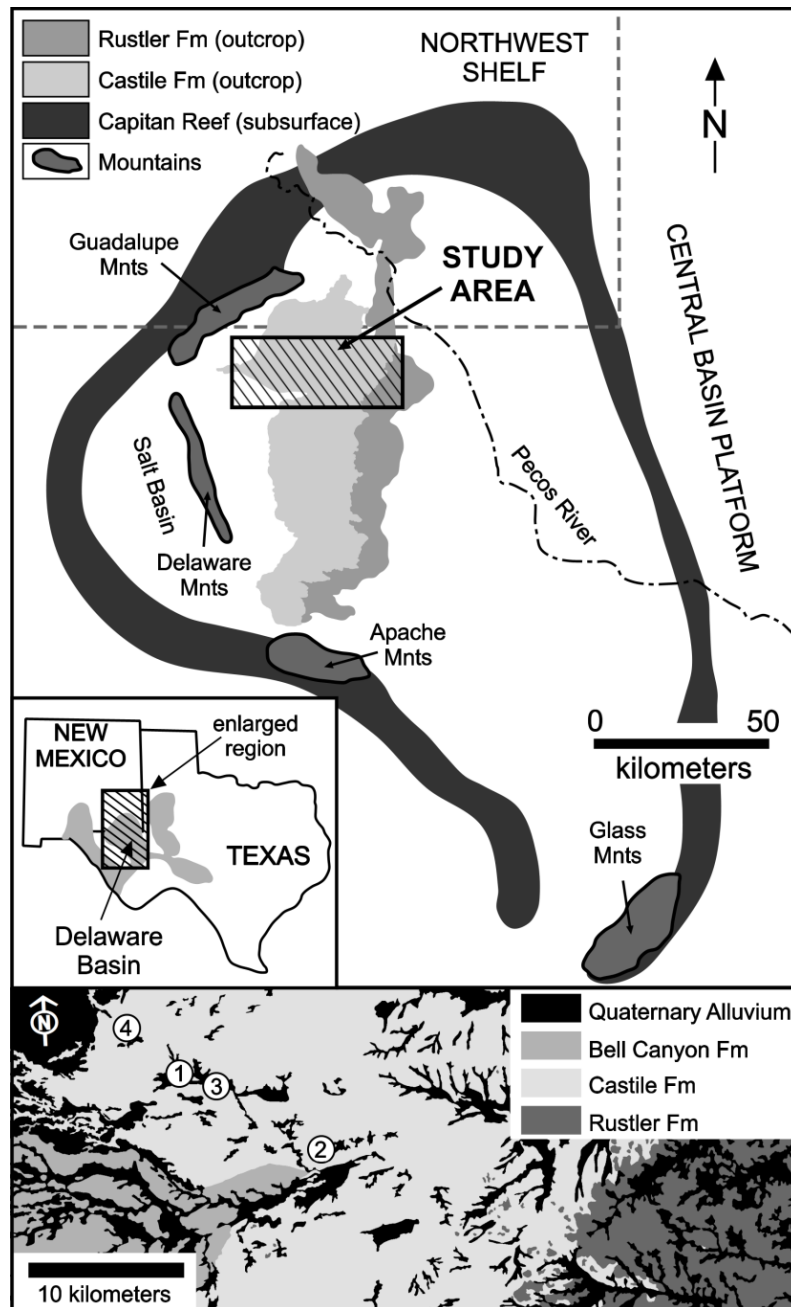


Figure 1. Map of study area showing geographic relationship of the Delaware Basin to Texas with major features of geologic interest in the region. Study area in upper figure is enlarged as a simplified geologic map in the lower portion. Circled features 1, 2, 3 and 4 correlate with location of resistivity *Site 1*, *Site 2*, *Site 3* and *Site 4*, respectively.

Land reconnaissance of the study area revealed several sites of probable karst related geo-hazards along major thoroughfares in Culberson County, Texas. Multi-electrode surveys were conducted at a total of 20 separate sites with multiple instrument configurations at each site. Four selected sites are presented in this paper as examples of the usefulness of Direct Current (DC) resistivity imaging in geo-hazard detection in gypsum karst.

GEOLOGIC SETTING

The Delaware Basin of west Texas and northeastern New Mexico is classified as an evaporite intracratonic basin outlined by a 600-700 kilometer chain of Capitan Limestone that crops out as the Guadalupe Mountains to the northwest and the Apache Mountains to the west and south, respectively (Hill, 1996). Assimilation of Pangea during Late Mississippian and Early Permian resulted in block faulting along Precambrian zones of weakness creating structural separations of the Permian Basin into the Central Basin Platform, Midland Basin and Delaware Basin. Sediment infill and subsidence along high angle faults of the Delaware Basin dominated throughout the Paleozoic including formation of a major carbonate reef around the periphery (Horak, 1985). By Late Guadalupian and into the Early Ochoan, extensive reef development encircled the basin and restricted the flow of marine waters creating a deep saline lake and conditions ideal for Castile evaporite deposition (Kirkland, 2003). Subsequent deposition of Salado and Rustler formations capped the region and surrounding basin (Scholle et al., 2004).

Tectonic activity during the Early Mesozoic had minimal effect on the Delaware Basin; however, Laramide tectonism during the Late Mesozoic and Early Cenozoic produced regional tilting and uplift of the basin strata (3-5°) to the east/northeast. Effects of Basin and Range extension in the study area are limited to near vertical conjugate

joint/fault sets formed in the early Neogene that are oriented at ~N75°E and ~N15°W (Horak, 1985, Hentz and Henry, 1989).

The Delaware Basin experienced vast fluctuations in climate during the Pleistocene from wet and cold to dry and warm during glacial and interglacial periods; intermittent periods of heavy stream erosion during glacial melt and karst processes sculpted the modern landscape. Within the last 10,000 years, climate has transitioned the Delaware Basin into an arid to semiarid desert (Hill, 1996). Today the average precipitation ranges from 15-40 cm with an average annual temperature of 24°C and average summertime high of 40°C.

Karst Development

The high solubility of Castile evaporite rocks has resulted dramatic karst development throughout the Gypsum Plain. Minor karst occurs in less soluble and predominantly carbonate Rustler strata, while the halite rich Salado Formation has been largely removed in outcrop and shallow subcrop by intrastratal dissolution creating a solutional contact boundary between the Castile and Rustler formations (Stafford et al., 2008a).

Surficial karst manifestations within the Castile Formation crop out across 1800 square kilometers of the Gypsum Plain as sinkholes, subsidence features, fractures and

caves. Solutional caves are attributed to both hypogene and epigene speleogenesis (Stafford et al., 2008a), with hypogene caves formed by dissolution from rising fluids driven by differences in hydraulic pressure gradients within semi-confined strata and epigene caves formed by gravitationally driven water in unconfined strata (Palmer, 2006). Dense clusters of hypogene caves are found in the western portion of the study area where surface denudation has breached them. Epigene caves form by near-surface meteoric processes and are widespread throughout the Gypsum Plain but are often expressed as isolated features associated with collapsed and filled sinkholes (Stafford et al., 2008a).

Gypsite soil caves or suffosion caves are often coupled with epigene caves in the subsurface within the study area. Suffosion is commonly associated with the formation of sinkholes or doline structures where unconsolidated clastic material is transported or washed into the subsurface leaving behind a void (Palmer, 2006). In the study area, suffosion caves form by the transport of the insoluble fraction of gypsic soils which form a cover of variable thickness across the region. Dissolution of the soluble fraction of the soils/sediments allows for the migration of the insoluble fraction into subsurface voids spaces or conduits formed by epigene processes (Stafford, 2008a).

ELECTRICAL RESISTIVITY METHODS

Two dimensional direct current (DC) resistivity surveys were conducted at four sites of interest, using an eight-channel SuperSting (R8/IP) multi-electrode earth resistivity meter, produced by Advanced Geosciences Inc. (AGI). All four sites were selected based on observable karst processes in close proximity to the road. Surveys were conducted using 56 electrodes and a dipole-dipole array configuration (Figure 2A and B).

Geometry of electrode configuration and the relative positions of transmitting and receiving dipoles were configured using AGI administrator software prior to data acquisition. The geometric factor k for the dipole-dipole array is given by:

$$k = \frac{\pi}{4} \frac{n(n+1)(n+2)}{a} \quad (1)$$

Where “ n ” is the distance ratio between dipole separation, and “ a ” is the spacing between transmitting and receiving electrodes (Loke, 1999) (Figure 2B). These parameters were set to a maximum of 6 for “ a ” spacing and maximum value of 8 for “ n ” and were applied uniformly to all surveys in this study. Deployment of these survey parameters were fully automated by the SuperSting resistivity meter; a feature that is common to modern day multi-electrode DC resistivity acquisition systems which reduces data acquisition time. Two surveys are reported in this study at Site 1; a 110-meter survey at 2-meter electrode

spacing was conducted first followed by a 220-meter survey at 4-meter electrode spacing. Site 2 was surveyed with 2-meter electrode spacing for a total survey

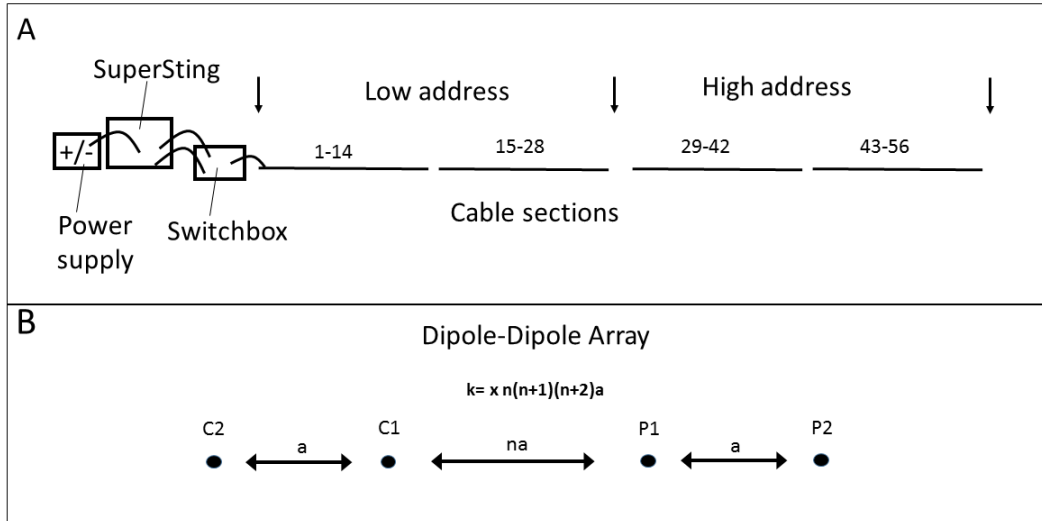


Figure 2. (A) Schematic showing layout configuration of each survey conducted. Four cable sections were used with 56 electrodes at each survey site. (B) Schematic showing configuration for dipole-dipole array with four electrodes. k represents the geometric factor, C1 and C2 are current electrodes, P1 and P2 are potential electrodes and a represents the electrode spacings.

length of 110-meters. Site 3 and Site 4 were surveyed with a 1-meter electrode spacing using the roll-along method with a total survey length of 111 meters each. The main advantage of using a roll-along method was to extend survey length while maintaining higher resolution at shallow depths. Depth of penetration and profile resolution is a function of electrode spacing; increases in electrode spacing will increase depth penetration, however, resolution of the shallow subsurface is decreased (Greenwood, 2016).

Prior to each measurement, electrodes were wetted with a dilute saline solution to improve electrical contact resistance with the ground. Given the arid conditions in the study area, some sites were abandoned when contact resistance could not be lowered to an acceptable level, typically less than 2000 Ω . Site specific parameters were configured directly on the SuperSting console, these included electrode spacing, measurement units (meters), and whether a roll-along survey would be conducted or not. For all surveys the measurement time was set to 1.2 seconds which was cycled twice at each electrode pair. The maximum error threshold between measurement cycles was set to 2% and injected current for each measurement was set to a maximum of 2000 mA.

All data acquired was processed with *EarthImager 2-D* inverse modeling software produced by Advanced Geosciences Inc. Pseudosections were inverted using smooth model inversion with L2 norm optimization. Noise associated with natural magnetotelluric currents were automatically removed from all data; this was accomplished by applying an estimated noise threshold of 3% prior to inversion. Additionally, misfit data were removed by utilizing a data misfit histogram after inversion was complete. This process allowed for more accurate models which represented true subsurface resistivity distribution at each site. Terrain corrections were applied to all data to better represent the topography within the survey area. This was accomplished by extracting elevation values from a digital elevation model created from LiDAR (Light Detection and Ranging) data of the study area and processed in ESRI ArcGIS. LiDAR horizontal resolution was acquired at 0.3-0.4 meters with 10 centimeters

vertical resolution. LiDAR images were analyzed at each site for karst delineation and extent to compliment resistivity data.

SITE ANALYSES AND INTERPRETATIONS

Site 1 (110-meter survey)

Survey of Site 1 was conducted in a northwest-southeast trending line with 56 electrodes at 2-meter spacing and a total line length of 110 meters (Figure 3A). Effective depth of penetration was 23 meters. This site is located in a topographically low region within the study area making this area more susceptible to overland flow during precipitation events. Overgrowth of vegetation on the surface is localized near the center of the survey line, around the 50-60 meter mark. The three zones of low resistivity (40-100 Ωm), noted by circular dashed lines at around 10 meters of depth, are interpreted to be solution conduits filled with moisture-rich gypsic soils transported from the surface. Dashed line across the entire profile indicates approximate bedrock boundary with lower profile of leached bedrock less saturated than the upper. A continuous zone of low resistivity in the northwest end of the survey at 5-6 meters in depth is a filled sinkhole.

Field verification via excavation in northwest end of the survey correlates well with the data shown on the resistivity profile as a thicker zone of gypsic soil. At depths of 15-20 meters, a gradually increasing zone of high resistivity represents fractured gypsum bedrock.

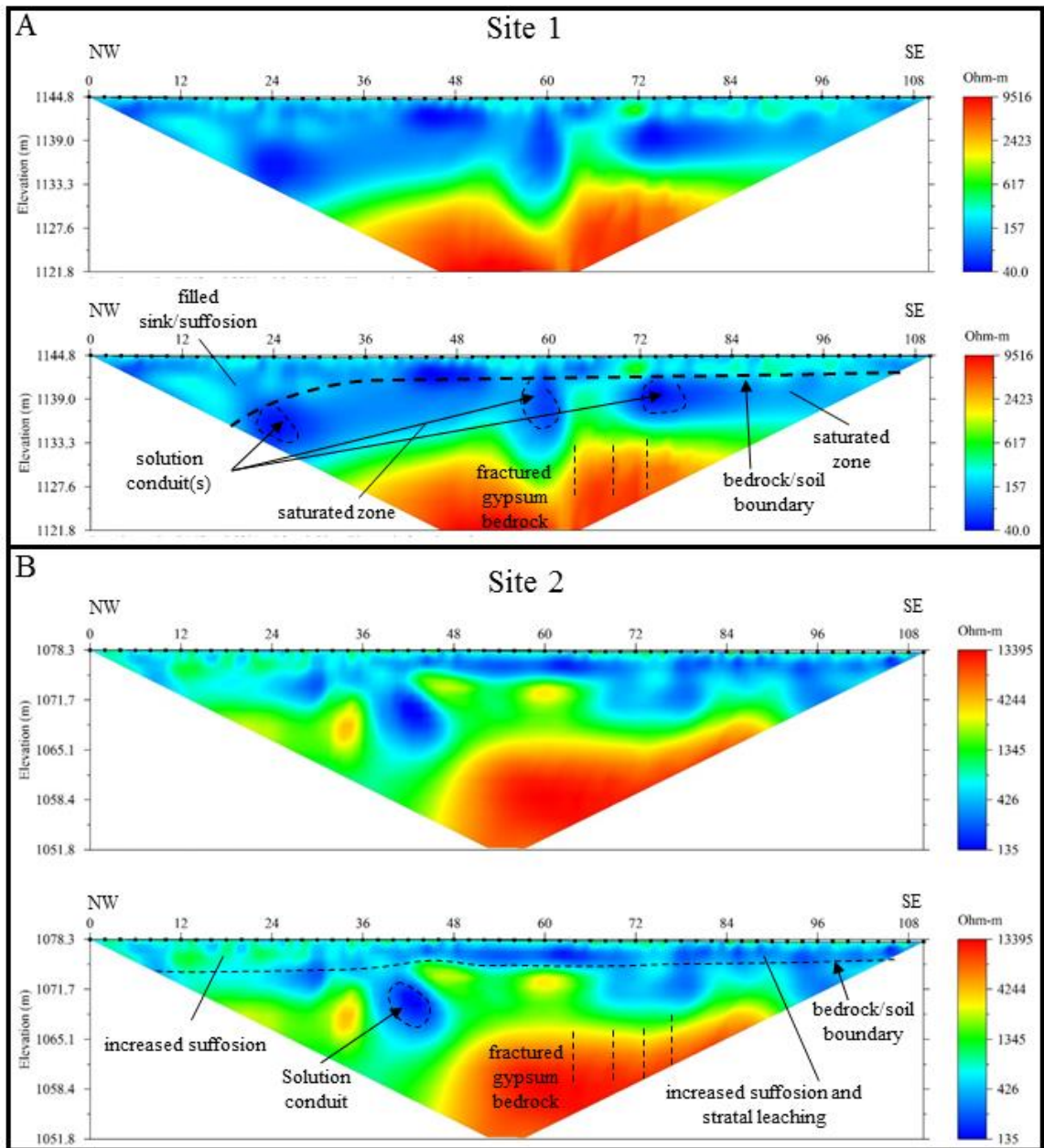


Figure 3. (A) *Site 1* inverted and interpreted inverted section (dipole-dipole array, 56 electrodes at 2-meter spacing with total survey length of 110 meters). RMS error= 5.73%, L2 norm= 0.70, iteration= 5. Scale = 1:1; (B) *Site 2* inverted and interpreted inverted section (dipole-dipole array, 56 electrodes at 2-meter spacing with total survey length is 110 meters). RMS error= 4.63%, L2 norm= 0.76, iteration= 4. Scale=1:1.

LiDAR image of this site shows surficial karst features proximal to the survey site (Figure 4A). Most notable is the cave entrance directly opposite the survey site which was discovered during land reconnaissance prior to this study. Observations of this feature showed a sediment-filled solutional conduit that trends underneath the road towards the filled sinkhole on the opposite side and underneath a small collapse structure in the road. Other karst features delineated from LiDAR and land surveying include a collapse feature and cave entrance northeast of survey site; however, due to private land restrictions this feature was not surveyed.

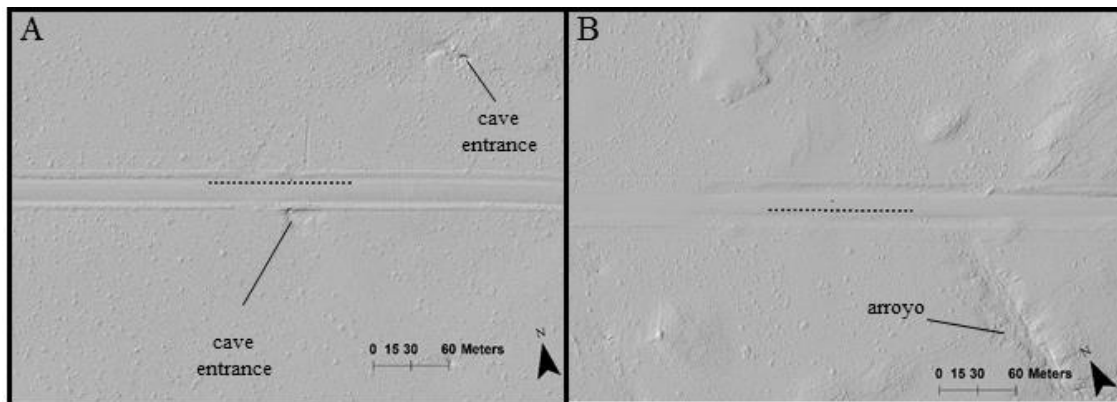


Figure 4. (A) *Site 1*. LiDAR images showing location of cave entrances proximal to survey site. (B) *Site 2* LiDAR image showing proximal entrenched arroyo. Dashed lines represent approximate location of electrical resistivity surveys.

Site 2

Survey of *Site 2* was conducted in a northwest-southeast trending line with 56 electrodes at 2-meter spacing with an effective depth penetration at 26.5 meters and a total survey length of 110 meters (Figure 3B). Low resistivity anomaly located between

meter mark 34 and 42 and at 7-15 meters in depth is interpreted to be a solution conduit filled with soil located on edge of a ridge near-surface bedrock. Thicker gypsic soil occurs to the northwest where increased shallow suffosion is common. Stratal leaching associated with gypsum dissolution is attributed to the contrasting low and high resistivity and represent variable moisture content in the subsurface within solutionally-widened fractures and gypsum laminae. High resistivity anomaly at depth is highly fractured gypsum (dashed vertical lines). Entrenched arroyo located in the southeast and down gradient of the survey site likely promotes increased transport of soils over the surface and through the subsurface as suffosion (Figure 4B).

Site 3

Survey of *Site 3* conducted in a northwest to southeast trending line utilizing the roll-along survey method with maximum depth penetration of 13.6 meters (Figure 5A). Roll-along survey at 1-meter spacing provided enhanced resolution of the shallow subsurface in this area. Particular importance was given to this area given the numerous karst features and lineaments observed during land surveying and LiDAR image analyses (Figure 6A). Suffosion processes are less common due to thin soil profile, but epigene karst development is more pronounced. From meter mark 22-50, isolated anomalies of high resistivity (5k-27k Ωm) at shallow depths are interpreted to be solution conduits likely connected to the surface creating largely air-filled voids with minor sediment and moisture; correlation was made through excavation during field verification.

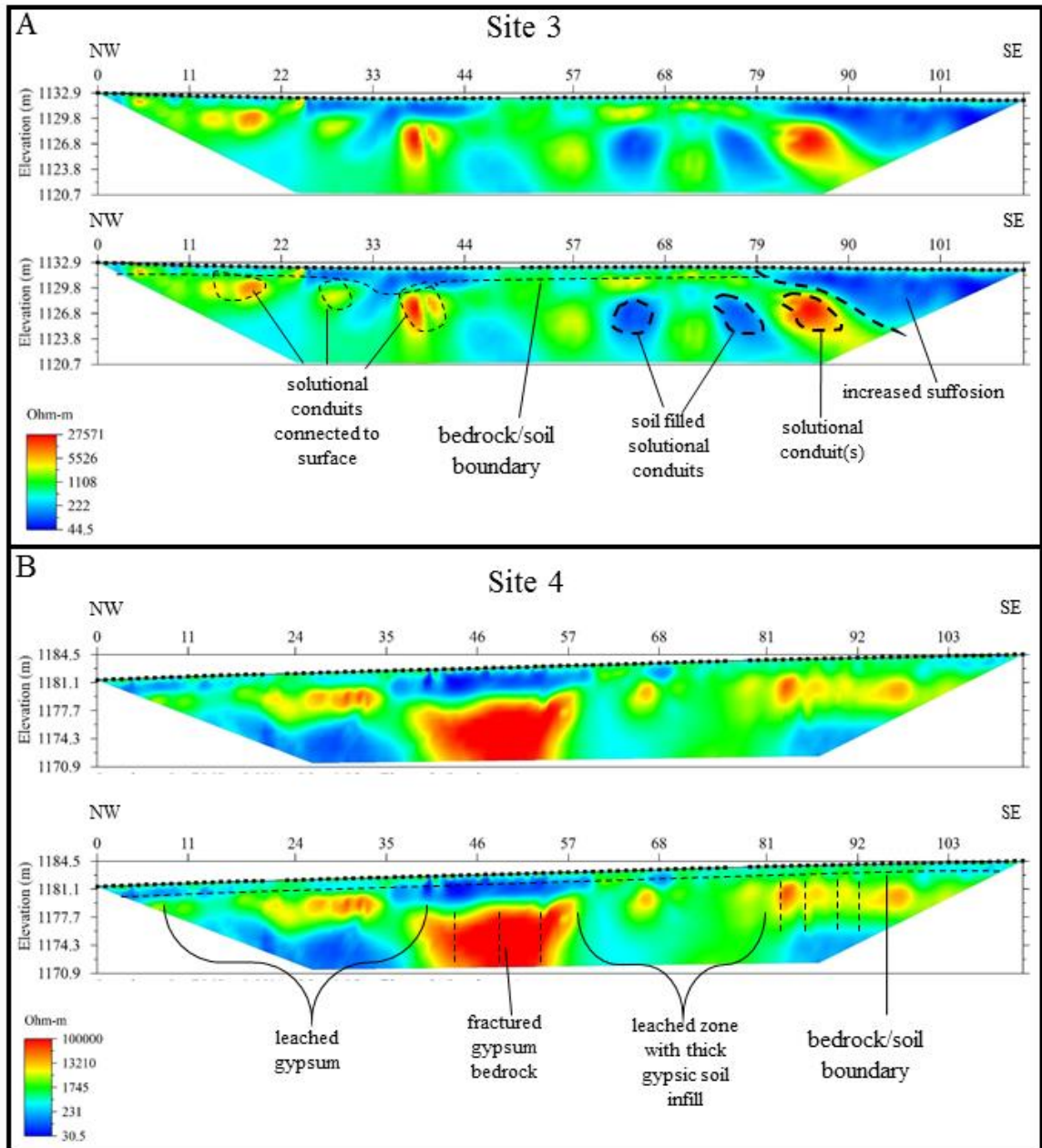


Figure 5. (A) *Site 3* inverted section and interpreted inverted section (dipole-dipole array, 56 electrodes roll-along survey at 1-meter spacing). RMS error= 7.39%, L2 norm= 0.80, iteration= 6, Scale= 1:1; (B) *Site 4* inverted section and interpreted section (dipole-dipole array, 56 electrodes roll-along survey at 1-meter spacing). RMS error= 8.99%, L2 norm= 0.85, iteration= 8, Scale=1:1.

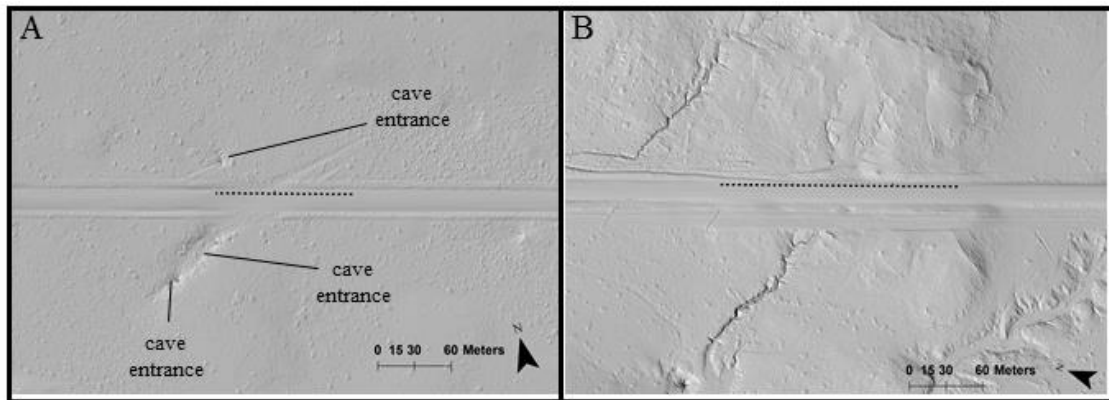


Figure 6. (A) LiDAR image of *Site 3* with multiple cave entrances observed and documented on the surface with conduits trending laterally underneath the road. (B) LiDAR image of *Site 4* with highly fractured gypsum bedrock on surface. Dashed lines represent approximate survey locations.

Furthermore, cave surveys conducted southeast of the survey site determined lateral continuation of a cave passage partially filled with soil underneath the road (Figure 7). From meter mark 62-85 and depths of 4 to 7 meters are three anomalous zones of low resistivity zones interpreted to be soil-filled solution conduits. Road base failure in this area may enhance groundwater recharge and infilling of these conduits. The high resistivity anomaly ($\sim 27\text{k } \Omega\text{m}$) from meter mark 80 to 90 and depths of 4-7 meters represents a solution conduit devoid of any soil infill and likely decoupled from active karst processes in the nearby proximity. From meter mark 80-112 is an area of lower surface elevation and low resistivity values ($45 \text{ } \Omega\text{m}$) at depths of 1-7 meters. These indicate a saturated vadose zone and thicker soil profile where excessive surface ponding of water occurs during rain events.

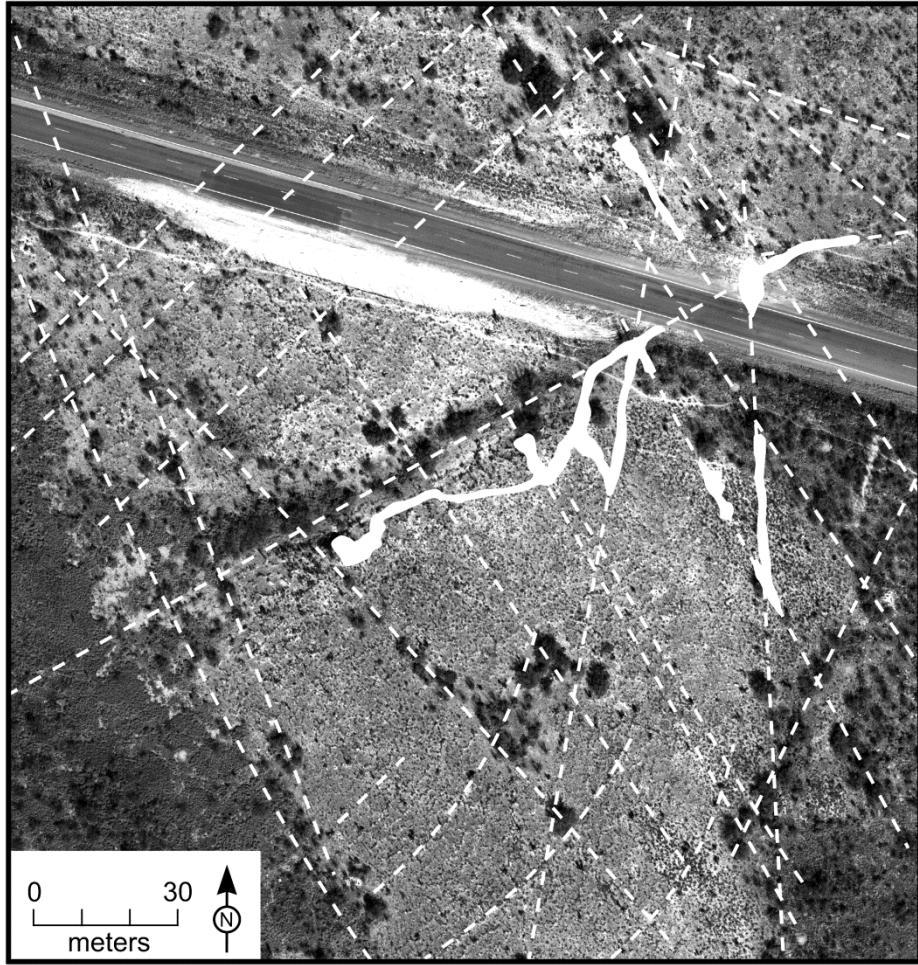


Figure 7. Aerial photo showing extent of surveyed caves (solid white fills) and surface lineaments (dashed white lines) that represent near-vertical fractures at survey *Site 3*

Site 4

Survey of Site 4 was conducted in a northwest-southeast trending line with a total survey length of 111 meters (Figure 5B). This site is located in the northwestern region of the study area where clusters of hypogene caves and commonly observed. Outcrop of fractured gypsum bedrock is exposed at the surface along the survey line (Figure 6B). Survey was conducted with the roll-along method at 1-meter electrode spacing for enhanced resolution. From meter mark 0 to 50 is a saturated zone with enhanced dissolution in the subsurface, this is partly due to the sloping terrain where overland flow of solutionally aggressive waters are focused as represented by the dashed outline of the low resistivity anomalies. High resistivity anomaly (100k Ω m) from meter mark 40 to 58 and 7-14 meters in depth is interpreted to be highly-fractured gypsum bedrock where migration of descending fluids and mobilized gypsic soils associated with dissolution is concentrated. From meter mark 80-112, zones of contrasting high/low resistivity indicate a series of fractures at depth.

Site 1 (220-meter survey)

A second survey conducted at Site 1 was acquired with a 4-meter electrode spaced survey and a total survey length of 220 meters (Figure 8). Survey was conducted from northwest to southeast. Total depth penetration was 41.3 meters. Multiple features in this inverted section can be correlated with the higher resolution, shallow depth 2-meter electrode spaced survey of Site 1 (Figure 3A). The anomalous low resistivity zones

interpreted as solution conduits between meter mark 120-152 and 5-6 meters in depth show similar characteristics to the previous survey of Site 1, and thus have been labeled as the same features. Dashed line across entire profile represents the approximate soil/bedrock boundary correlated from excavation. The low resistivity zone from meter mark 64-76 and 5-8 meters in depth has similar characteristics to the confirmed sinkhole between meter mark

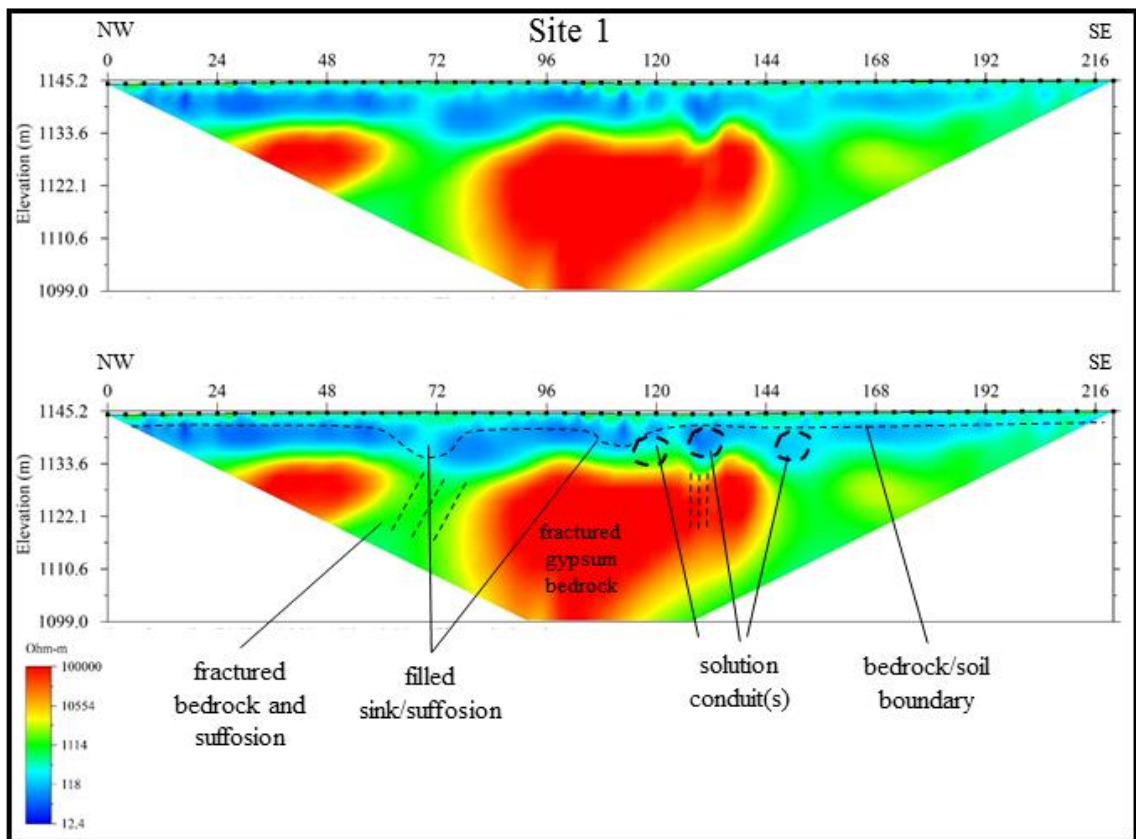


Figure 8. *Site 1* inverted and interpreted inverted ERT profile (dipole-dipole array, 56 electrodes at 4-meter electrode spacing). RMS error= 6.88%, L2 norm= 0.90. Iteration= 7. Scale= 1:1.

104-120 and, therefore, was interpreted to be a similar feature. Increased suffosion may occur in this location. At depths of 8 meters and beyond the extent of fractured gypsum bedrock is more pronounced with resistivity values up to 100k Ω m. Discontinuity in competent bedrock can be inferred by the stark contrast in resistivity between meter mark 60 and 76, this zone likely represents fractured gypsum with soil fill.

KARST PROCESSES DELINEATED BY RESISTIVITY ANALYSES

The occurrence of karst related geo-hazards in Culberson County can be naturally occurring or anthropogenically-enhanced. Karst terrains are well known to exhibit complex interaction between geomorphology, hydrogeology and stratal diagenesis (Stafford et al., 2008a). The triple permeability of soluble rocks (matrix, fracture and conduit porosities) creates unpredictable hydrologic systems in karst terrains, while the high solubility of gypsum adds to these complexities within the study area. The anthropogenic effect in karst related geo-hazards is often associated with road construction, pollution and de-watering of karst aquifers for agricultural and industrial use (Klimchouk and Andrejchuk, 1996). Within the study area, anthropogenic effects are mainly attributed to infrastructure development; however, natural occurrences abound. Land traverses conducted prior to electrical surveying identified several features such as potholes, road base exposure and fractures, which could be correlated to resistivity data as zones of induced suffosion (Site 3), solutional conduits (Site 1 and Site 3) and fractured bedrock (Site 2 and Site 4).

Geo-hazards attributed to natural karst in the region appear to be dominated by suffosion processes that are coupled with deeper karst phenomena, both solutional conduits and solutionally enhanced / leached zones. Caves, fractures and sinkholes are areas of high permeability that facilitate suffosion during heavy precipitation events,

which subsequently induce piping and void creation beneath road bases that create subsidence failures.

Surveys conducted at Site 1 and Site 3 showed thicker soil horizons in the resistivity profile section that are interpreted to be caused by suffosion where soil is ‘piped’ into open cavities from the surface. Discontinuities in the gypsum bedrock observed after excavation shows that a zone of thicker gypsic soil fill at Site 1 is related in part to preferential dissolution or ‘leaching’ of bedrock at shallow depths where collapse and subsequent soil infilling have occurred. This same process can be attributed to Site 3, except dissolution of gypsum bedrock has created near vertical conduits or solution ‘pipes’ which can be seen cropping out locally. Cave passages that extend directly underneath the road proximal to Site 1 and Site 3 may act as recharge zones where overland flow transports soil into the subsurface, while also adding solutionally-aggressive waters to the conduit system.

Fractures identified in the resistivity profile analyses are inferred mainly from surficial expressions at Site 2 and Site 4, where solutional widening of these fractures has occurred by gravitationally-driven fluid migration which creates near-vertical, planar features that are ubiquitous in the area. Ascension of moisture laden air through density convection from the water table also contributes to solutional widening in these zones, which is more common in the hypogene karst regions of the study area (Stafford et al., 2008). In both instances, these fractures act as secondary pathways for soil transport

associated with suffosion processes. Similar to fractured zones, leached zones of gypsum were identified in resistivity profile section of Site 3 and Site 4, where leaching occurs in regions of sustained water ponding over fractured gypsum rock or fractured indurated gypsic soil. Leaching subsequently results in differential dissolution both laterally and vertically that promotes compaction and differential subsidence. Excavation at Site 4 showed leached zones at shallow depths 2-5 meters where heavily fractured gypsum rock was solutionally-widened and partially infilled with soil.

CONCLUSIONS

Expressions of karst are abundant in the study area and can easily be observed exposed at the land surface and in geophysical imaging throughout the outcrop region of the Castile Formation. The application of electrical resistivity surveying in determining these expressions and related geo-hazards proved essential in this study to characterize surficial failures that were not directly connected to the surface as exposed karst features. All sites showed direct evidence of karst-induced road failures; however, a priori knowledge of the proximal hydrogeologic system was required for proper identification of resistivity anomalies detected in the surveys, which included suffosion, subsidence, solutionally-widened fractures, and solutional conduits. In many instances, anthropogenic modifications of the land surface through road construction and maintenance exacerbated the pre-existing karst phenomena by altering the local hydrogeologic system; however, these features are also naturally occurring throughout the region.

An increase in electrode spacing from 2-meters to 4-meters at Site 1 proved to be a useful method in characterizing the extent of karst features at greater depths. A consequence, however, of increased electrode spacing is diminished resolution at shallow depths, yet when combined with a 2-meter electrode spaced survey correlations could be consistently made (Figure 3A and Figure 8). Broad features such as bedrock discontinuity and soil/bedrock boundaries are easily distinguishable as well in both surveys.

The heterogeneous nature of karst, and specifically gypsum karst, creates less than favorable conditions for electrical resistivity surveying, especially in dry arid geographical locations where electrical coupling between electrodes is difficult to achieve. In this study, sites where the surface was more homogenous or contained indurated gypsic soils were more suitable for data acquisition. Other limitations to consider are the three dimensional effects of the features identified in two dimensional inverted sections. A common, yet more time consuming approach to this problem would be to conduct 3D electrical surveys to more accurately characterize the size and extent of shallow bodies. However, this study area was adjacent to roads which precluded acquisition of 3D surveys due to heavy traffic.

Non-invasive, spatial delineation of karst geohazards is critical for infrastructure development within heavily impacted anthropogenic regions. The ability to detect and characterize karst phenomena within the shallow surface can enable improved construction design and geo-hazard mitigation that will reduce the probability of catastrophic failure. Traditional resistivity methodologies like this study are time intensive, but they provide high-resolution characterization for regions of known or suspected geohazards. However, it is essential that geophysical studies be correlated with traditional geologic and hydrologic studies in karsted regions for proper identification and delineation of remotely-sensed potential geohazards.

ACKNOWLEDGEMENTS

This research was partially funded by the Texas Department of Transportation with support from the Department of Geology at Stephen F. Austin State University. The authors are grateful to the generous field assistance of individuals that made this work possible: Jonathan Woodard, Nikota Welch, and Aaron Eaves.

REFERENCES

- Benson, R.C., and Yuhr, L.B., 2015, Site characterization in Karst and Pseudo-Karst Terraines: Practical strategies and technology for practicing engineers, Hydrologists and geologists: 2016: Netherlands, Springer. 421p.
- Greenwood, J., 2016, Electrical Resistivity, Induced Polarization (IP) & Self-Potential (SP) for Engineering and Environmental Applications:
- Hentz T.F., and Henry C.D. (1989) Evaporite-hosted native sulfur in Trans-Pecos Texas: relation to late-phase Basin and Range deformation. *Geology* 17, p. 400-403.
- Hill, C.A., 1996. Geology of the Delaware Basin, Guadalupe, Apache and Glass Mountains: New Mexico and West Texas. Permian Basin Section – SEPM, Midland, TX, 480 p.
- Horak, R.L., 1985, Trans-Pecos tectonism and its effects on the Permian Basin, in Dickerson, P.W., and Muelberger, W.R., eds., Structure and Tectonics of Trans-Pecos Texas: Midland, Texas, West Texas Geological Society, p. 81–87.
- Kirkland, D.W., 2003, An explanation for the varves of the Castile evaporites (upper Permian), Texas and New Mexico, USA: *Sedimentology*, v. 50, p. 899–920.
- Klimchouk, A., and Andrejchuk, V., 1996, Environmental problems in gypsum karst terrains: *International Journal of Speleology*, v. 25, p. 145–156.
- Klimchouk, A., 2000, Speleogenesis in gypsum. In: Klimchouk A., Ford D.C., Palmer A.N. & Dreybrodt W. (Eds.) *Speleogenesis: evolution of karst aquifers*. Huntsville, National Speleological Society, p. 261-273.
- Loke, M.H., 1999, Electrical imaging surveys for environmental and engineering studies: A practical guide to 2-D and 3-D surveys.

- Metwaly, M., and AlFouzan, F., 2013, Application of 2-D geoelectrical resistivity tomography for subsurface cavity detection in the eastern part of Saudi Arabia: *Geoscience Frontiers*, v. 4, p. 469–476.
- Niederleithinger, E., Weller, A., and Lewis, R., 2012, Evaluation of Geophysical techniques for dike inspection: *Journal of Environmental & Engineering Geophysics*, v. 17, p. 185–195.
- Palmer, A.N., 2006, *Cave geology*: Dayton, OH, Cave Books.
- Scholle, P.A., Goldstein, R.H., and Ulmer-Scholle, D.S., 2004, *Classic Upper Paleozoic Reefs and Bioherms of West Texas and New Mexico*. New Mexico Institute of Mining and Technology, Socorro, NM, 166p.
- Stafford, K., Nance, R., Rosales-Lagarde, L., and Boston, P., 2008a, Epigene and hypogene gypsum karst manifestations of the Castile Formation: Eddy County, New Mexico and Culberson County, Texas, USA: *International Journal of Speleology IJS*, v. 37, p. 83–98.
- Zhou, W., Beck, B., and Adams, A., 2002, Effective electrode array in mapping karst hazards in electrical resistivity tomography: *Environmental Geology*, v. 42, p. 922–928.

APPENDIX A

LITERATURE REVIEW

INTRODUCTION

The Delaware Basin of West Texas and southeastern New Mexico is the major western subdivision of the Permian Basin and a northern extension of the Chihuahuan Desert. The north-northwest trending basin is a pear shaped depression that is roughly 250 km long and 180 km wide and encompasses an area of 33,500 square kilometers (Hill, 1996). The location of this study is a 54.7 kilometer stretch of Texas Ranch to Market Road 652 (Figure A1) that lies entirely within Culberson County; this road

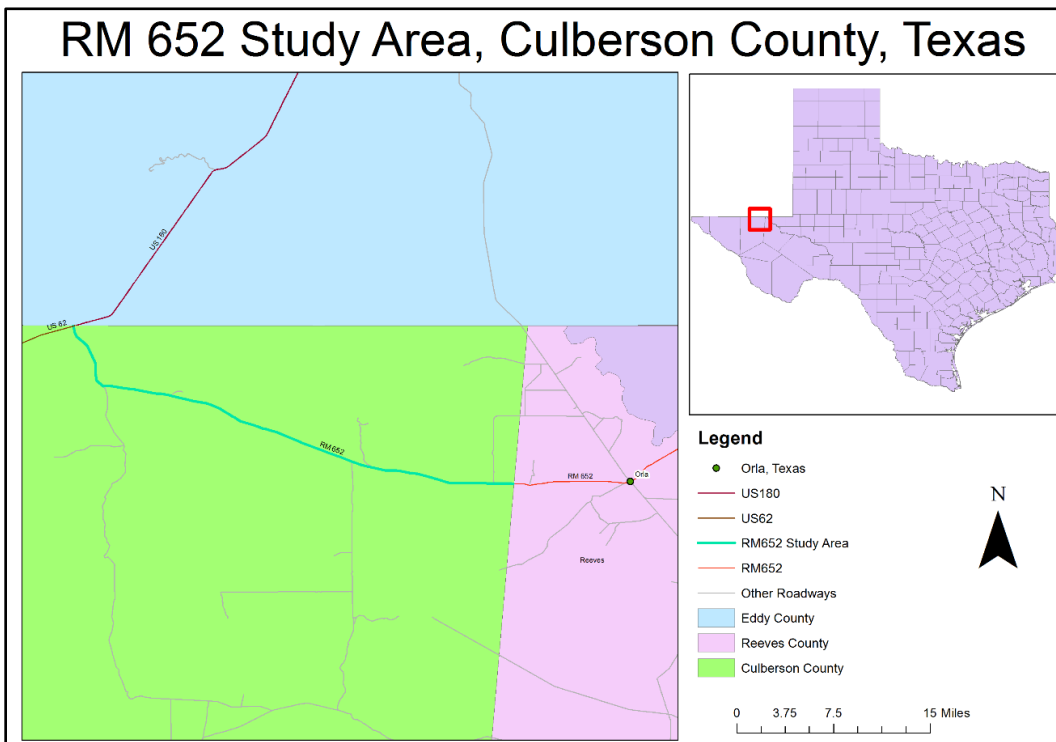


Figure A1. Map of study area and surrounding counties.

extends an additional 38.6 kilometers into Reeves County, Texas. Annual precipitation ranges from 15-40 cm with an average annual temperature of 24 degrees Celsius and an average summertime high of 40 degrees Celsius.

The Delaware Basin has been characterized as a classic evaporite intracratonic basin and is an important oil and gas producing province. The stretch of road in focus is widely used for commercial transportation; however, due to the nature of karst terrains, several zones of failure along and directly beneath the road have occurred with recent increases in heavy vehicle traffic. The Castile Formation, the major stratigraphic unit underneath the road in the study area, is composed primarily of gypsum which is highly susceptible to dissolution from meteoric and groundwater flow and presents a significant geohazard risk.

This study utilizes electrical resistivity to characterize and delineate the karst geohazards along a 55 kilometer section of Texas Ranch to Market Rd 652 in Culberson County. Approximately 20 sites of major concern have been identified by previous road failures, GPR (ground penetrating radar) and visual inspection (Stafford, 2015). Electrical resistivity data was collected at these sites using a *SuperSting R8 56 Electrode System* manufactured by AGI (Advanced Geosciences, Inc).

West Texas: Delaware Basin

The Delaware Basin covers an area of approximately 33,500 square kilometers in the western portion of the Permian Basin in west Texas and southeastern New Mexico (Figure A2). The basin fill consists of Phanerozoic sedimentary rocks 7,300 m thick with the vast majority of deposition occurring during the Permian (Kelley, 1971; Hills, 1984).

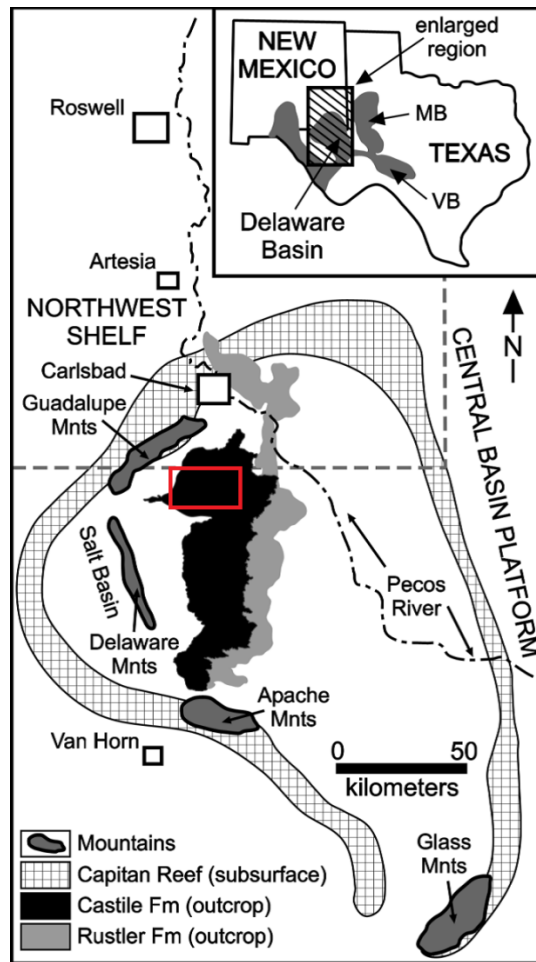


Figure A2. Location of study area showing outcrops of Castile and Rustler formations. (from Stafford 2008c).

The basin is outlined by a 600-700 kilometer chain of Capitan Limestone which crops out as the Guadalupe Mountains to the northwest and the Glass and Apache Mountains to the west and south, respectively (Hill, 1996).

STRUCTURAL HISTORY OF THE DELAWARE BASIN

The supercontinent, Rodinia, existed during the Proterozoic within which the North American craton was rooted; structural events during this time are unclear, yet played a crucial role in the formation of the Delaware Basin (Horak, 1985). Precambrian structures of the Permian Basin exerted significant controls on subsequent Phanerozoic deposition. The Proterozoic history of the Permian Basin can be characterized by five or six events, resulting in the formation of a failed triple rift junction, the Delaware aulacogen, post Grenville deformation. These early structures were reactivated during the Paleozoic through Cenozoic, which account for the distribution and pattern of sedimentation throughout the basin (Horak, 1985; Adams and Keller, 1996).

By Late Precambrian, passive continental margins flanked the North American continent and steady subsidence allowed for the deposition of shelf sediments. The larger Tobosa Basin, which the Delaware Basin is part of, first formed in the Cambrian by rifting of a continental block from the North American craton (Dickinson, 1981; Hill, 1996). The passive margin phase (Horak, 1985) and sedimentation phase (Hills, 1985) established a 300-million-year period when a shallow sea covered southeastern New Mexico and west Texas resulting in passive sedimentation in the slowly subsiding basin enclosed by Paleozoic carbonate shelves (Hill, 1996).

During the early Paleozoic, up until the Mississippian, minor tectonic activity related to weak extensional and western compressive stresses produced block faulting and eastward tilting of the basin. The Antler Orogeny in the Late Devonian-Mississippian was responsible for a broad overarch in most of New Mexico and northern Texas (Hill, 1996). By the middle Paleozoic, the Tobosa Basin was slightly tilted to the east and sediment deposition reached a thickness of 7300 meters (Hills, 1985).

During the Late Mississippian through the Early Permian, collision of Laurasia and Gondwana formed the supercontinent of Pangea which gave rise to the Ouachita Orogeny in the Marathon-Delaware Basin area (Hill, 1996). Compressive forces from the advancing Ouachita fold and thrust belt in the southeast caused block faulting along Precambrian zones of weakness in the Tobosa Basin. These crustal blocks rose and subsided along high angle faults causing a separation of the basin into the Central Basin, Midland Basin and Delaware Basin (Horak, 1985; Hill, 1996). Northwestward compression from the approaching Ouachita orogenic front caused rapid subsidence of the Delaware Basin in the Pennsylvanian, and erosion of the uplifted Marathon-Glass Mountains filled the basin further with sediment eventually separating it from the rising Central Basin Platform. By the beginning of the Leonardian, collision of Laurasia and Gondwana had ceased and the Delaware Basin remained tectonically stable throughout the rest of the Permian (Hill, 1996). Subsidence, however, did continue with deposition of fine- to coarse-grained clastics into the basin while growth of an extensive

carbonate/evaporite platform nearly enclosed the entire basin (Horak, 1985). By the end of the Permian, during Ochoan time, uplift of the basin occurred causing a slight eastward tilt which eventually cutoff the Hovey Channel, a basinal outlet channel which once connected the basin to open marine waters. The deposition of clastics and carbonate sediment ceased and deposition of evaporites became dominant in the constricted basin (Hill, 1996).

The Mesozoic was a period of relative stability in the Delaware Basin. However, in the Early Triassic as final assembly of Pangea occurred, the Delaware Basin was uplifted above sea level and deposition was influenced primarily by erosion and fluvial sedimentation (Dickenson, 1981). By the Late Triassic to Early Jurassic, the Marathon region, south of the Delaware Basin, began to take shape as the Yucatan peninsula pulled away from Texas forming the Gulf of Mexico (Dickenson, 1981). According to Horak (1985) and Keith (1982), as the rifted margin of the Gulf of Mexico subsided; transgression of marine waters spread across the region and deposition of sediments occurred in much of Texas and the Western portion of the United States. At the close of the Mesozoic, subduction of the Farallon Plate on the western coast of the United States resulted in a weak tilt of the Delaware Basin to the east as movement along the pre-existing Precambrian zones of weakness occurred (Hills, 1984). The most pronounced effect of the Laramide Orogeny was the elevation of the Permian Basin by as much as 1200 meters, which raised the basin above sea level during this time (Horak, 1985).

By the early to middle Eocene (55-43 Ma) effects of Laramide Orogeny had subsided significantly and the Delaware Basin entered another period of stability (Hill, 1996). However, by about 40 Ma the region was again interrupted by a brief phase of volcanism related to a steepening of the subducted Farallon slab (Keith, 1978). Intrusions of calc-alkalic and alkalic belts were emplaced over a wide area in the Delaware Basin and represent the eastward extent of compression and arc-magmatism in the region (Hill, 1996). While the volcanic phase was the initial stage of extension in the region, subsequent Basin and Range extension and tectonism (30-0 Ma) was responsible for major block faulting and further epirogenic uplift of the western portion of the Delaware Basin (Horak, 1985; Hill, 1996). As the lithosphere beneath the Delaware Basin thinned and extended during this phase of Basin and Range extension, the heat regime changed from that of intrusive magmatism to an increased temperature gradient and convective heat flow. Effects of Basin and Range extension decrease considerably by the beginning of the Quaternary, except for brief episodes of seismic activity and normal faulting in the region (Hill, 1996).

STRATIGRAPHY

The Delaware Basin and surrounding area contain over one billion years of stratigraphic record with an estimated 95% of the outcrops being Permian in age. The Permian strata within the basin reach a maximum thickness of 2000 meters (Hill, 1996). For the purposes of this study, only strata related to RM 652 in Culberson County will be discussed as karst geohazards are restricted to Ochoan strata and hydrogeologic relationships within the underlying Guadalupian strata (Stafford, 2015)

GUADALUPIAN STRATIGRAPHY

The Guadalupian depositional history can best be characterized by extensive growth of stratigraphic reefs that separated the deep ocean basin from the shallow back reef lagoons. During this time, a thick clastic sequence was deposited in the deep basin with limestone and carbonate reef facies deposited on a shallow lagoonal shelf (Figure A3). The Goat Seep Dolomite and Capitan Limestone were deposited as carbonate reef facies while the Artesia Group were deposited as backreef facies on the platform margin (Hill, 1996).

Deposition of the Cherry Canyon and Bell Canyon formations within the Delaware Basin occurred during sea level lowstands as siliciclastic material prograded across the northwestern shelf in the middle-Guadalupian time (Scholle et al. 2004). Rapid deposition during this time was accommodated by subsidence along the Central Basin fault boundary (Hill, 1996). Deposition of carbonate reefs had ceased by the end of the Guadalupian as a consequence of reef growth in the subsiding basin and the closing of the Hovey Channel which restricted open marine circulation. The basin was then filled with a thick evaporitic sequence beginning with the Castile during Ochoan time (Hill, 1996; Scholle et al. 2004).

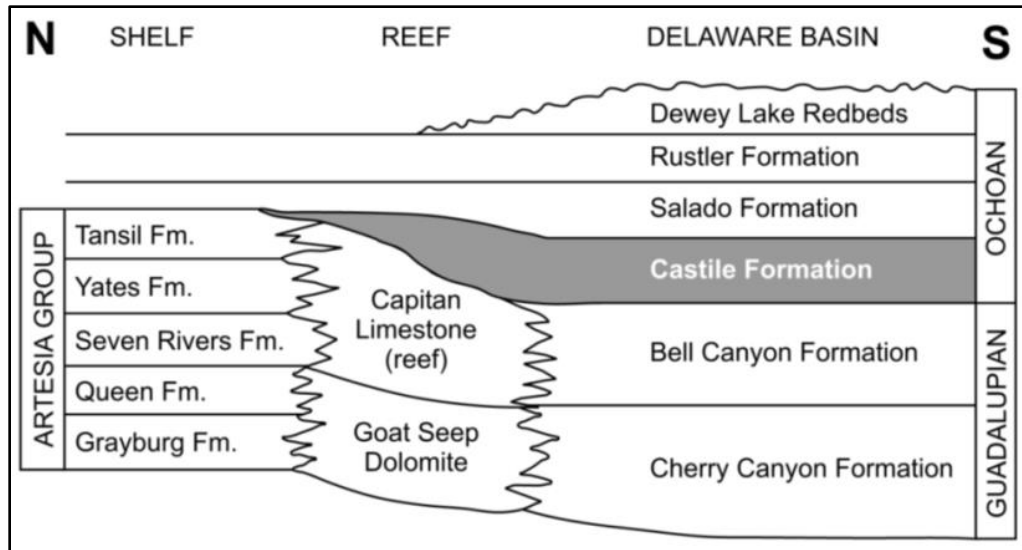


Figure A3. Stratigraphic section from north to south through the Delaware basin showing the major units in the study area (from Stafford 2015, adapted from Scholle et al., 2004).

Cherry Canyon Formation

The Cherry Canyon Formation is the middle formation of the Delaware Mountain Group and forms the upper half slope below Capitan Limestone cliffs in the southern portion of the Guadalupe Mountains (King, 1942; Hill, 1996). In this outcrop, the unit consists of 300-400 meters of thinly-bedded, laminated sandstone and siltstone. Sixteen separate cycles of deposition are identified in 145 meters of this unit, and occur in every 3-6 meters. The cycles begin with a shaly sandstone layer followed by a thin layer of sandstone which culminates in a thin lenticular limestone layer before the process is repeated. The lowermost portion of this formation consists of a sandstone tongue which persists to the Northwest Shelf in the Guadalupe Mountains and consists of an arkosic

sandstone with bluish-green shale layers and is notable because it does not change into limestone shelfward (Hill, 1996). The Cherry Canyon sandstone tongue may have formed in deep submarine canyons which channeled massive debris flows southeastward into the deeper portions of the basin during the Leonardian (Harrison, 1966; *as cited in* Hill, 1996). Above the sandstone tongue, are the limestone members of the Cherry Canyon Formation, the Gateway, South Wells and Manzanita limestones (Hill, 1996).

Bell Canyon Formation

According to King (1942), the Bell Canyon Formation is the upper part of the Delaware Mountain Group and crops out as a broad belt between the crest of the Delaware Mountains and the reef zone at the margin of the Delaware Basin in the east. The formation varies in thickness from 200-300 meters. It consists of primarily of fine-grained sandstone and coarse-grained siltstone with interbedded layers of limestone and is lithologically similar to the Cherry Canyon Formation. Carbonate tongues interfinger with sandstone units along the margins of the basin and thicken towards the reef complex of the Capitan Limestone (Hill, 1996).

OCHOAN STRATIGRAPHY

The Ochoan stratigraphy is dominantly evaporite facies consisting of anhydrite, halite, and thin sequences of dolomite and redbeds. The lowest formation, the Castile, is only found within the Delaware Basin (King, 1942). Deposition of evaporites during the Ochoan represents a dramatic change in sedimentation from the primarily carbonate and siliciclastic facies of the Guadalupian. The closing of the Hovey Channel and restriction of marine circulation is attributed to the thick evaporite facies. The Ochoan series consists of the Castile, Salado, Rustler and Dewey Lake formations with a combined thickness of 1200-1500 meters. Outcrops of these formations are extremely limited on the surface due to the high solubility of evaporites (Hill, 1996).

Castile Formation

The Castile Formation is a clastic-free evaporite sequence consisting of massive to laminated anhydrite/gypsum and calcite with interbedded halite and overlies the Bell Canyon Formation. The Castile crops out in the west from the Delaware Mountains to the Rustler Hills in the east with a total area of 2600 square kilometers in southeastern New Mexico and west Texas. Thickness varies due to the dissolutional properties of anhydrite and halite, but in some areas the formation can be up to 540 meters thick. Characteristic features of the Castile Formation are the “castile buttes” in the study area. These buttes

are sub-circular hills that rise on average 30 meters in the Gypsum Plain and are composed of replacement calcite Tertiary in age resulting from sulfate reduction in the presence of ascending light hydrocarbons. These Castile buttes offer excellent opportunities for close up investigation of the laminated gypsum. These laminations are interpreted to be annual periods of calcite-anhydrite couplets representing influx of freshwater during wet seasons followed by evaporation during hot dry seasons (Hill, 1996).

Salado Formation

The Salado Formation is primarily composed of halite containing layers of anhydrite, potash and minor amounts of siliciclastics. Thickness of the Salado is variable due to intrastratal dissolution, but can be as much as 500-600 meters thick in some parts of the basin. Within the study area, the Salado is completely dissolved away. Dissolution of salt in the subsurface indicates that the western limit of the Salado is an erosional boundary and not depositional. Leached zones commonly occur throughout the Salado where halite is completely removed, and zones of blanket dissolution breccias or intrastratal breccia are common throughout the Salado and Castile formations and extend vertically for hundreds of meters. In contrast to the underlying Castile Formation, the Salado is known to have been deposited in a shallow mud flat or lagoonal setting (Hill, 1996).

Rustler Formation

The Rustler Formation outcrops in the Rustler Hills west of the study area. Subsequent to Salado deposition, transgression occurred throughout the region representing a decline in the hypersaline waters that existed in the basin. Rustler deposition occurred in a low relief basin and lacks major facies changes. Alternating transgression and regressions are represented by the alternating limestone/dolomite and anhydrite/gypsum layers within the formation. The formation consists primarily of dolomite, siltstone, anhydrite and halite. The Rustler is nearly identical to the Salado but contains significantly more limestone, dolomite and siliciclastics (Hill, 1996).

Dewey Lake Redbeds

The last advance of the Permian sea is marked by the deposition of the Rustler, as the sea retreated the Dewey Lake Redbeds were deposited and consist mainly of well-laminated, thin-bedded red to orange siltstone, claystone and fine-grained sandstone. The Dewey Lake Redbeds outcrop in various parts of the Delaware Basin, however, the most prominent outcrop is in the eastern portion of the basin where thickness is up to 150 meters. Small scale sedimentary structures within the unit suggest several modes of grain transport which include eolian and fluvial (Hill, 1996).

KARST OF THE DELAWARE BASIN

The Castile Formation the Delaware Basin is primarily composed of gypsum and anhydrite and has been commonly referred to as the Gypsum Plain (Hill, 1996).

Manifestations of karstic terrain include the dissolution of soluble rocks, such as gypsum and anhydrite, forming closed depressions, caves, fissures and sinkholes (Palmer, 2006).

High solubility of evaporites such as the Castile have allowed for the large scale development of cave and karst in the Delaware Basin; surficial expressions of karst within the Castile outcrop are abundant and include sinkholes, karren and surficial precipitates. Altogether 3,237 karst related features have been indentified in the region using GIS-based spatial analyses and are determined to be hypogene or epigene in origin (Figure A4) (Stafford et al; 2008a, 2008b). The Castile karst evolution within the study area manifests itself in four primary ways: 1) surficial karst, 2) epigene caves, 3) hypogene caves, and 4) intrastratal brecciation. Due to speleogenetic process, these different forms commonly overlap within the Castile Formation of the study area (Stafford et al; 2008a).

Surficial karst: Castile Formation

Surficial karst manifestations within the Castile Formation crop out across 1800 square kilometers of the outcrop region and are commonly expressed as sinkholes or

karren and surficial precipitates. Approximately 8% of the bedrock is exposed, the remaining bedrock is covered with a thin gypsum crust or gypsic soils. Sinkholes or

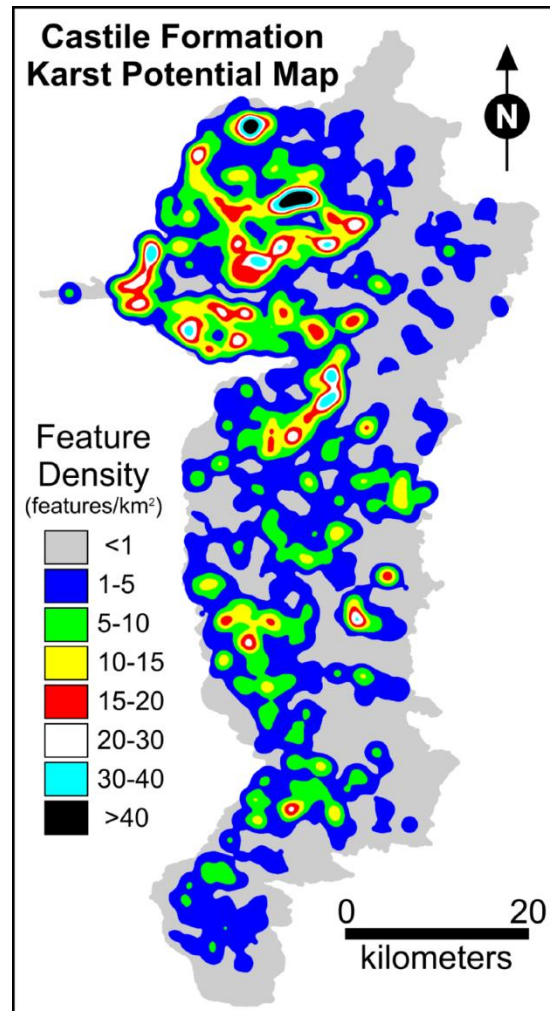


Figure A4. Density map showing the spatial distribution of karst manifestations of the Castile Formation in the study area (from Stafford et al., 2008b).

closed depressions are the dominant karst features and are characterized as both open and filled structures (Stafford et al, 2008a). Two basic mechanisms are responsible for the

formation of sinkholes: 1) solutional incision, where soluble rock is exposed at the surface and subjected to erosional process and dissolution by meteoric water, and 2) collapse structures where surface sediment fills into an upward stoping subsurface void (Stafford et al, 2008a). Incised sinkholes are generally distinguished by their lateral elongation and well-developed arroyos that connect to a central drain. Collapsed sinks are circular or elliptical in shape and are often obscured by sediment infilling (Stafford et al, 2008a). All these karst features occur within the study area, however, distinguishing them can be challenging due in part to the effects of meteoric dissolution and collapse, or epigenetic overprinting (Stafford et al, 2008a).

Epigenetic Caves

Epigenetic caves and karst are isolated features in the outcrop region of the Castile Formation and are closely associated with well-developed closed solutional depressions (Stafford et al, 2008a). Rapid dissolution of highly soluble gypsum and anhydrite by meteoric waters on the surface enhances the formation of large incised sinkholes connected to small solution conduits (Klimchouk, 2000a). Determining the origin of these solutional sinkholes is difficult due the small size of passages. The epigene caves that can be studied are limited laterally in size, and given the rapid dissolution of calcium sulfate most passages are impassable just beneath the subsurface. This is due to meteoric waters quickly increasing in saturation with respect to calcium sulfate on the land surface, thus preventing further dissolution. The epigene caves in the

study area display laminated, massive, nodular and tabular gypsum fabrics. Small-scale scallops or ripple features on the walls, ceiling and floors of the caves indicate rapid turbulent transport of water through the passages, most likely during intense monsoonal rain storms (Stafford et al., 2008a).

Hypogenetic Caves

The caves in the Castile Formation display a variety of speleogenetic features due to epigenetic overprinting by surficial processes which often obscure hypogene features in the study area. However, these same surficial processes have allowed easier access for the study of the morphological features of hypogene caves in the Castile Formation. These features which are common to caves of hypogene origin include risers, wall channels, ceiling channels, and cupolas (rounded ceiling pockets). In the Castile, however, these features form in isolated planes of maze cave development, or in conduits formed by rising fluids. Unlike other soluble rock (limestone and dolomite) the Castile Formation lacks well-defined stratigraphic layers which may be the cause for its unique cave development (Stafford et al., 2008a).

Intrastratal Brecciation and Calcitization

Zones of blanket brecciation, and vertical breccia pipes, are common throughout the Delaware Basin and are intimately tied to hypogenic speleogenesis. In the Castile, vertical breccia pipes (Figure A5) can extend through the entire thickness of section.

Occurrence in the Salado and Rustler formations is extensive as well. Breccia pipes occur by a combination of dissolution, subsidence, deformation and collapse (Hill, 1996). Intrastratal dissolution of evaporites within the formations creates void space followed by collapse of less soluble strata within the structure (Figure A6). In the study area, brecciated zones occur as collapse pits, dissolution troughs and solution subsidence valleys, which are either expressed as topographic lows where collapse has occurred or topographic highs as ‘castile’ buttes (Stafford et al., 2008a).

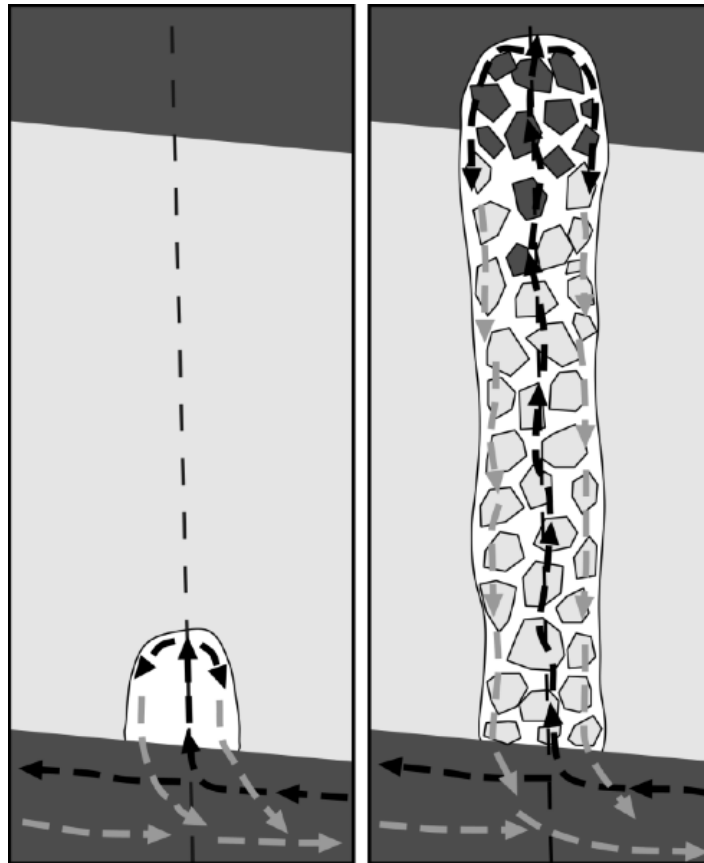


Figure A5. Diagrammatic depiction of the formation of breccia pipes. Dark arrows represent upward movement of low density undersaturated fluids and light colored arrows represent the descending high density oversaturated fluids (from Stafford, 2015).

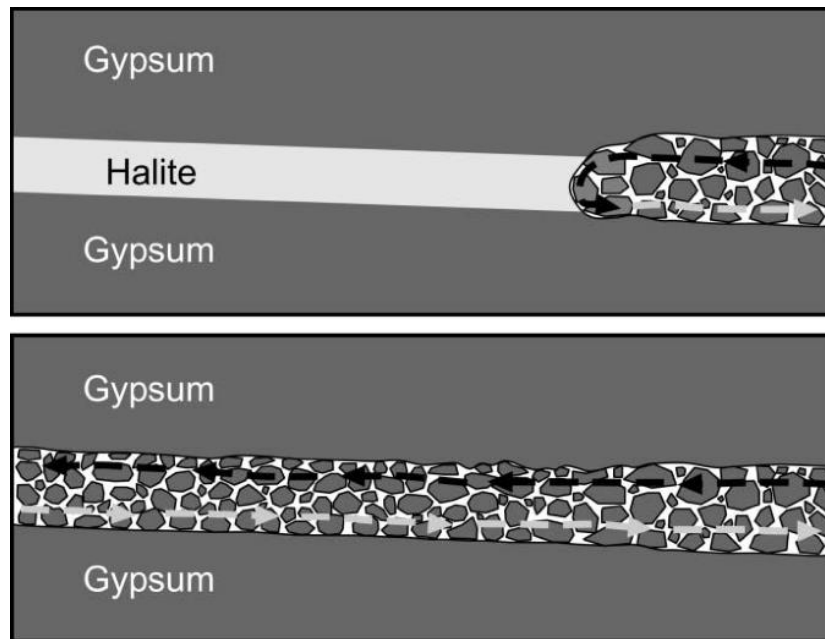


Figure A6. Diagrammatic representation of formation of blanket zones of breccia through intrastratal dissolution of halite layers (from Stafford, 2015).

The brine density convection model proposed by Anderson and Kirkland (1980) details the process by which large breccia pipes developed in the northern and eastern margin of the Delaware Basin above the Capitan Reef. In their model, upward movement of undersaturated fluids in the Capitan Reef Aquifer dissolve overlying evaporites creating solution pipes or columns. As the fluids become oversaturated and dense, they sink back down to the lower aquifer. The process is continued until the surface is breached and the convection regime changes (Anderson and Kirkland, 1980). In the Castile Formation, a similar mechanism is involved, however fluids are provided by the

underlying clastic Bell Canyon Formation and not the Capitan Reef Aquifer (Stafford et al., 2008a).

Occurrence of calcitized breccia zones is extensive within the Castile Formation. Stafford and others (2008c) identified as many as one thousand calcitized masses across the Castile outcrop. These include Castile buttes and laterally extensive zones of brecciation (Figure A6). The main processes involved in the occurrence of calcitization are Thermal Sulfate Reduction (TSR), Bacterial Sulfate Reduction and meteoric calcitization (Stafford et al., 2008c). Sulfate reduction, whether bacterially (BSR) or inorganically (TSR) is the process by which sulfate is reduced by hydrocarbons in diagenetic settings producing calcite and hydrogen sulfide gas. Thermochemical sulfate reduction typically occurs in higher temperature regimes of 100 degrees Celsius to 200 degrees Celsius at depths of 2-4 kilometers (Machel, 2001). However, TSR at 25 degrees Celsius has been shown to be thermodynamically possible (Worden and Smalley, 1996). Bacterial sulfate reduction occurs in lower temperatures (0-80 degrees Celsius) and lower depths and has been attributed to the process of calcitization in the Delaware Basin (Kirkland and Evans, 1976). However, TSR would have been possible with elevated geothermal gradients during the Neogene when widespread emplacement of igneous dikes associated with Basin and Range extension occurred (Horak, 1985, Stafford et al, 2008c). Nevertheless, either process (TSR or BSR) can be attributed to calcitization in the study area (Stafford et al, 2008c).

RESISTIVITY

Surface geophysical methods have long been used to characterize the deep subsurface in hydrocarbon and mineral exploration. However, the use of these methods to image shallow subsurface features, up to 30 meters or so, is relatively new (1970's) (Benson and Yuhr, 2015). Today the application of geophysical methods in environmental and geotechnical problems in karst terranes is common (e.g. Zhou et al, 2002; Metwaly and AlFouzan, 2013; Park, 2013; Land and Asanidze, 2015; Benson and Yuhr, 2015).

Resistivity Theory

Resistivity is an intrinsic property of a material. It is measured in Ohms and is dependent on the type of material conducting current and its size. Electrical current is measured in amperes (amps) and by convention it is assumed that current flows from positive (+) to negative (-) through wires. However, to induce a current flow an electrical potential difference is needed; this is typically known as voltage (V). This potential difference is produced by a battery or some other power source, for example a 1.5-volt battery will produce a potential difference of 1.5 volts. As with many materials, including rocks, the current applied through the material is proportional to the voltage. Doubling the voltage will also double the current, this proportion is called Ohms Law (Eq. A1).

The amount of current flowing through a material is called resistance and can vary depending on the material and dimensions. A simplified example would be a copper wire that would have less resistance than a lead wire of the same dimensions, and a long thin wire would have greater resistance than a short thick wire (Mussett and Khan, 2000). (Eq. A2a, A2b).

$$\frac{\text{Potential or voltage difference (volts)}}{\text{current (amps)}} = \frac{V}{I} = \text{resistance } R \text{ (ohms } \Omega) \quad [\text{A1}]$$

$$\text{resistance, } R = \text{resistivity } (\rho) \times \frac{\text{length}}{\text{area of cross-section}} \quad [\text{A2a}]$$

$$\text{resistivity, } \rho = \text{resistance} \times \frac{\text{area of cross-section}}{\text{length}} \quad [\text{A2b}]$$

The main purpose of an electrical resistivity surveying is to measure the relative distribution of resistivity in the subsurface. The resistivity measured can vary and depends on the material in subsurface. Geological parameters such as soil type, mineralogy (rock type), water saturation and porosity also have an effect on the resistivity measured (Loke, 1999). To measure the resistivity of the subsurface, electrical connections are made through metallic electrodes placed a few centimeters into the ground (Figure A7). The current travels from one electrode to the other and is measured with a resistivity meter. In traditional 1-D electrical surveys, four electrodes are placed in the ground with a fixed distance between each electrode. The resistivity measurements are made when current is injected into the ground and the resulting voltage difference is

measured at two potential electrodes. From the values of voltage (V) and current (I), the apparent resistivity can be calculated. The calculated resistivity is not the “true” resistivity, instead it is an “apparent” value based on the geometry of the electrode configuration. To find the “true” resistivity an inversion process must be done using a computer program (Loke, 1999).

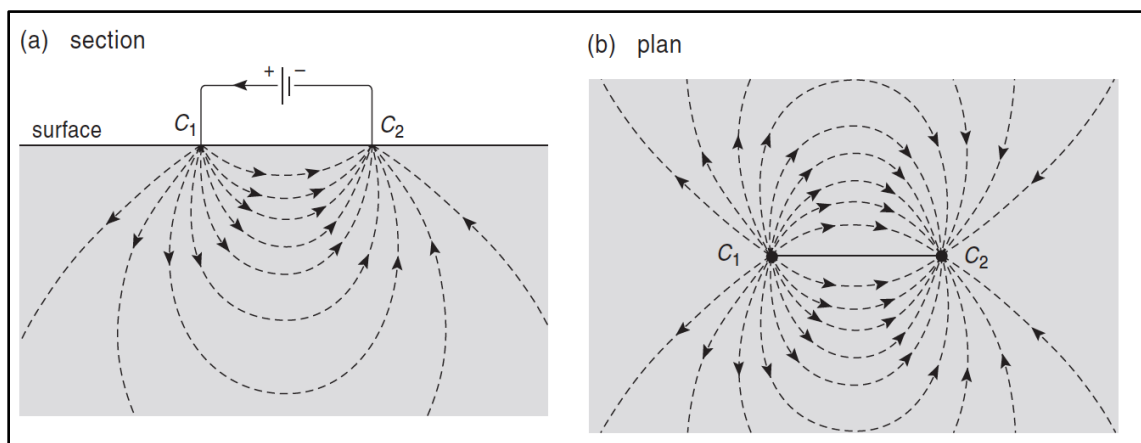


Figure A7. Simplified diagram of electrode placement in a 2-D resistivity survey and current flow paths (from Musset and Khan, 2000)

Two dimensional (2-D) electrical surveys of geologic bodies are a practical and less time consuming way to obtain vertical and horizontal variations in resistivity. The main advantage of a 2-D survey is the high number of measurements taken in a single reading (100-1000) compared to a mere 10-20 readings in a 1-D survey. While 3-D surveys are the most accurate in characterizing geologic features, they are more time consuming and costly (Loke, 1999). There are variety of array configurations, of which each are useful depending on the depth of investigation or the type of geological feature

being studied. The most important and commonly used arrays are Wenner, Schlumberger, and dipole-dipole arrays (Figure A8) (Metwaly and AlFouzan, 2013).

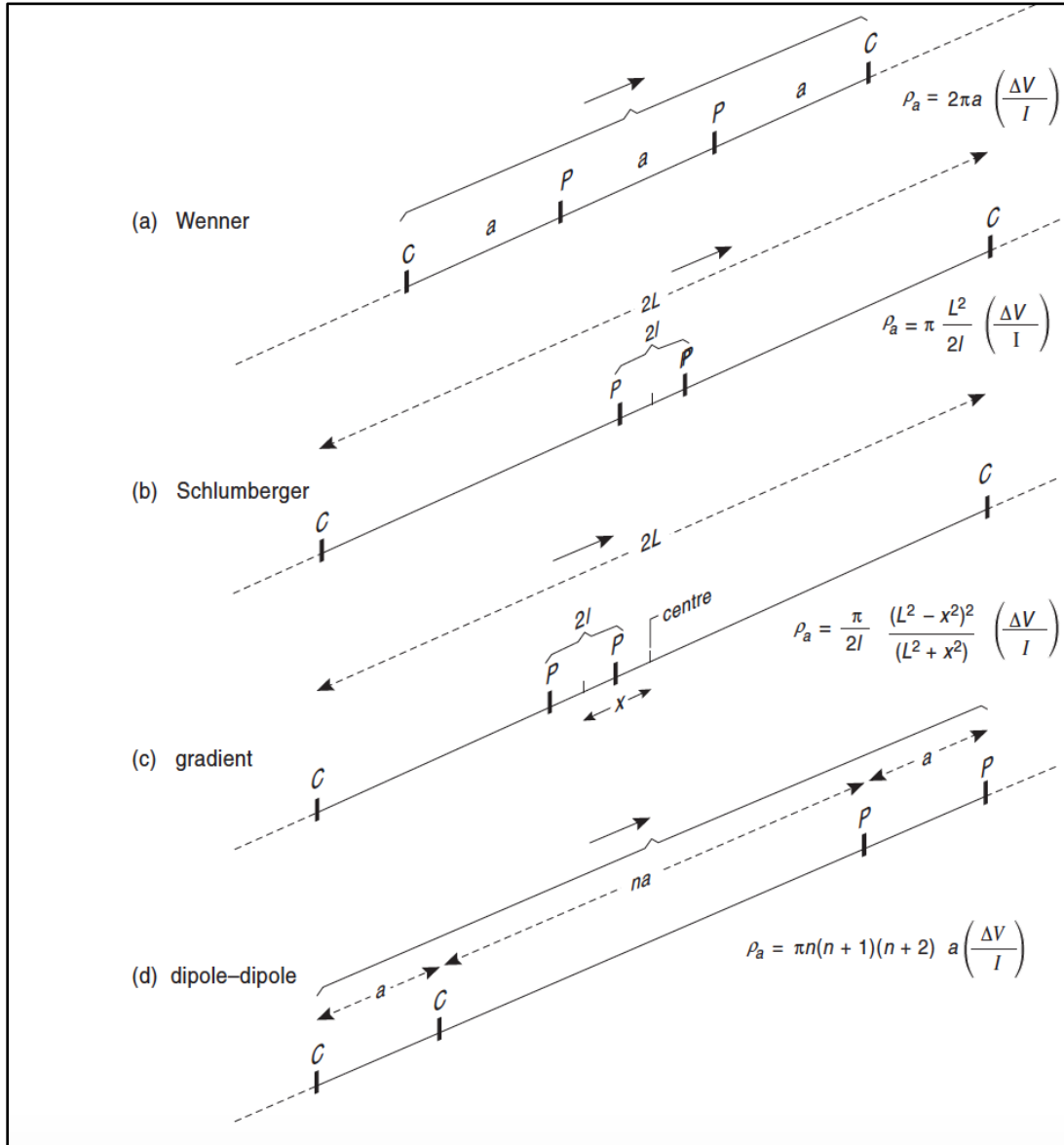


Figure A8. Common array configurations and corresponding geometric factors. **C** is the current electrode and **P** is the potential electrode. Current travels from the **C** electrode and resistivity is measured by the **P** electrode (from Mussett and Khan, 2000).

Wenner arrays involve positioning four electrodes into the ground at equal intervals connected to a resistivity meter. After the measurement is complete, the electrode spacing is then increased progressively throughout the survey and measurements are taken again (Mussett and Khan, 2000). This array set up is more sensitive to vertical changes of resistivity in the subsurface, and less sensitive to horizontal changes, thus increasing vertical resolution but decreasing horizontal resolution (Loke, 1999). Figure A8 section A. shows the electrode configuration of the Wenner array as well as the corresponding geometric factor which describes the geometry of the electrode configuration in the calculation of the apparent resistivity (Mussett and Khan, 2000). The Schlumberger array configuration differs from the Wenner in that potential electrodes (“*P*” electrodes) are spaced closer together, while the current electrodes (“*C*” electrodes) are moved progressively and symmetrically apart. This configuration allows for fewer electrode movement since the *P* electrodes are fixed (Figure A8 section B) (Loke, 1999; Mussett and Khan, 2000).

The dipole-dipole array configuration is widely used in resistivity surveys, especially in groundwater exploration (Figure A8 section D) (Reynolds, 1997). The spacing between the current electrodes and potential electrodes are marked as “*a*.” The other spacing factor is marked as “*na*,” where “*n*” is the ratio between the current electrode *C* and potential electrode *P*. Typically in a dipole-dipole survey the “*a*” spacing remains fixed while the “*n*” factor is increased incrementally to increase the depth of

investigation. The main disadvantage of this type of survey is the small signal strength when the “**n**” factor is large resulting in low resolution at depth. The sensitivity function plot (Figure A9) shows that the largest sensitivity values are between dipole pairs (C1 and C2, P1 and P2) essentially meaning that resistivity changes are more sensitive between these pairs. The sensitivity contour pattern is almost vertical, thus the dipole-dipole array is very sensitive to horizontal changes in resistivity but relatively insensitive to vertical changes. Essentially this means that this array type is good at mapping vertical structures such as cavities and dykes, but poor at mapping horizontal structures such as sills and bedding planes in sedimentary rocks (Loke, 1999).

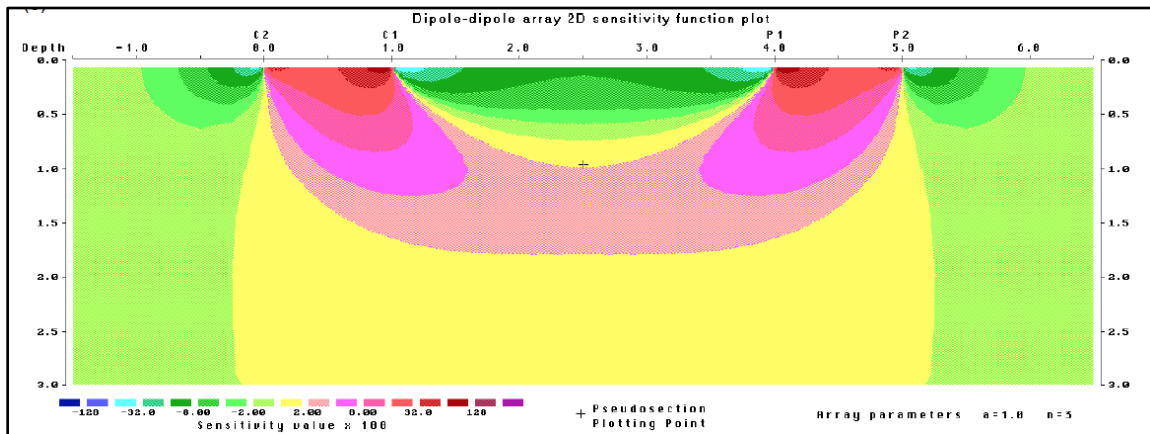


Figure A9. Contour plot showing resistivity sensitivity changes between electrode pairs in a dipole-dipole array (from Loke, 1999).

The choice of array configuration primarily depends on the dimensions of the target: size, shape, depth and resistivity contrast with the surrounding rock. The larger the

electrode spacing, the poorer the resolution both vertically and laterally. (Zhou et. al, 2002; Mussett and Khan, 2000).

Electrical Resistivity and Karst

The application of electrical resistivity to detect and characterize subsurface karst features has been shown to be effective. While other geophysical methods are often used to show karst features such as open cavities and void spaces or the detection of groundwater, electrical resistivity offers greater resolution (Park et al; 2013). According to Park (2013), ground penetrating radar is useful for detecting underground cavities. In a resistivity survey, as current passes through these cavities, which are often filled with water or clay in karst terranes, the resistivity would be much lower than the surrounding host rock, thus allowing for better resolution and better spatial characterization of the cavity.

According to Zhou et al, (2002) the most effective array configuration to characterize and delineate karst geohazards is the dipole-dipole array. In their study, the array configuration for characterizing a collapsed sinkhole along Interstate 70 in Frederick County, Maryland were compared. Among the common arrays (Wenner, Schlumberger, dipole-dipole), dipole-dipole provided the highest precision in locating the sinkhole feature along with the greatest resolution (Figure A10). The author notes that the

one benefit from this type of array configuration is the very high signal to noise ratio (Zhou et. al, 2002).

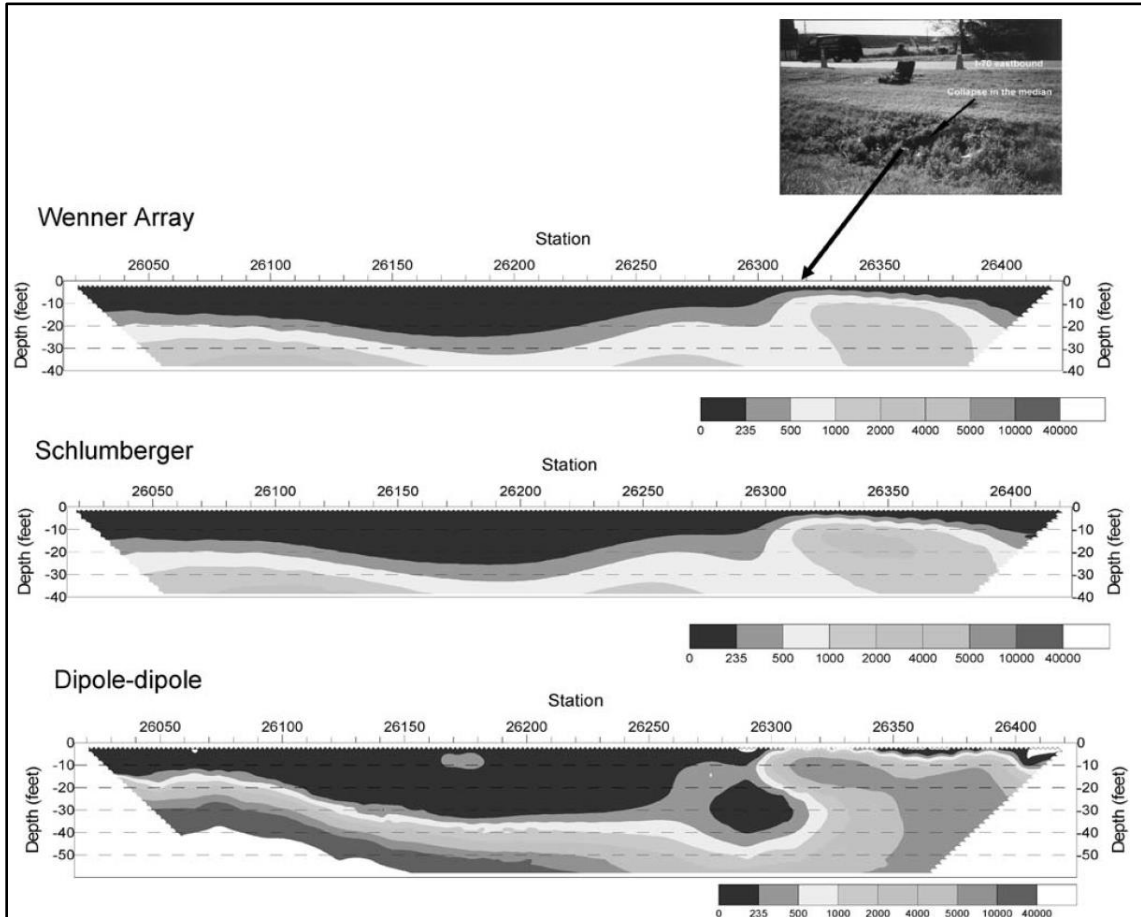


Figure A10. Inverted sections from resistivity survey conducted along interstate 70 in Frederick County, Maryland. Sections show the three common array configurations. Dipole-dipole array was determined to be the most effective in characterizing the sinkhole in the area (from Zhou et al., 2002).

While the dipole-dipole array configuration appears to be best suited for the current study, other examples of successful characterization of karst related features have been achieved using other common array configurations or a combination of them.

Metwaly and AlFouzon (2013) showed that the Wenner-Schlumberger array, where spacing is fixed between potential electrodes and the spacing between current electrodes is logarithmically increased followed by an increase in potential electrodes, was useful in detecting subsurface cavities in a housing development project in eastern Saudi Arabia.

References

- Adams, D.C., Keller, R.G. 1996, Precambrian basement geology of the Permian basin region of west Texas and eastern New Mexico: A Geophysical perspective: AAPG Bulletin, v. 80
- Anderson, R.Y., and Kirkland, D.W., 1980, Dissolution of salt deposits by brine density flow: *Geology*, v. 8, p. 66-69.
- Benson, R.C., and Yuhr, L.B., 2015, Site characterization in Karst and Pseudo-Karst Terraines: Practical strategies and technology for practicing engineers, Hydrologists and geologists: 2016: Netherlands, Springer. 421p.
- Dickinson, W.R., 1981, Plate Tectonic Evolution of the Southern Cordillera; *in* Dickinson, W.R. and Payne, W.D. (eds.), Relations of Tectonics to Ore Deposits in Southern Cordillera: Arizona Geol. Soc. Digest, v. 14, pp. 113-135.
- Horak, R.L., 1985, Trans-Pecos tectonism and its effects on the Permian Basin, in Dickerson, P.W., and Muelberger, W.R., eds., Structure and Tectonics of Trans-Pecos Texas: Midland, Texas, West Texas Geological Society, p. 81–87.
- Hill, C.A., 1996. Geology of the Delaware Basin, Guadalupe, Apache and Glass Mountains: New Mexico and West Texas. Permian Basin Section – SEPM, Midland, TX, 480 p
- Hills, J.M., 1984, Sedimentation, Tectonism, and hydrocarbon generation in Delaware basin, west Texas and southeastern New Mexico: AAPG Bulletin, v. 68.
- Hills, J.M., 1985, Structural Evolution of the Permian Basin of West Texas and New Mexico; *in* Dickerson, P.W. and Muehlberger, W.R. (eds.), Structure and tectonics of Trans-Pecos Texas: West Texas Geol. Soc., Guidebook Publ. 85-81, pp. 89-99
- Kelley, V.C., 1971. Geology of the Pecos Country, Southeastern New Mexico. New Mexico Bureau of Mines and Mineral Resources, Socorro, NM, 78 p.
- Douglas W. Kirkland (2), Robert Eva, 1976, Origin of limestone Buttes, gypsum plain, Culberson county, Texas: AAPG Bulletin, v. 60.

- Kirkland, D.W., 2003, An explanation for the varves of the Castile evaporites (upper Permian), Texas and New Mexico, USA: *Sedimentology*, v. 50, p. 899–920.
- Keith, S.B., 1978, Paleosubduction geometries inferred from Cretaceous and tertiary magmatic patterns in southwestern north America: *Geology*, v. 6, p. 516–521.
- Keith, S.B., 1982, Paleoconvergence rates determined from K₂O/SiO₂ ratios in magmatic rocks and their application to Cretaceous and tertiary tectonic patterns in southwestern north America: *Geological Society of America Bulletin*, v. 93, p. 524-532.
- King, P.B., 1942, Permian of west Texas and southeastern New Mexico: PART 1: *AAPG Bulletin*, v. 26.
- Klimchouk, A., and Andrejchuk, V., 1996, Environmental problems in gypsum karst terrains: *International Journal of Speleology*, v. 25, p. 145–156
- Klimchouk, A., 2000, Speleogenesis in gypsum. In: Klimchouk A., Ford D.C., Palmer A.N. & Dreybrodt W. (Eds.) *Speleogenesis: evolution of karst aquifers*. Huntsville, National Speleological Society: p. 261-273.
- Klimchouk, A., and Andrejchuk, V., 2002, Karst breakdown mechanisms from observations in the gypsum caves of the western Ukraine: Implications for subsidence hazard assessment: *International Journal of Speleology*, v. 31, p. 55–88.
- Land, L., and Asanidze, L., 2015, Rollalong Resistivity Surveys Reveal Karstic Paleotopography Developed on Near-Surface Gypsum Bedrock: *Proceedings of the Fourteenth Multidisciplinary Conference on Sinkholes and the Engineering and Environmental Impacts of Karst*, v. NCKRI Symposium 5.
- Loke, M.H., 1999, *Electrical imaging surveys for environmental and engineering studies: A practical guide to 2-D and 3-D surveys*. 63p.
- Machel, H., 2001, Bacterial and thermochemical sulfate reduction in diagenetic settings- old and new insights: *Sedimentary Geology*, v. 140, p. 143–175.
- Metwaly, M., and AlFouzan, F., 2013, Application of 2-D geoelectrical resistivity tomography for subsurface cavity detection in the eastern part of Saudi Arabia: *Geoscience Frontiers*, v. 4, p. 469–476

- Mussett, A.E., and Khan, A.M., 2000, *Looking into the earth: An introduction to geological geophysics*: Cambridge, Cambridge University Press.
- Palmer, A.N., 2006, *Cave geology*: Dayton, OH, Cave Books.
- Niederleithinger, E., Weller, A., and Lewis, R., 2012, Evaluation of Geophysical techniques for dike inspection: *Journal of Environmental & Engineering Geophysics*, v. 17, p. 185–195.
- Park, M.K., Park, S., Yi, M.-J., Kim, C., Son, J.-S., Kim, J.-H., and Abraham, A.A., 2013, Application of electrical resistivity tomography (ERT) technique to detect underground cavities in a karst area of South Korea: *Environmental Earth Sciences*, v. 71, p. 2797–2806
- Reynolds, J.M., 1997, *An introduction to applied and environmental geophysics*: New York, John Wiley & Sons. p. 418-490
- Scholle, P.A., Goldstein, R.H., and Ulmer-Scholle, D.S., 2004, *Classic Upper Paleozoic Reefs and Bioherms of West Texas and New Mexico*. New Mexico Institute of Mining and Technology, Socorro, NM, 166p.
- Stafford, K.W., 2015, *Evaluation of Existing Geologic Conditions along RM 652: Initial Characterization of Karst Geohazards Associated with RM 652 in Culberson County, Texas*: TxDOT rep., p. 1–71.
- Stafford, K., Nance, R., Rosales-Lagarde, L., and Boston, P., 2008a, Epigene and hypogene gypsum karst manifestations of the Castile Formation: Eddy County, New Mexico and Culberson County, Texas, USA: *International Journal of Speleology IJS*, v. 37, p. 83–98.
- Stafford K.W., Rosales-Lagarde L. & Boston P.J., 2008b, Castile evaporite karst potential map of the Gypsum Plain, Eddy County, New Mexico and Culberson County, Texas: a GIS methodological comparison. *J. Cave and Karst Studies*. p. 83-98.
- Stafford, K.W., Ulmer-Scholle, D., and Rosales-Lagarde, L., 2008c, Hypogene calcitization: Evaporite diagenesis in the western Delaware Basin: *Carbonates Evaporites Carbonates and Evaporites*, v. 23, p. 89–103.
- Worden, R.H., and Smalley, P.C., 1996, H₂S-producing reactions in deep carbonate gas reservoirs: Khuff formation, Abu Dhabi: *Chemical Geology*, v. 133, p. 157–171.

Zhou, W., Beck, B., and Adams, A., 2002, Effective electrode array in mapping karst hazards in electrical resistivity tomography: *Environmental Geology*, v. 42, p. 922–928

APPENDIX B
METHODOLOGY

METHODS

Electrical resistivity data for this study was collected using a Super Sting R8 resistivity meter produced by *Advanced Geosciences Inc.* All resistivity data was collected along RM652 in Culberson County, Texas (Figure B1). The Super Sting R8 resistivity meter is an eight channel multi-electrode earth resistivity meter (AGI, 2005). (Figure B2). Resistivity data was collected using a dipole-dipole array type with the 56 electrodes at 1-meter, 2-meter or 4-meter electrode spacing. Survey lengths were dependent on the desired depth of investigation and the resolution required to delineate karst features (Table: B1). All data were processed using AGI EarthImager 2-D inversion software.

Command Files

Prior to collecting field data; survey parameters were created in the administrator software provided by Advanced Geosciences (Figure B3). Essentially, this software produced a command file that was downloaded to the instrument via a data cable from a P.C. This command file contained important survey parameters such as array type, number of electrodes, and spacing between current and potential electrodes. For this study, 56 electrodes were deployed at each survey site with a maximum spacing of 6 and a minimum spacing of 1 between transmitting “C1 and C2” and receiving electrodes “P1

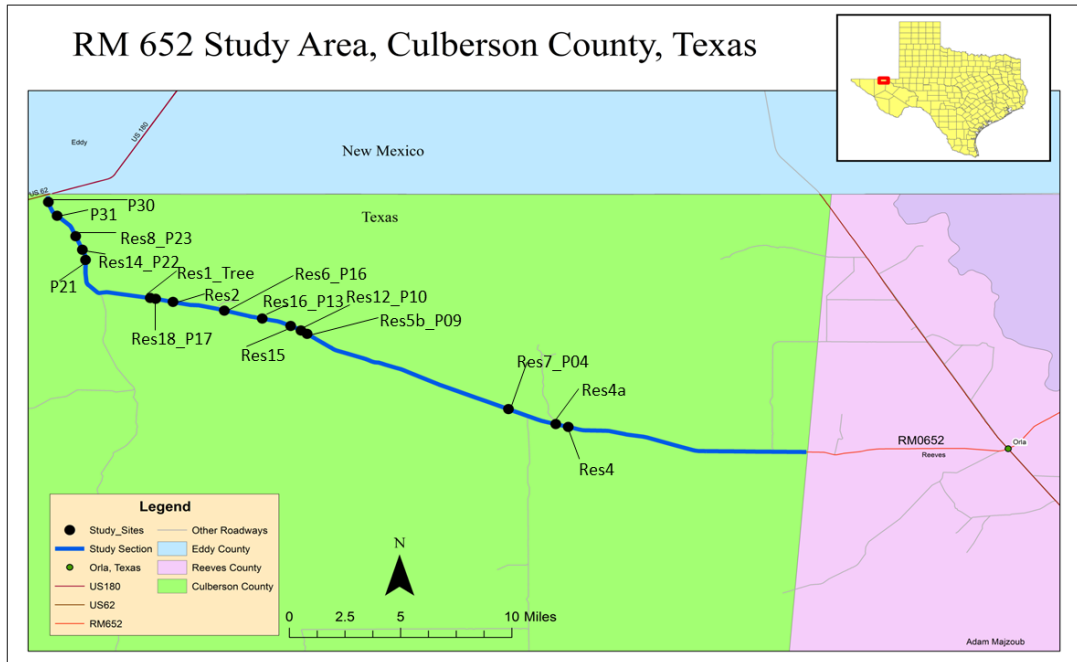


Figure B1: Map of study area and approximate locations of each resistivity survey.

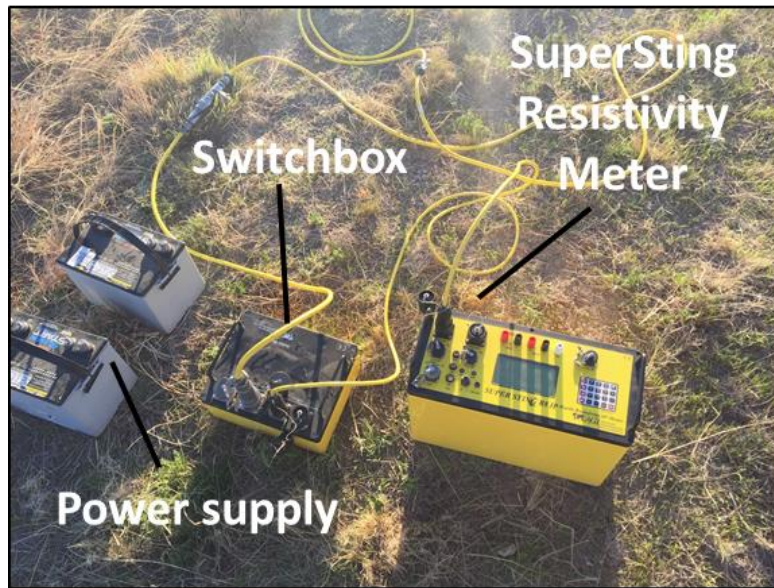


Figure B2: Super Sting R8 resistivity meter produced by Advanced Geosciences. Image shows the SuperSting console, switchbox, and marine batteries for power supply. Cables are connected to electrodes along a survey line (not shown).

Table B1: Survey site and field parameters.

Site	Electrode spacing	Survey length	Description
P30	2 meters	110 meters	
P31	2 meters	110 meters	
Res8_p23	1 meter	195 meters	Roll-along survey
Res8_P23	4 meter	220 meters	
Res14_P22	2 meters	110 meters	
P21	2 meters	110 meters	
Res1_Tree	2 meters	110 meters	
Res1_Tree	4 meters	220 meters	
Res18_P17	2 meters	110 meters	
Res2	1 meter	109 meters	Roll-along survey
Res2	4 meters	220 meters	
Res6_P16	4 meters	220 meters	
Res16_P13	2 meters	110 meters	
Res16_P13	2 meters	110 meters	50 percent overlap
Res15	2 meters	110 meters	
Res12_p10	4 meters	220 meters	
Res5b_P09	2 meters	110 meters	
Res5b_P09	4 meters	220 meters	
Res7_P04	2 meters	110 meters	
Res4a	4 meters	220 meters	
Res4	2 meters	110 meters	

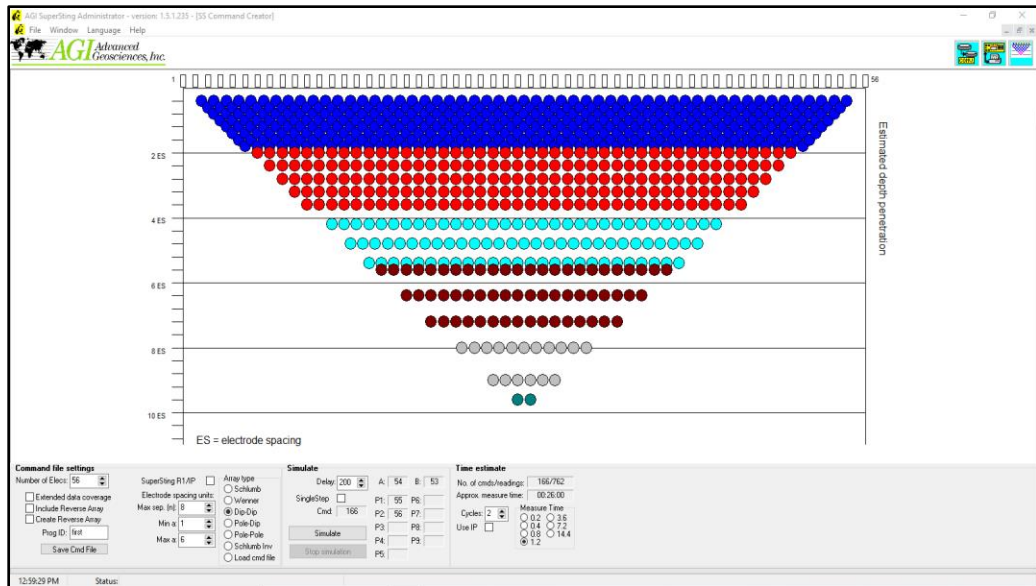


Figure B3: Parameters for dipole-dipole survey set with the command file creator option in Advanced Geosciences administrator software. Image shows a simulated version of survey data collected with the given parameters.

and P2” (Figure B4). Common nomenclature refers to this spacing factor as “*a*” spacing. The maximum “*n*” is the spacing ratio between “C1 and P1” electrodes to the “C2 and C1” or “P1 and P2” dipole separation, this was set to 8. For dipole-dipole arrays, the “*a*” spacing is initially kept fixed and gradually increased along with the “*n*” factor to allow for greater depth penetration (Loke, 1999).

The spacing between dipole-dipole pairs is independent of the actual electrode spacing used in the field. One benefit of the Super Sting system is that the parameters set in the command file fully dictate the geometry of the survey which are executed automatically; hence repositioning electrodes in the field is not required and saves a great deal of time.

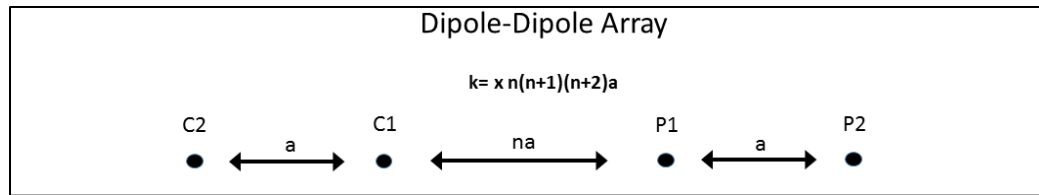


Figure B4: Simplified electrode configuration for dipole-dipole array. k represents the geometric factor. Where “ n ” is the distance ratio between dipole separation, and “ a ” is the spacing between transmitting and receiving electrodes.

Data Acquisition

Survey lengths were determined based on the road patch length and observable karst related features along the shoulder of the road. A tape measure was used to determine the midpoint of each site and depending on survey length, the beginning and ending points were marked using spray paint. Upon deciding survey length, the tape measure was extended 26, 56, or 112 meters from the midpoint in either direction. This was done to ensure karst features, or road maintenance features related to karst breakdown, were in the center of the survey. Stainless steel stakes (electrodes) were hammered into the ground at 1 meter, 2 meters, or 4 meters depending on the length of the survey. All data was collected using only 56 electrodes. Provided cables were then laid out and connected to each electrode.

Field Setup

For the purposes of this study, only four cable sections were used. Cable connectors are numbered in sequential order 1-56 and are divided into the four sections of cable. Cables 1-14 and 15-28 represent the low address section and 29-42 and 43-56 the

high address section. The Super Sting resistivity meter was placed at the low address section for all surveys (Figure B5 and B6).

The command file created prior to field survey setup defines the type of survey conducted however certain parameters were required to be programmed in the SuperSting resistivity meter system prior to collecting data. These parameters included configuration of electrode spacing and whether the survey was a roll-along survey or not. All other settings were set to factory defaults. For all surveys these defaults were set to 1.2 seconds

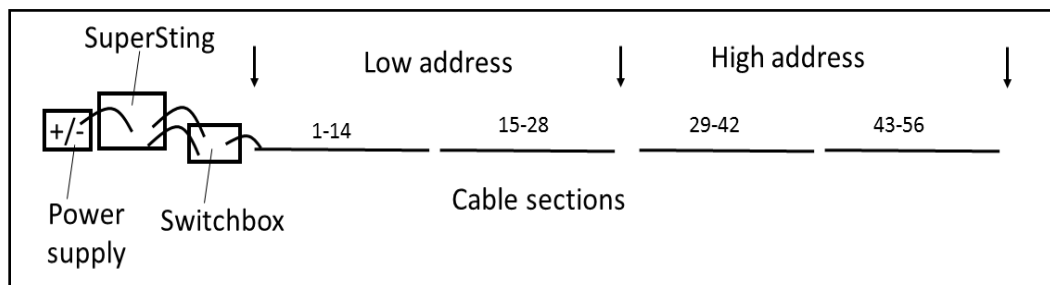


Figure B5: Schematic of in field survey setup. Resistivity meter and switchbox were placed at the low address section. The switchbox, produced by Advanced Geosciences, allows for positioning of resistivity meter at the low address section rather than middle of survey.

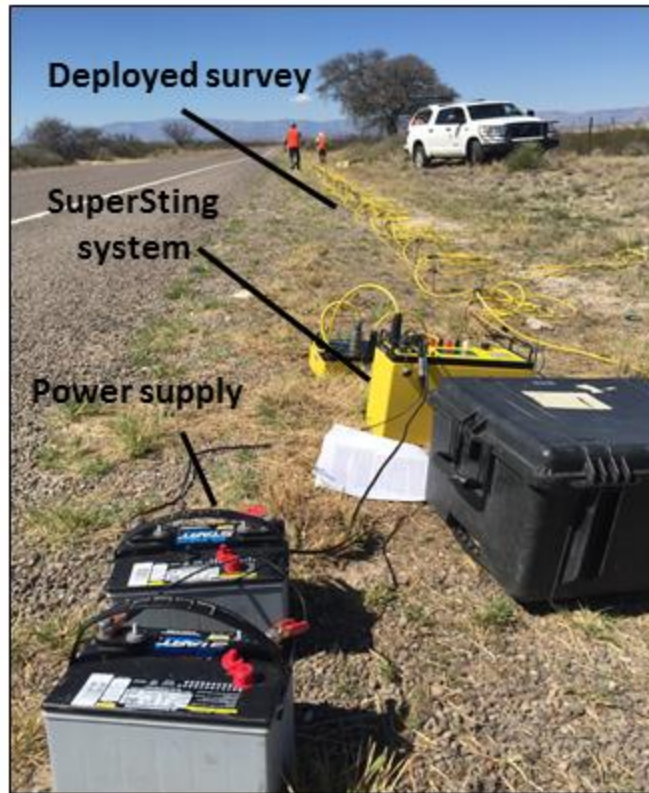


Figure B6: Annotated photo of in field 56-electrode setup along survey site.

measurement time with 2 measurement cycles at each electrode pair. The maximum error threshold between measurement cycles was set to 2% and injected current for each measurement was set to a maximum of 2000mA. Cable address sections were programmed in sequential order according to the survey layout, see figure B4. Quality control steps such as performing a contact resistance test and watering the electrodes with saline solution were conducted at each site. The contact resistance test is a feature of the SuperSting which allows the user to check the quality of electrical coupling with the ground. If contact resistance was too high (>2000 ohms) at a particular electrode, it was

either repositioned or more firmly planted in the ground. Two-thousand-ohm threshold for contact resistance is applicable to most earth resistivity surveys (AGI, 2005).

Roll Along Surveys

One-meter roll-along surveys were conducted at two sites *Res 2 and Res 8_P23*, see figure B1 and table B1, where site coverage at depth, resolution and shallow depth penetration were important for the study. Figure B7 is a schematic of how the survey was carried out. The main survey was conducted at 56 meters in length and 1-meter electrode spacing. Once the survey was complete the low address section (1-28) was moved to the end of the high address section (29-56) at which point the survey was conducted in the new location. The survey line was advanced in this process until the desired length of the section was achieved.

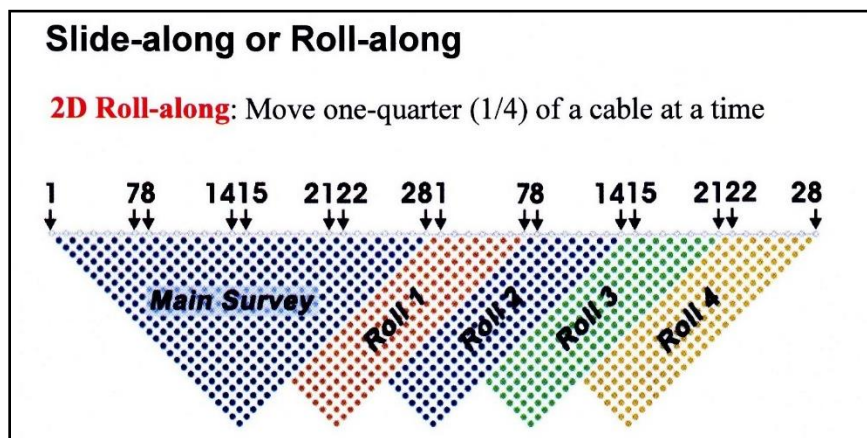


Figure B7: Schematic of roll-along survey. Figure shows advancement at 25 percent or one quarter of survey length. In this study, roll-along was advanced 50 percent or half the survey length (AGI, 2016).

On average features smaller than half the electrode spacing width are not completely resolved in the inverted sections (AGI, 2016); therefore, the necessity to conduct this type of survey allowed for more effective interpretation of the scope and nature of karst features and their overall impact on road sections.

Survey at site *Res 16_P13*, see figure B1 and table B1, was conducted with a 50 percent overlap to ensure total length of site was measured. This type of survey is different than a roll-along survey in that two separate surveys are conducted rather than just one continuous survey (Figure B8).

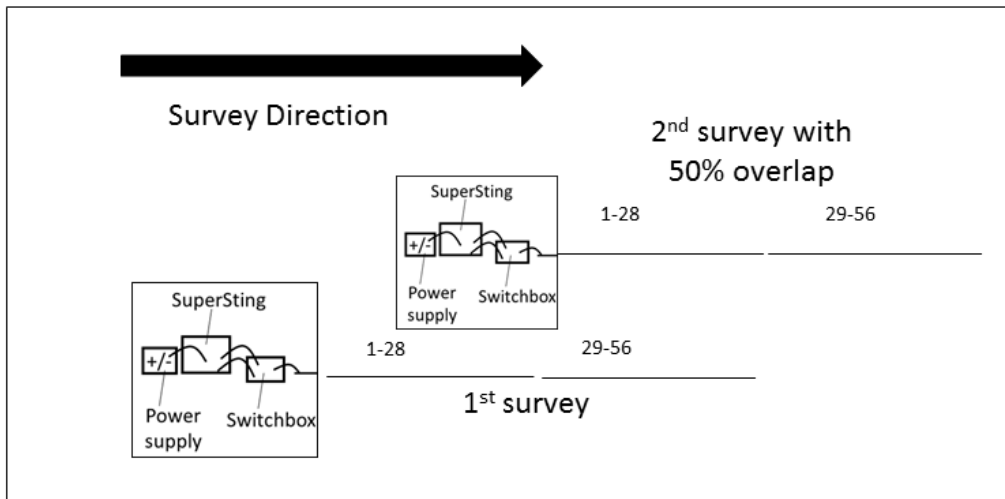


Figure B8: Schematic of survey with 50 percent overlap at site *Res16_P13*. Total length is 220 meters at 2-meter electrode spacing.

Data Processing

All electrical resistivity data obtained in this study was processed using Earth Imager 2D version 2.4.4 produced by Advanced Geosciences Inc. Terrain corrections

were applied to all inverted sections to more accurately represent the topography of each survey site.

Pseudo sections

Data collected from each site was uploaded to a personal computer from the SuperSting system. Raw data that is read in EarthImager 2D is displayed as a pseudo-section. The pseudo-section represents a relative distribution model of the apparent resistivity values collected in the field. For a true earth resistivity model, the data must be inverted to give a more accurate resistivity distribution. The settings in EarthImager 2D determine the criteria by which the software produces an inverted model showing true subsurface resistivity. In this study all data was inverted using a smooth model inversion, also known as Occam's inversion, which is a method to find the smoothest possible model which fits the collected data. Smooth model inversion is convenient for most resistivity data and the software readily allows the user to select the type of survey which presets all criteria and inversion parameters. In this study *Surface* settings were used (Figure B9 and B10).

Data Misfit

Data collected in the field did not always match the model produced through the inversion process, thus increasing the Root Mean Squared (RMS) error. In most cases, noise in the data collected was attributed to either background magneto-tellurics, surface contact resistance, and/or surrounding anthropogenic features such as wire fences and

pipelines. This type of noise is automatically accounted for in the settings and less weight is given to it in the inverted section, this is done by applying a 3% estimated noise

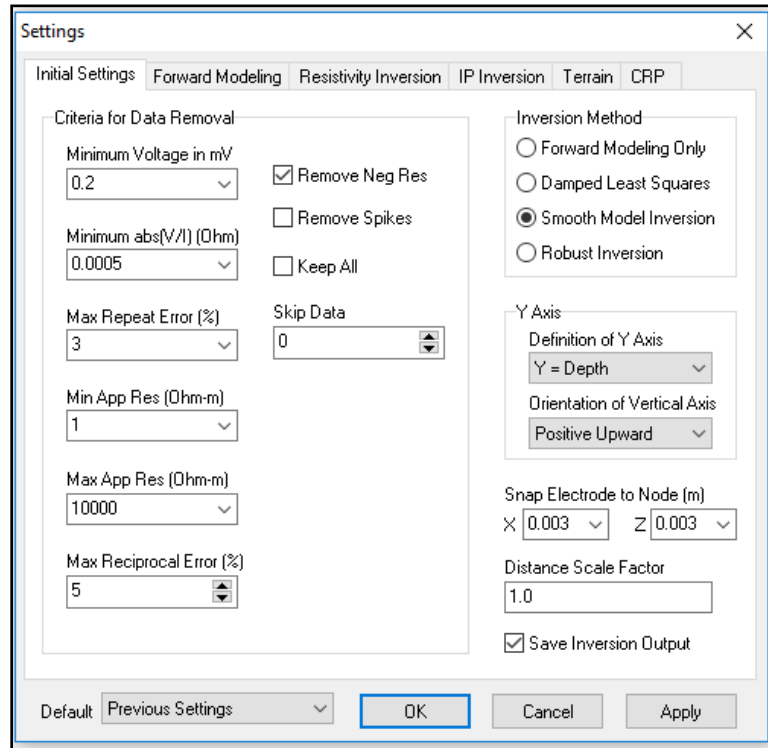


Figure B9: Initial settings from EarthImager 2D. All criteria and parameters for inversion are set to default *Surface* settings which is recommended for most resistivity data.

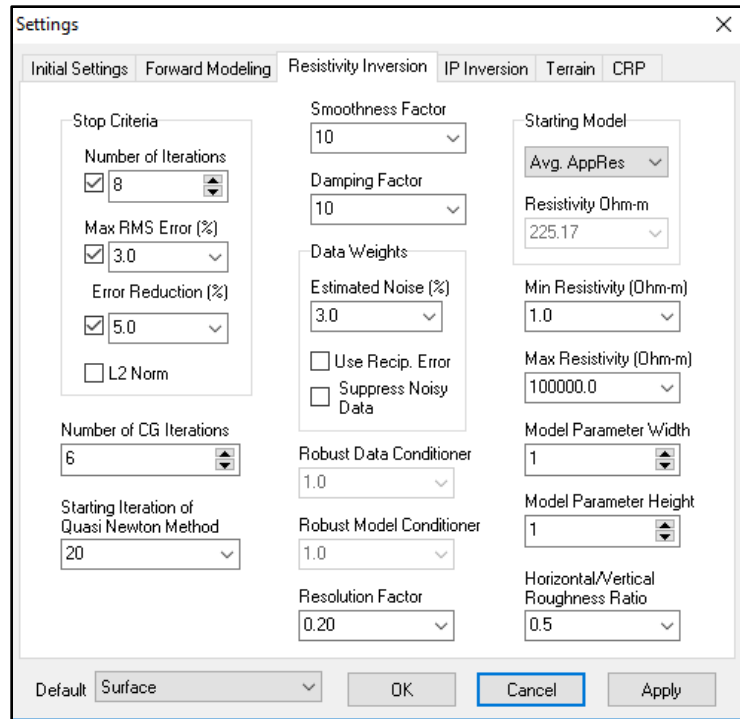


Figure B10: Image shows inversion settings for all data collected in this study. All settings are default *surface* settings in Earth Imager.

threshold in the inversion settings, *see figure B10*. However not all noise is filtered out using this setting. Poorly fitted data were manually removed based on the relative distribution of misfit observed in the *data misfit histogram* which is automatically generated after the inversion has fully converged (Figure B11). Removal of too much data could produce inconsistencies and artifacts in the inverted sections, therefore, misfit data was removed incrementally before running the inversion process again. This process was repeated until the root mean squared error was reduced to an acceptable level $<10\%$, for this study. In order to verify the accuracy of the inverted model, a data misfit cross

plot was generated for each site. The misfit cross plot is a graphical representation of the data collected (apparent resistivity) values versus the predicted values (Figure B12).

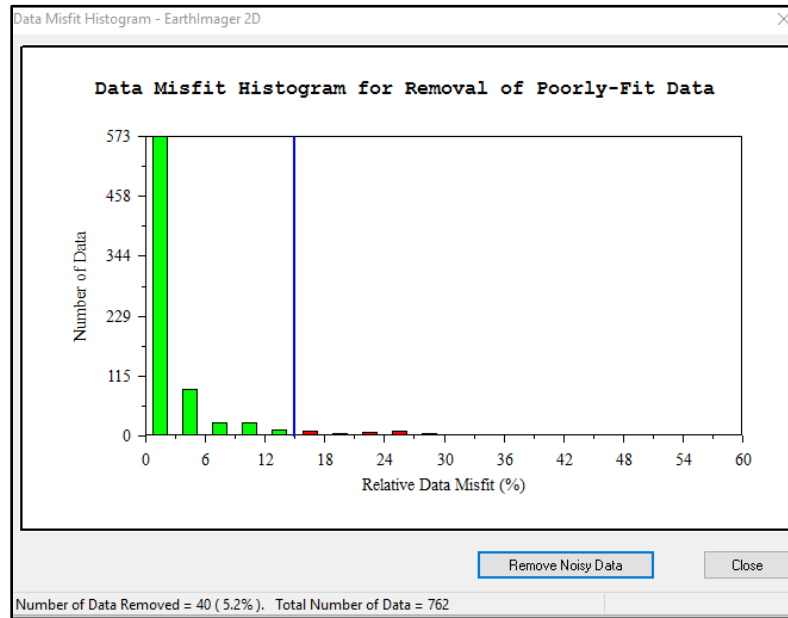


Figure B11: Data misfit histogram for site *Res16_P13*. Image taken from EarthImager 2D inversion software. Blue vertical line is adjustable and marks the threshold of data misfit removal.

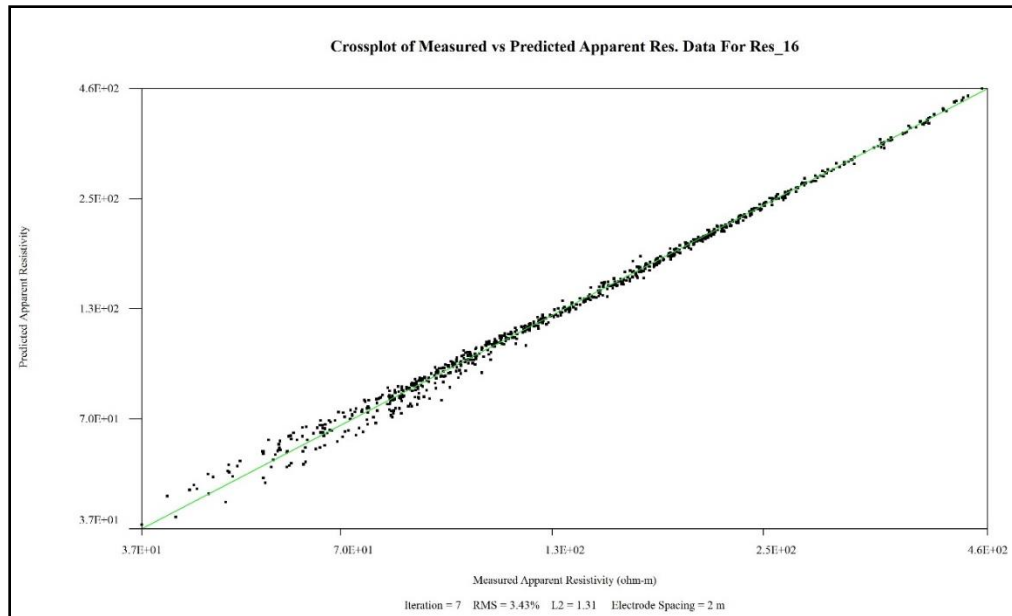


Figure B12: Data misfit cross plot for site *Res16_P13*. Data points are plotted along a best fit line which is the predicted apparent resistivity ‘y-axis’ versus the measured apparent resistivity ‘x-axis’

Terrain Correction

In order to more accurately interpret the data, a terrain correction was applied to all sites in this study. Aerial photos were taken with a DGI Phantom drone to more accurately assess the start and endpoints of each survey. Approximate locations of each survey were then digitized on a high resolution aerial photo of the study area in ArcGIS. A digital elevation model was produced with LIDAR data collected over the study area and layered with the map of the digitized survey lines. Fifty-six points were constructed across each survey line using the drawing tool in ArcGIS. These points represent approximate electrode locations which were spaced at either 1 meter, 2 meters, or 4 meters, elevation values were extracted from the points using the *extract values by points* tool. Elevation values for each site were exported and formatted in *Microsoft Notepad*

according to the terrain file format used by Earth Imager 2D (Figure B13). The terrain file is read prior to running the inversion, and is automatically applied to the inverted section profile.

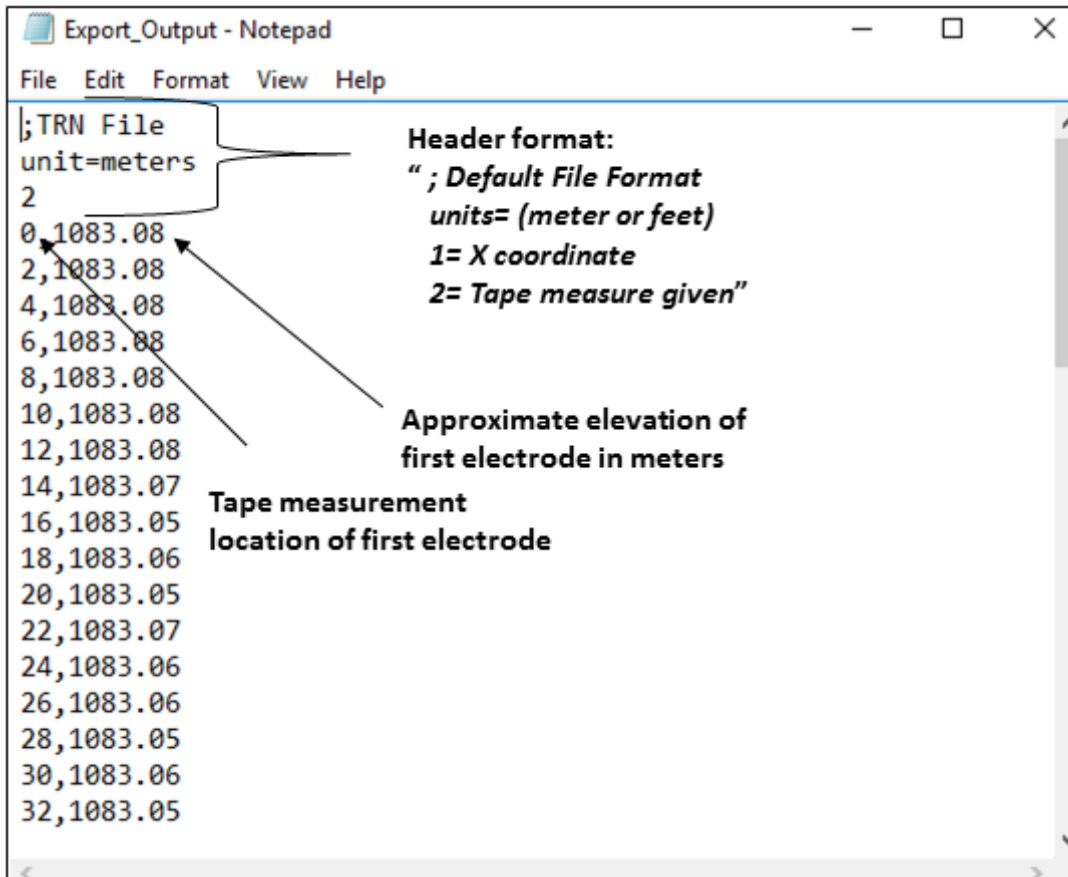


Figure B13: Terrain file for site *Res16*. Elevation data was extracted from DEM of study area in ArcGIS. Tape measurement locations of each electrode were inputted (2-meter increments) followed by approximate elevation in meters from DEM.

REFERENCES

- AGI, 2005. Instruction manual for the SuperSting with Swift automatic resistivity and IP system: Austin, TX, Advanced Geosciences, Inc., 87 p.
- AGI, 2016. Seminar on resistivity imaging, AGI Resistivity Imaging Seminar, Sept. 7-9, Austin, TX.
- Loke, M.H.,1999, Electrical imaging surveys for environmental and engineering studies: A practical guide to 2-D and 3-D surveys. 63p.

APPENDIX C
RESULTS AND SITE DESCRIPTIONS

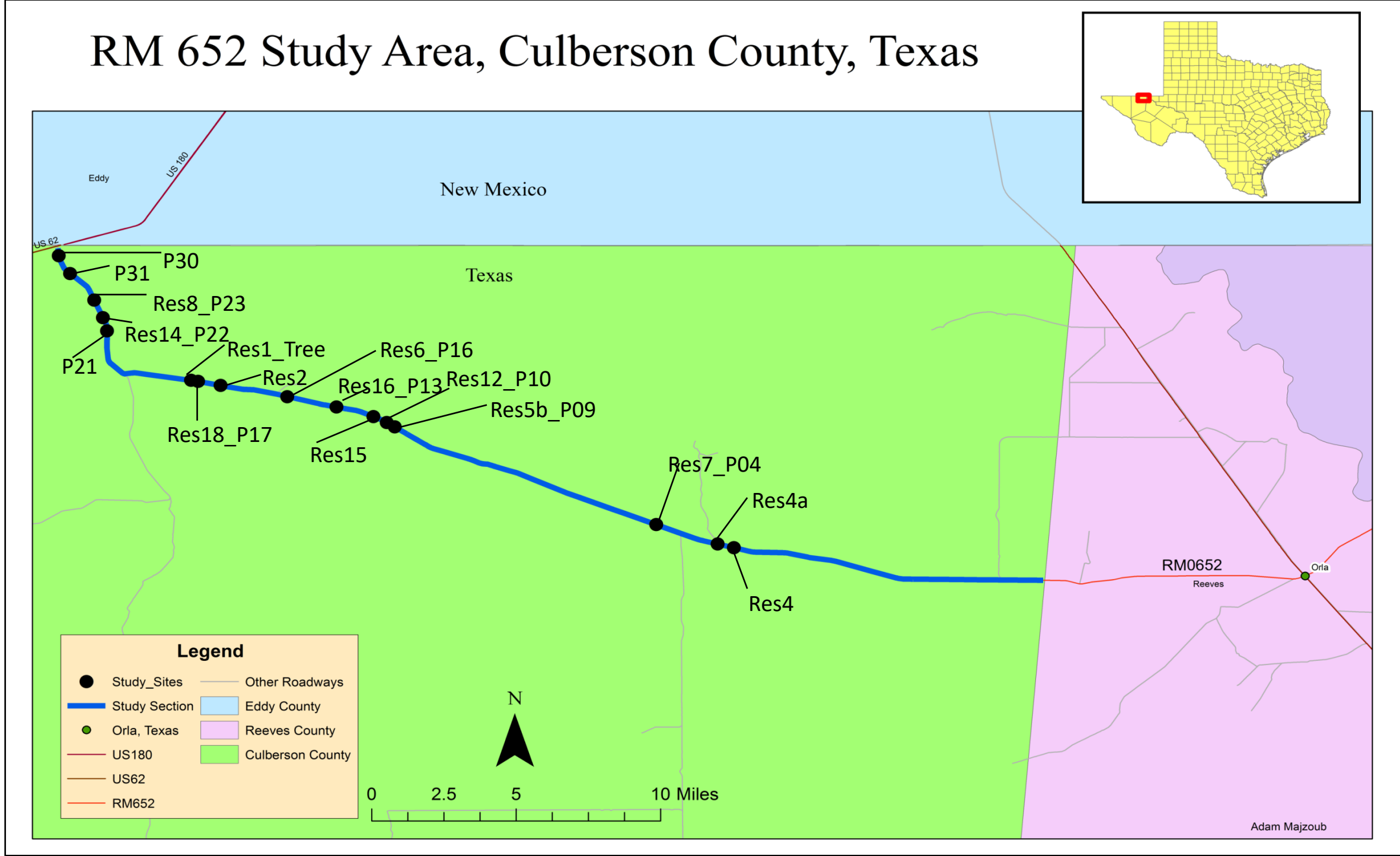
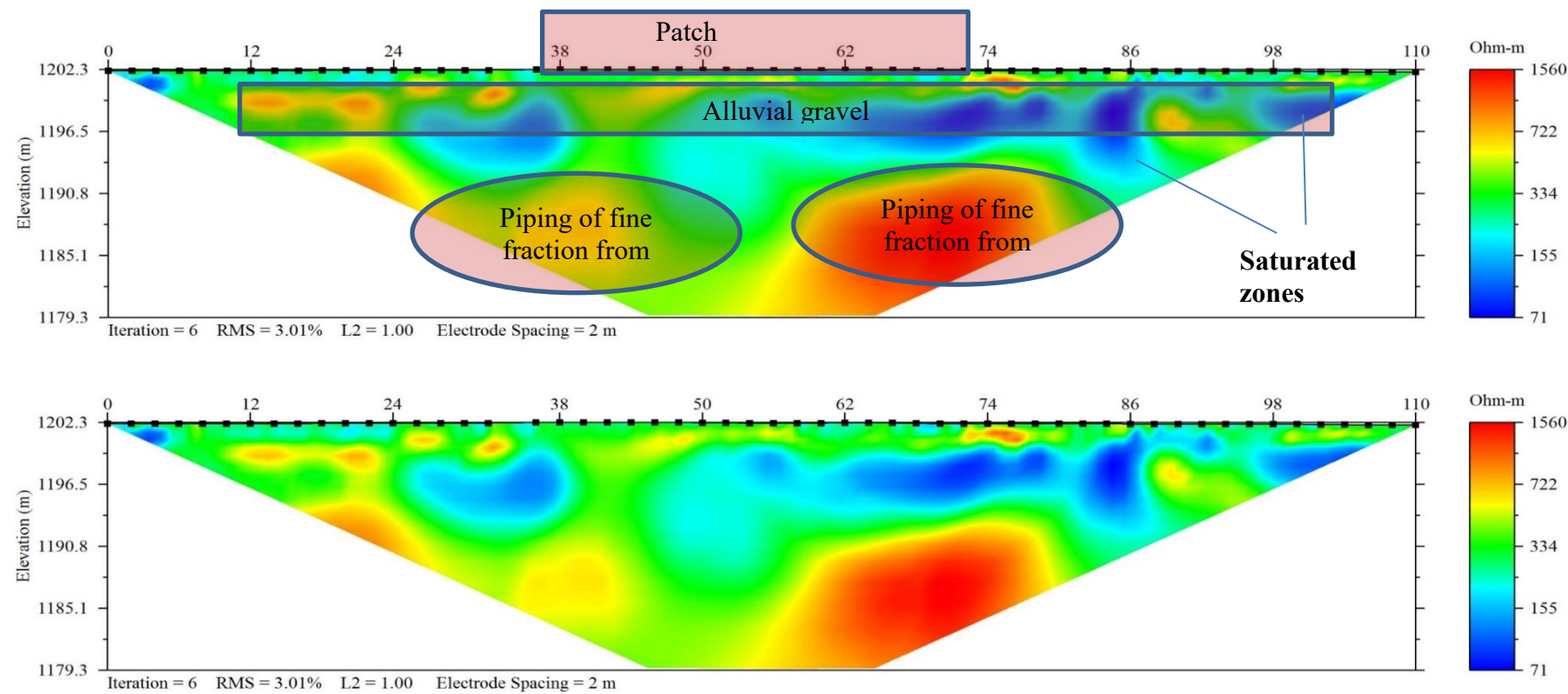
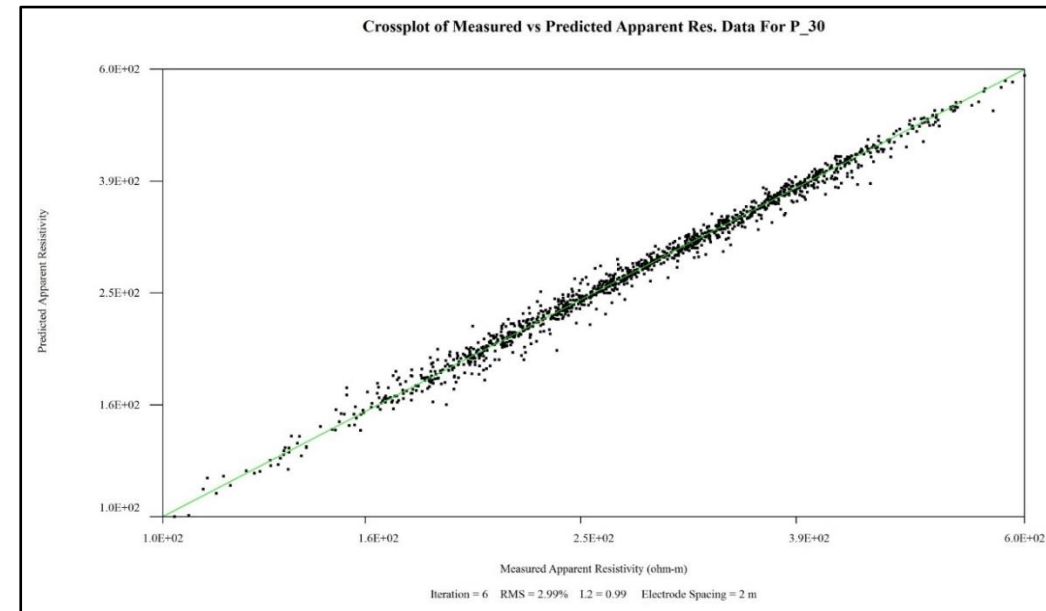
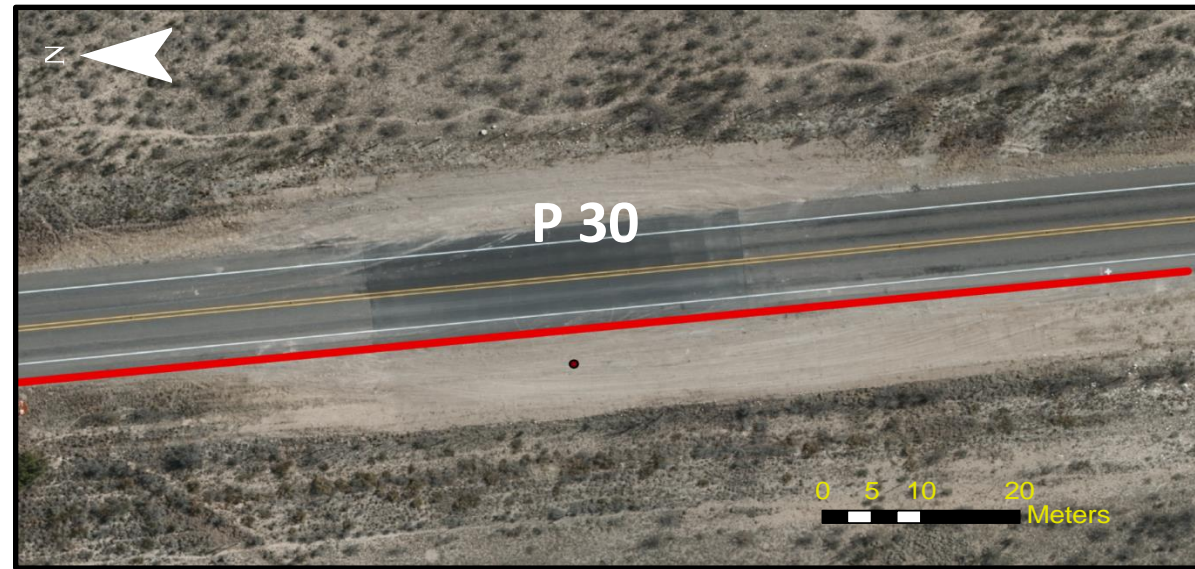
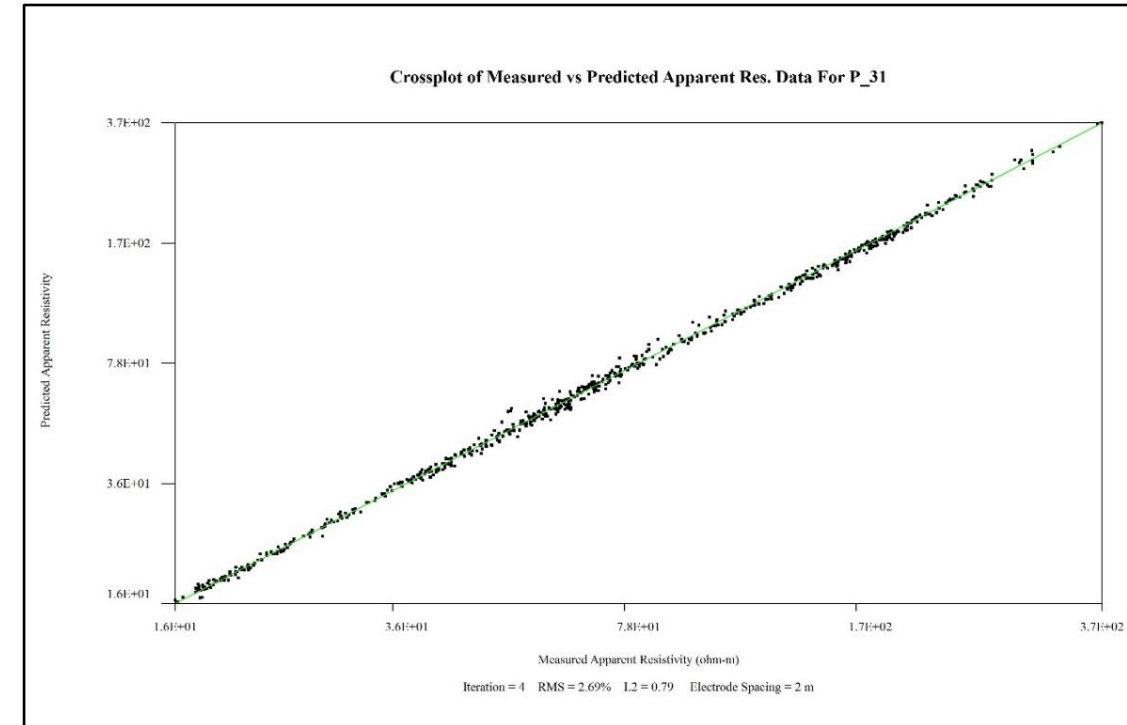


Figure C1: Map of study area showing approximate location of each resistivity survey site.

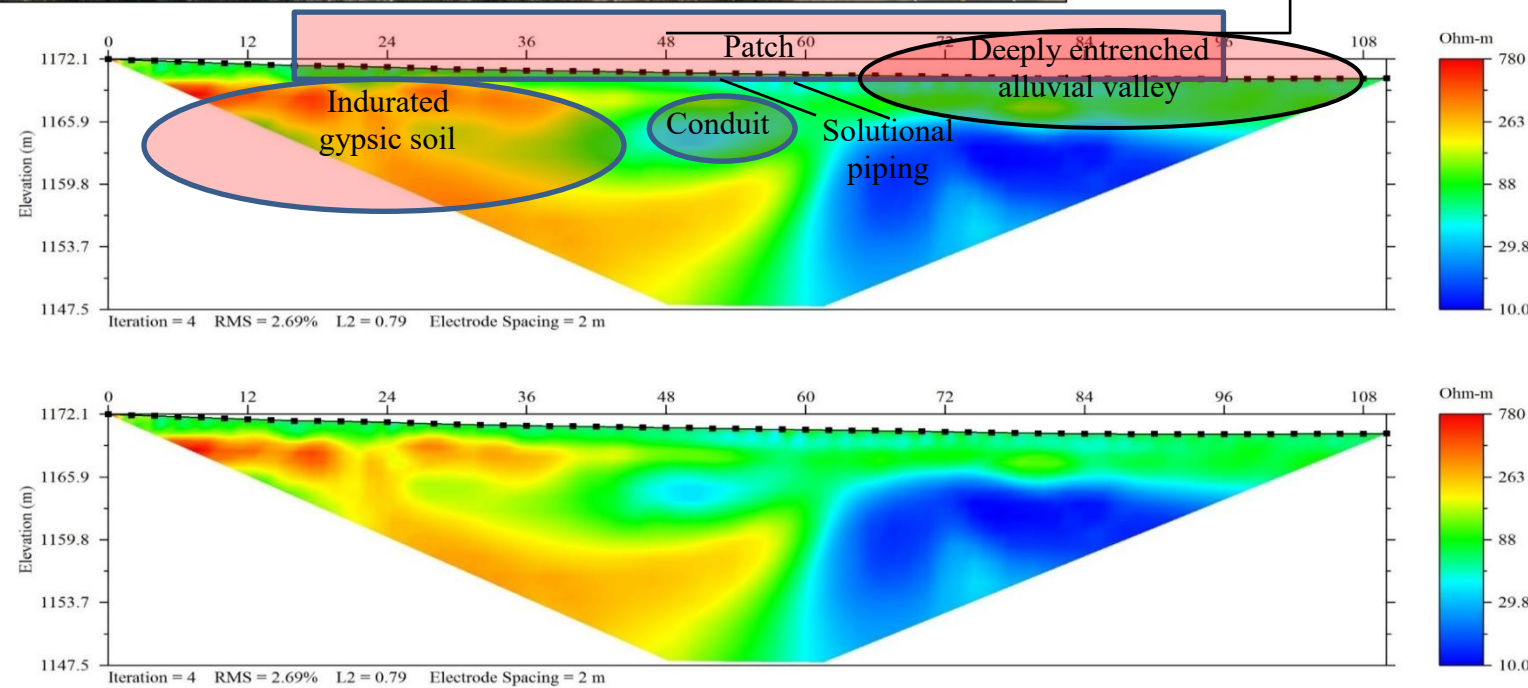


Description:
 This site is located on an alluvium plain. Piping of fine fraction from gravel begins at around 7-9 meters creating porous zones resulting in higher resistivity. Patch in the road is from meter 36 to meter 70. The saturated zones indicate preferential flow paths of moisture from the surface.

Figure C2: Survey site P 30. 56 electrode dipole-dipole array with 2-meter spacing (total length 112 meters). Note that maximum resistivity reading in inverted sections is 1560 ohm-m. RMS error 3.01%



Enhanced
compression



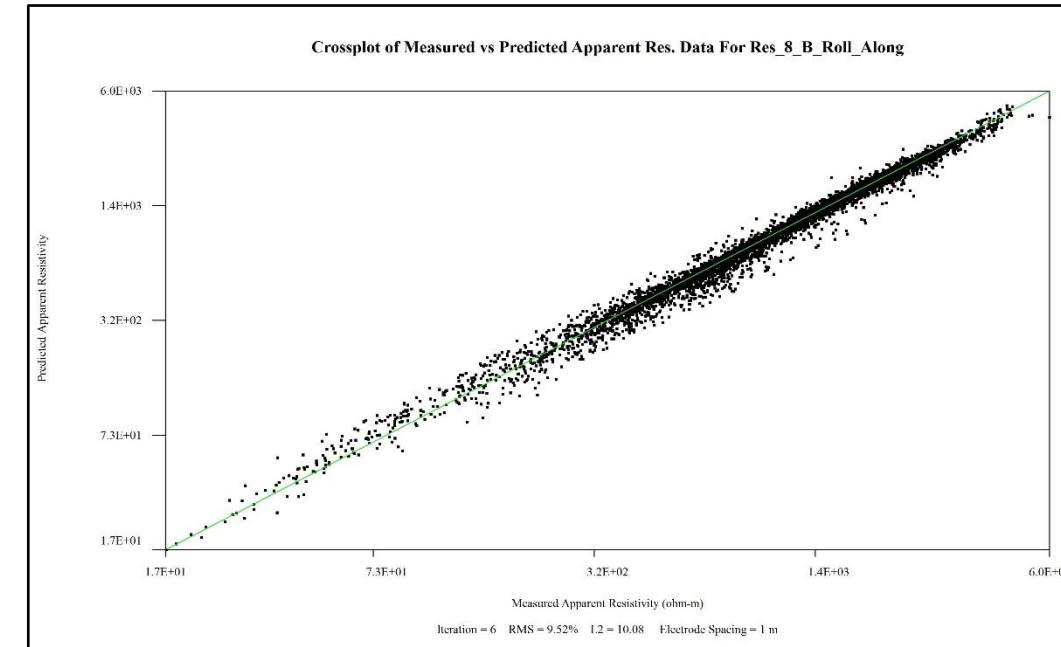
Description:

Survey is west to east in eastbound land. Zone of relatively high resistivity from 0 to 48 meters consists of indurated (hardened) gypsic soil overlying gypsum bedrock.

Centered on the patch is a zone of solutional piping at the transition to a continuous zone of moderately low resistivity. This zone can be interpreted as an area of enhanced compression due to dewatering of alluvial sediments.

Low resistivity region is interpreted as filled solutional valley. Maximum differential compression occurs at transition between bedrock and moisture rich alluvial fill. Piping at margin of transition likely associated with additional solutional conduit development.

Figure C3: Survey site P 31. 56 electrode dipole-dipole array with 2-meter spacing (total length 112 meters). Note that maximum resistivity reading in inverted sections is 780 ohm-m. RMS error 2.69%



Description:

Roll-along survey in westbound lane. Survey is northwest to southeast. From 0 to 50 meters (lower elevation) is a saturated zone with enhanced dissolution in the subsurface. Dissolution is more prominent between 40-50 meters. From 80-196 meters, zones of contrasting high/low resistivity indicate vertical venting structures along fractures (dashed lines) from ascending moisture at depth. Outcrop of gypsum bedrock observed at the surface in the on this survey.

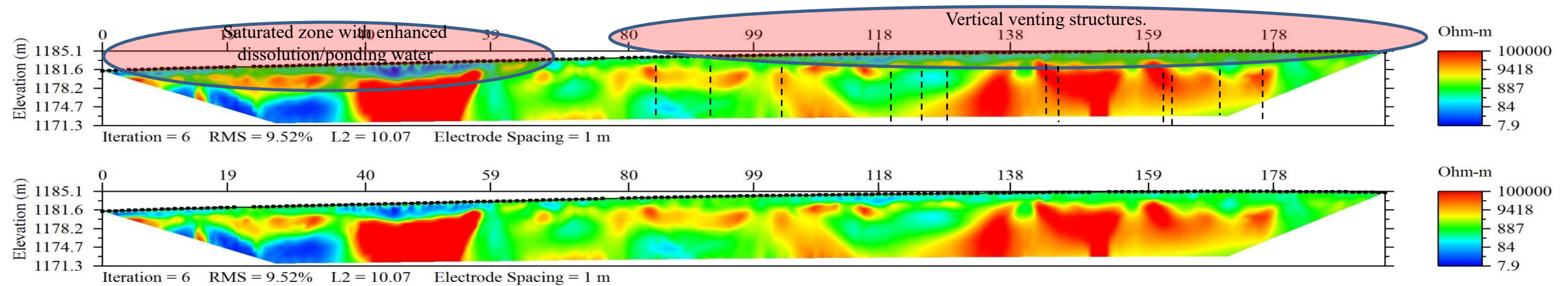
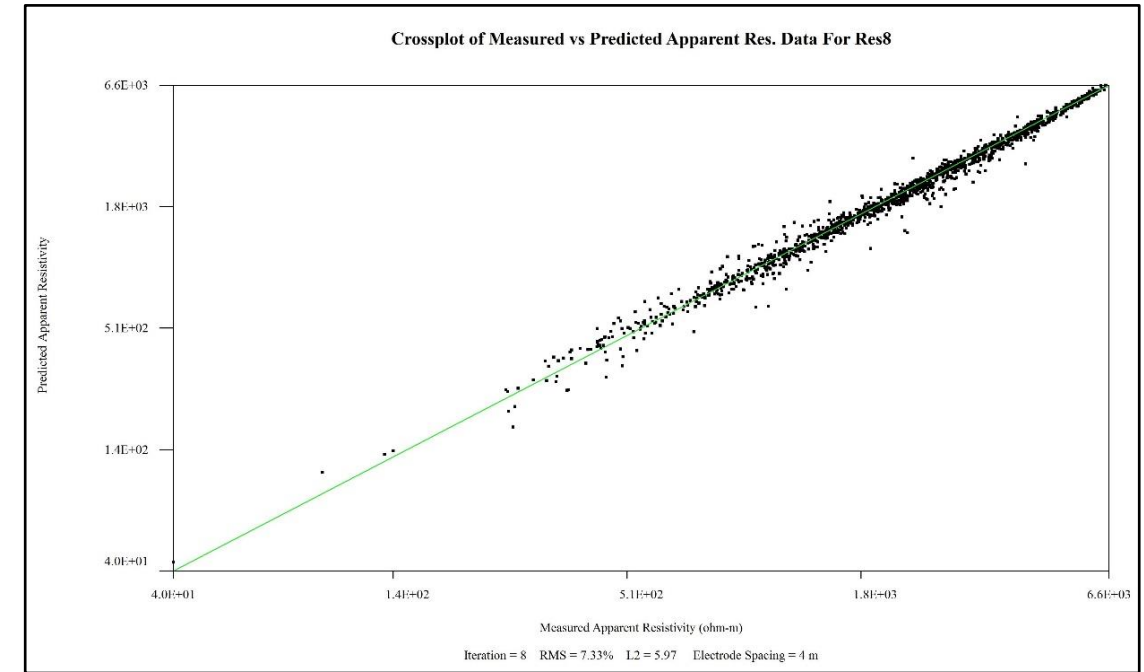


Figure C4: Survey site Res8_P23. 56 electrode dipole-dipole array roll-along survey with 1-meter spacing (total length 196 meters). Note that maximum resistivity reading in inverted sections is 100k ohm-m. RMS error 9.52%.



Description:

This survey highlights similar features to the roll-along survey of site Res8_P23, however depth penetration is greater given the electrode spacing of 4 meters. Resolution near the surface is decreased, yet the saturated subsurface from 0-50 meters can still be interpreted by the zone of low resistivity at 2 meters depth. From 72-224 meters vertical venting structures along fractures are better expressed at depth.

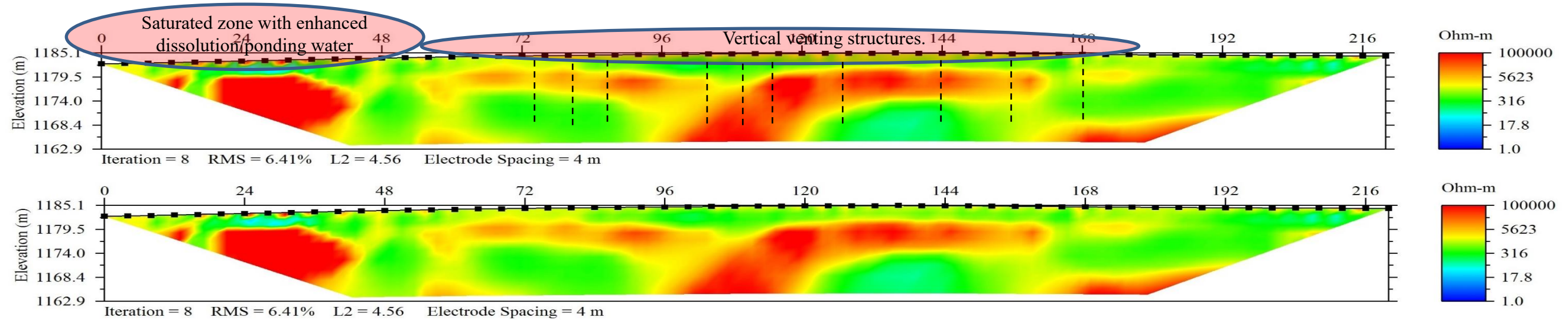
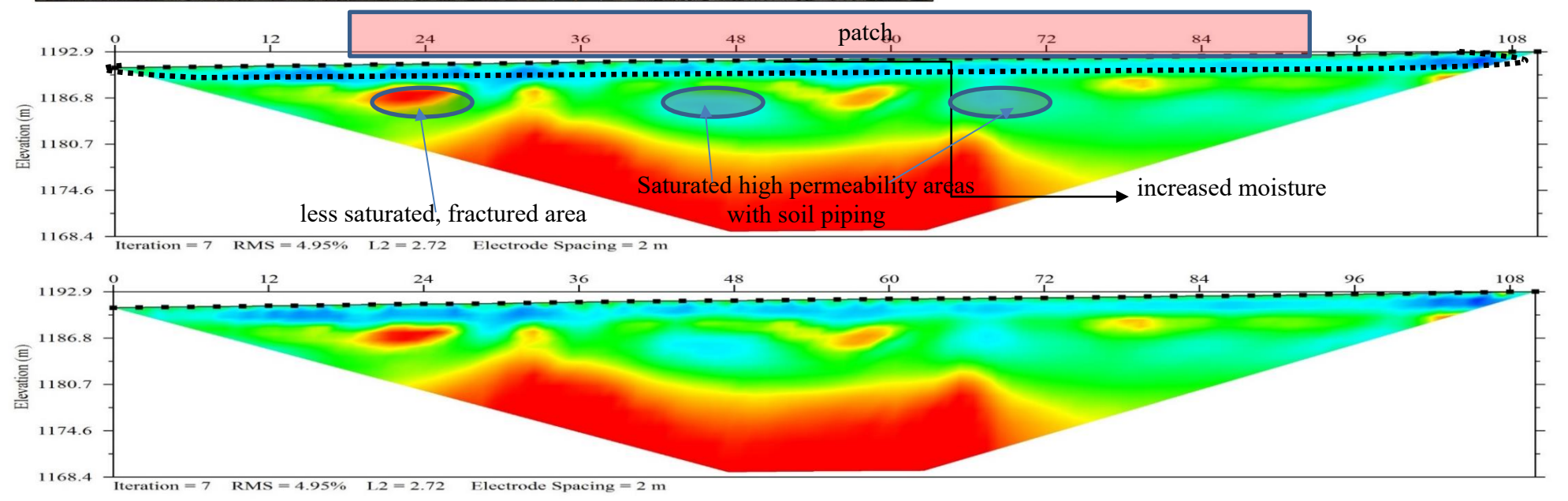
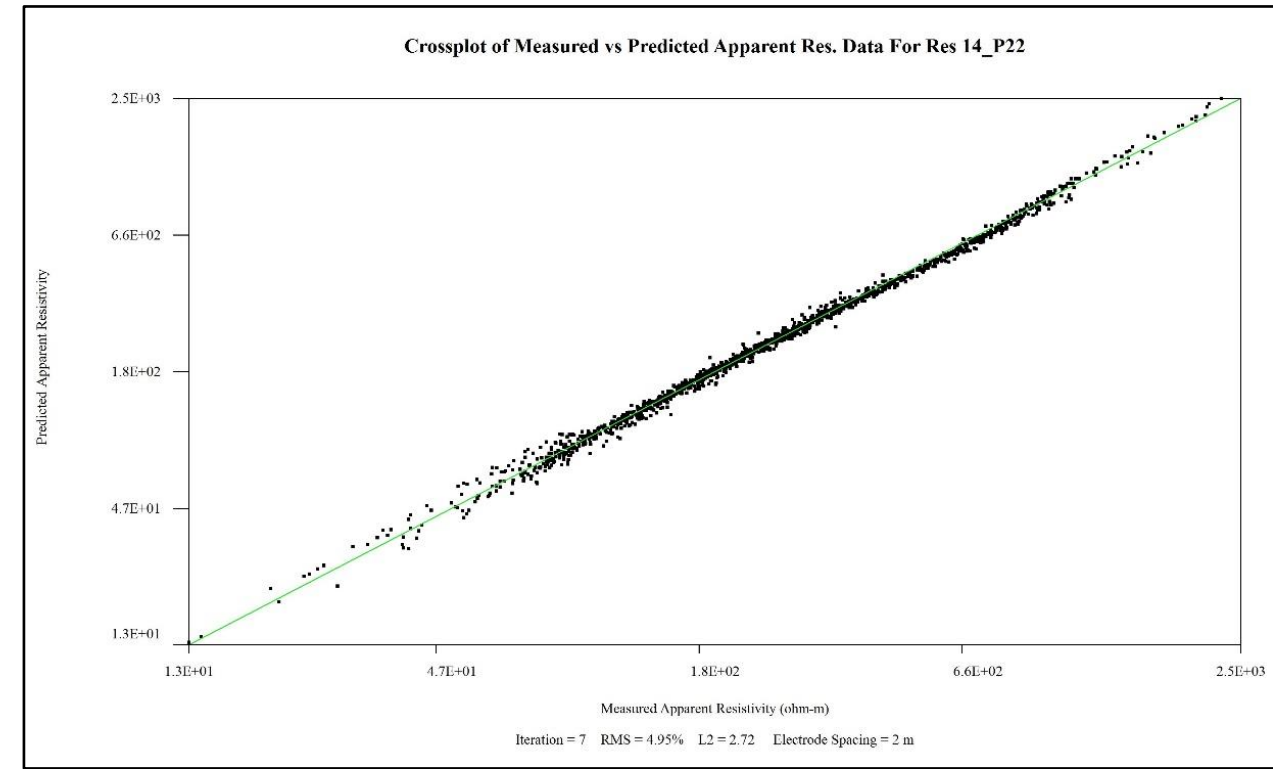


Figure C5: Survey site Res8_P23. 56 electrode dipole-dipole array with 4-meter spacing (total length 224 meters). Note that maximum resistivity reading in inverted sections is 100k ohm-m. RMS error 6.41%

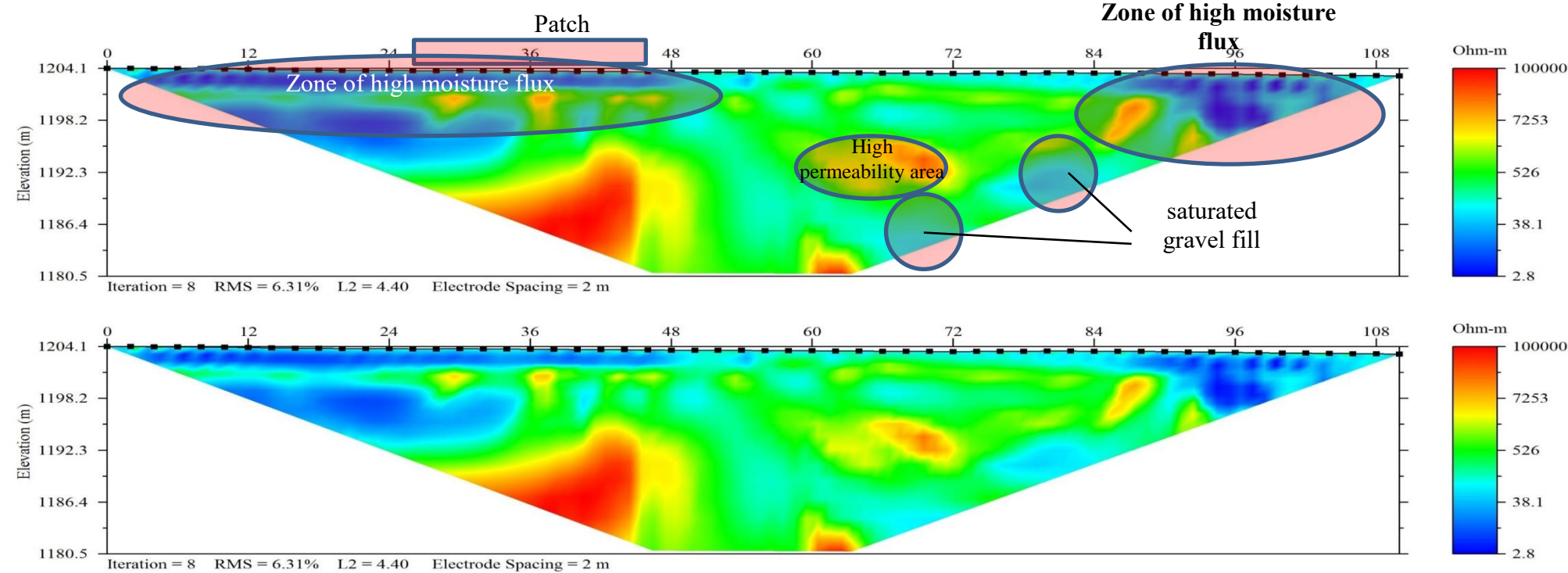
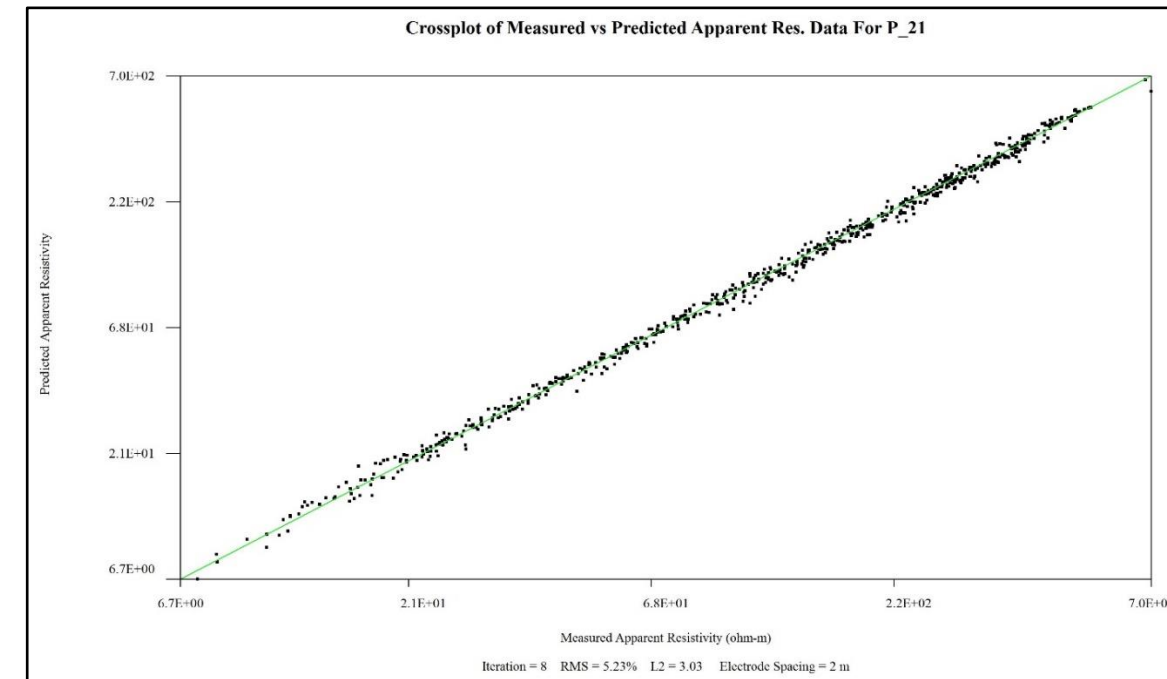


Description:

Survey is located in an area with predominantly gypsic soil on the surface. Patch increased lateral piping at 1-2 meters of depth as indicated by a continuous zone of low resistivity (dotted line). Soil piping is indicated by zones of low resistivity at depths of 6-9 meters.

Soil piping is likely associated with variations in underlying gypsum, possibly fractured zones or solutional conduits at depth. Berms constructed at northern and southern ends of survey have likely increased piping potential locally.

Figure C6: Survey site Res14_P22. 56 electrode dipole-dipole array with 2-meter spacing (total length 112 meters). Note that maximum resistivity reading in inverted sections is 100k ohm-m. RMS error 4.95%



Description:

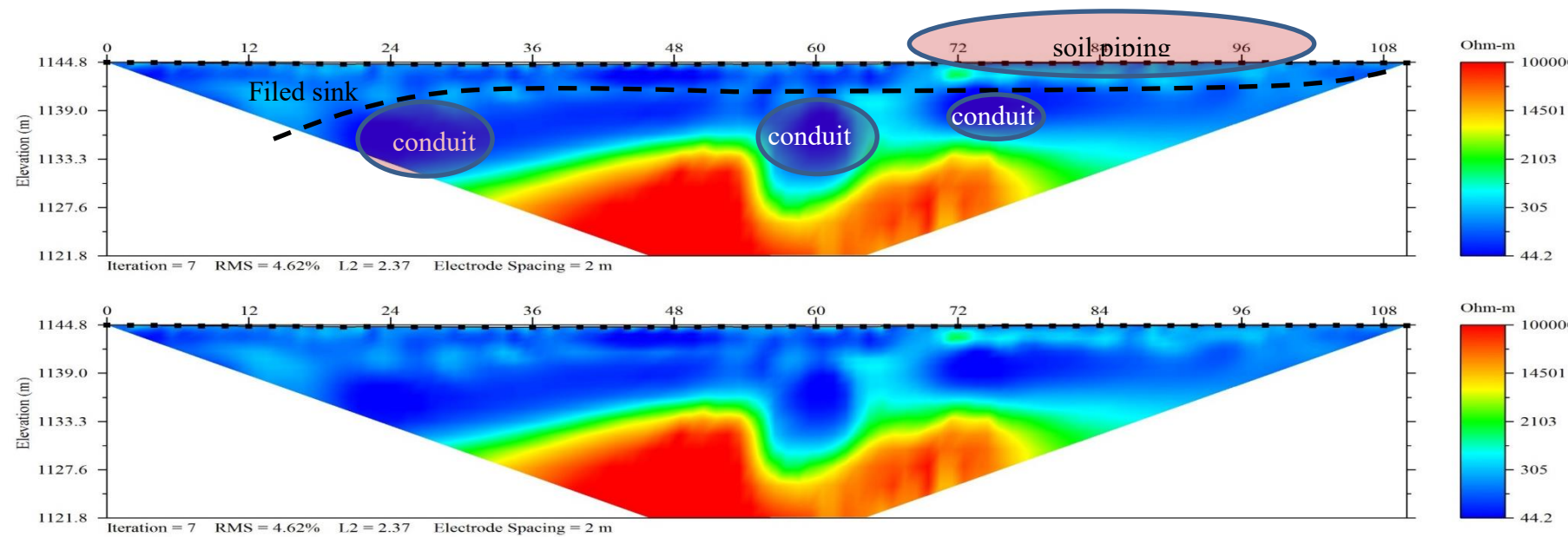
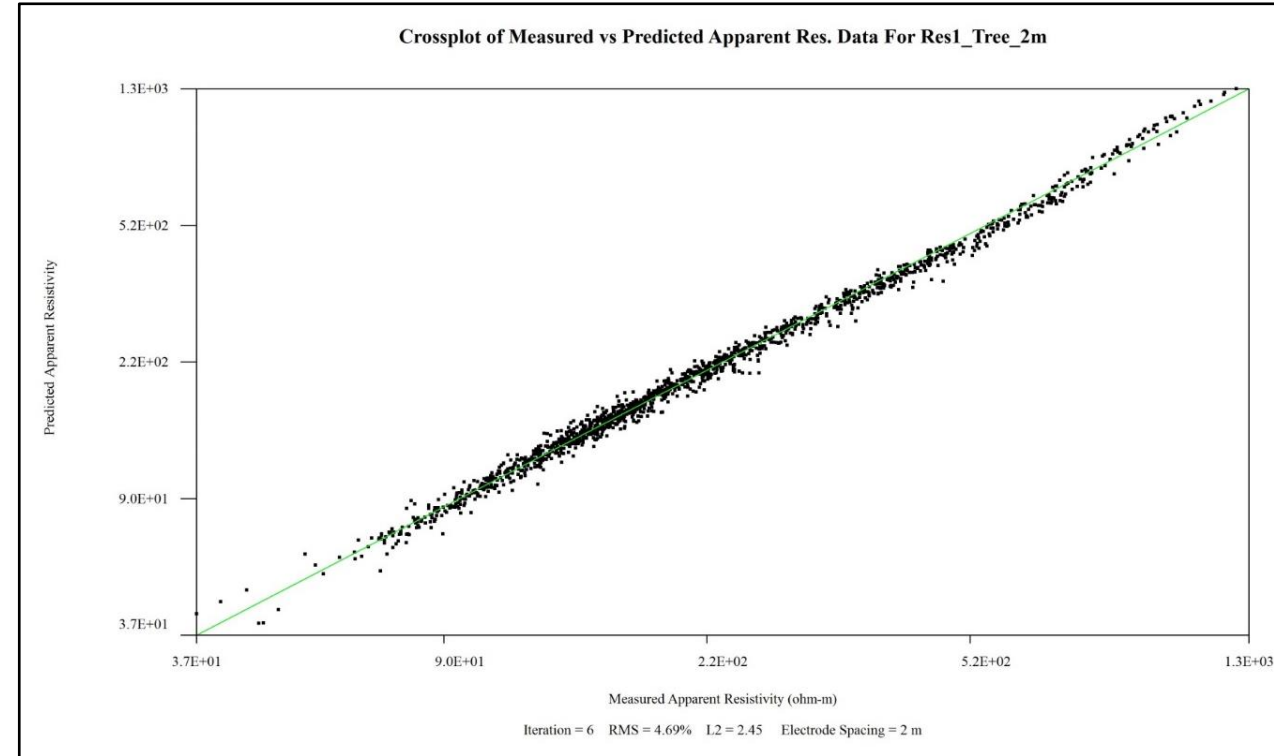
Survey conducted in a filled solution valley. Regions of high moisture flux or areas of preferential moisture flow are indicated by the low resistivity. Berm emplacement north and south of survey (not on map) are likely responsible for increased water flux beneath the road.

High and low permeability zones at depth likely represent gravel fill regions with low fine fraction content.

Resistivity variations associated with variations in moisture content in channel fill.

Increased piping in region associated with variations in moisture flux likely due to berm emplacement and differential permeability of road compositions.

Figure C7: Survey site P21. 56 electrode dipole-dipole array with 2-meter spacing (total length 112 meters). Note that maximum resistivity reading in inverted sections is 100k ohm-m. RMS error 6.31%



Description:

Surface expressions of karst such as caves and collapse features have been observed and documented 20-30 meters north of this survey. Overgrowth of vegetation on the surface is localized near the center of the survey (50-60 meters). At depth, zones of lower resistivity or high conductivity correlate well with surficial expressions of vegetation and soil piping into conduits. The zones of higher resistivity or low conductivity at around 20 meters depth indicate voids/conduits. Dashed line indicates approximate bedrock boundary with upper bedrock regions saturated.

Filled sink from (0-30 meters) is highlighted by a continuous zone of low resistivity. Contrasting low/high resistivity from 72-96 meters is attributed to soil piping near the surface.

Figure C8: Survey site Res1_Tree. 56 electrode dipole-dipole array with 2-meter spacing (total length 112 meters). Note that maximum resistivity reading in inverted sections is 100k ohm-m. RMS error 4.62%



Description:

224-meter survey at site Res1_Tree. Similar features are expressed in this survey as the 112-meter survey of the same site. Approximate location of the thick surficial vegetation is between 90-130 meters. Soil piping is common from 120-224 meters.

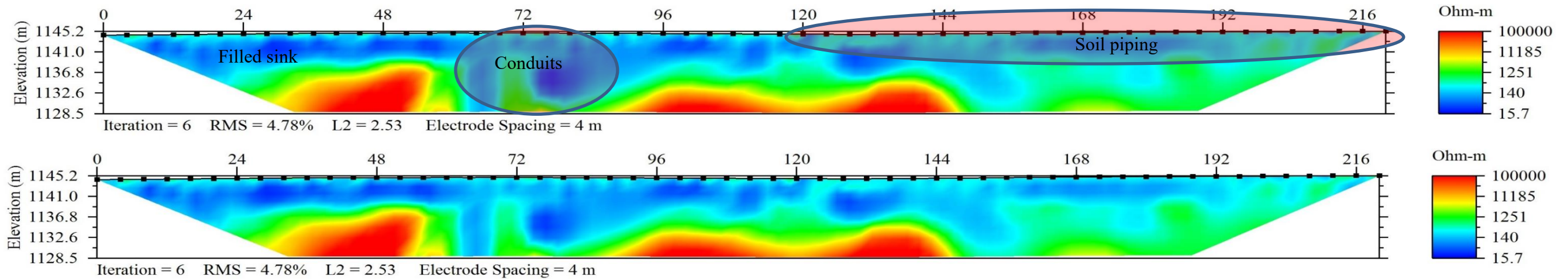
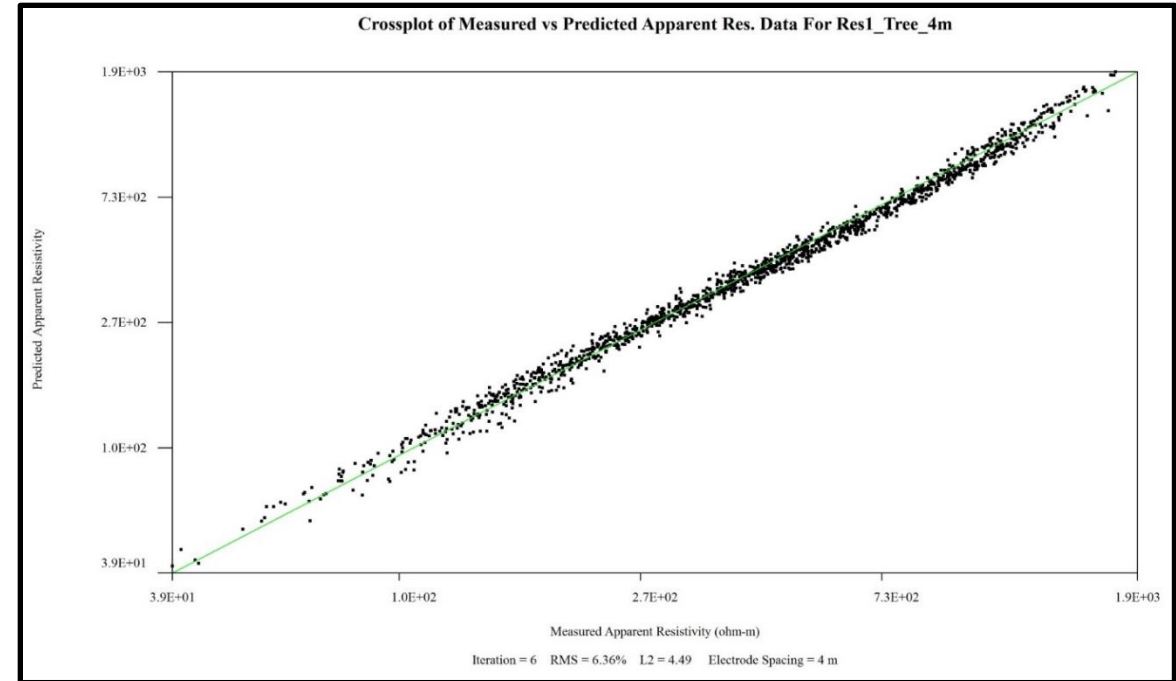
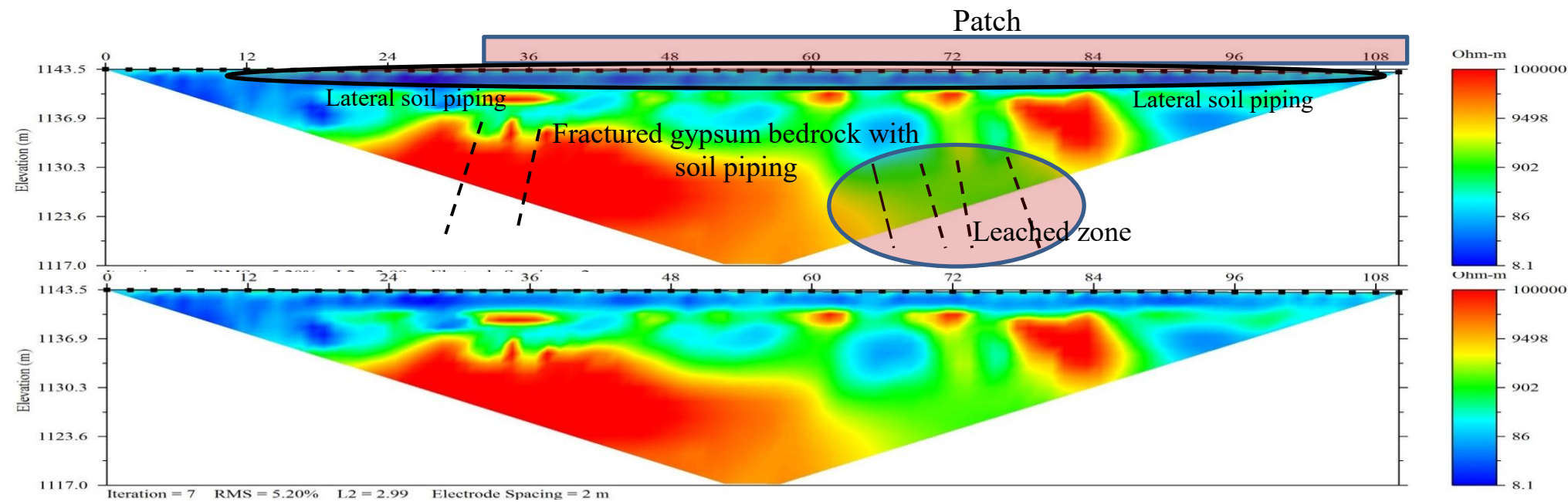
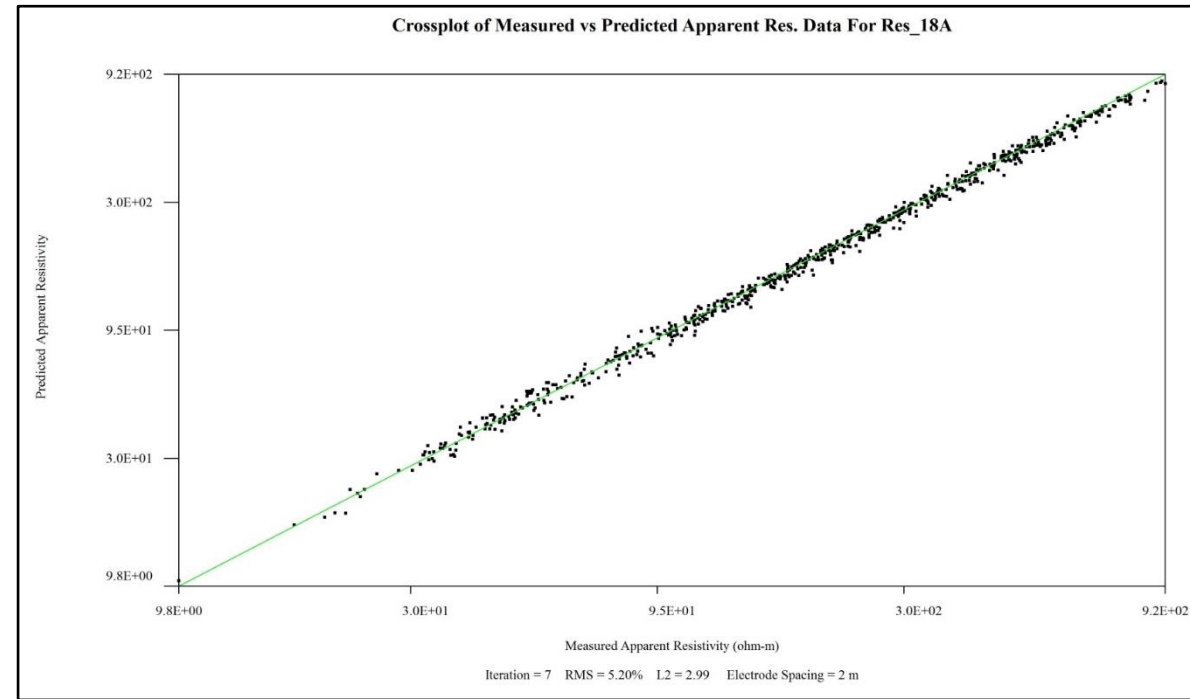


Figure C9: Survey site Res1_Tree. 56 electrode dipole-dipole array with 4-meter spacing (total length 224 meters). Note that maximum resistivity reading in inverted sections is 100k ohm-m. RMS error 4.78%



Description:

Patch in the road is from meter 34-110. Several solutional linear cracks were observed on the surface 2-3 meters southwest of the survey line. These features are dispersed on the surface for the first 15 meters. The region of low resistivity or high conductivity at 2-4 meters of depth is attributed to lateral soil piping. Solutional fractures create preferential flow paths for meteoric waters leading to piping of fine soils underneath the road base.

At greater depths (4-26 meters), regions of contrasting high and low resistivity are attributed to highly fractured gypsum bedrock (dashed lines) where moisture flux is greatest.

Figure C10: Survey site Res18_P17. 56 electrode dipole-dipole array with 2-meter spacing (total length 112 meters). Note that maximum resistivity reading in inverted sections is 100k ohm-m. RMS error 5.20%



Description:

Roll-along survey at 1-meter spacing provides enhanced resolution of the shallow subsurface in this area. From 22-50 meters is a zone of solution conduits connected to surface, correlation was made with excavation. At depth, there are several zones of high permeability that are either saturated or dry, these are highlighted by the sudden rather than gradual changes in resistivity. These are solutional conduits.

From meter 80-112 is an area of lower elevation where ponding and increased dissolution occurs during meteoric events.

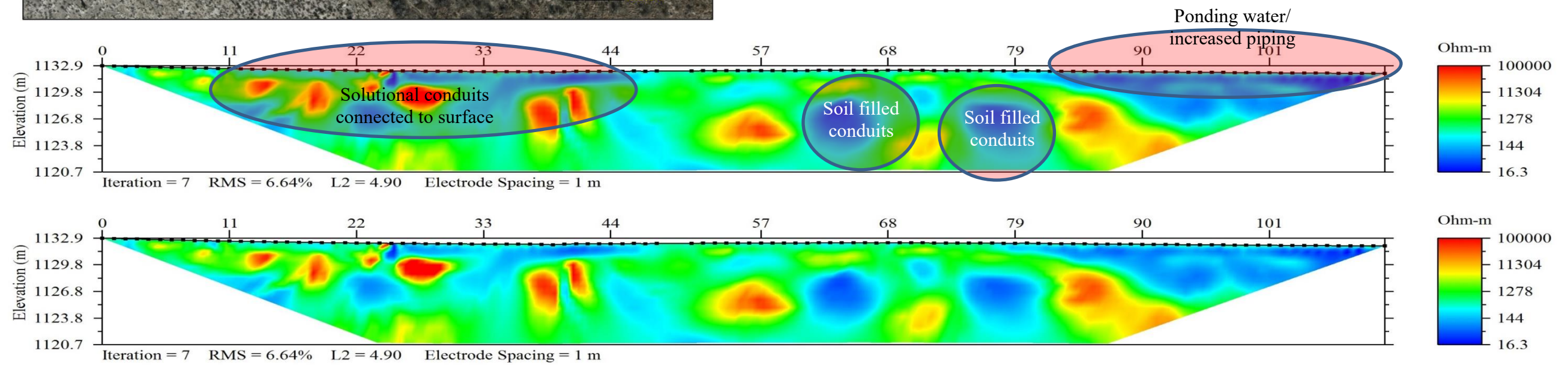
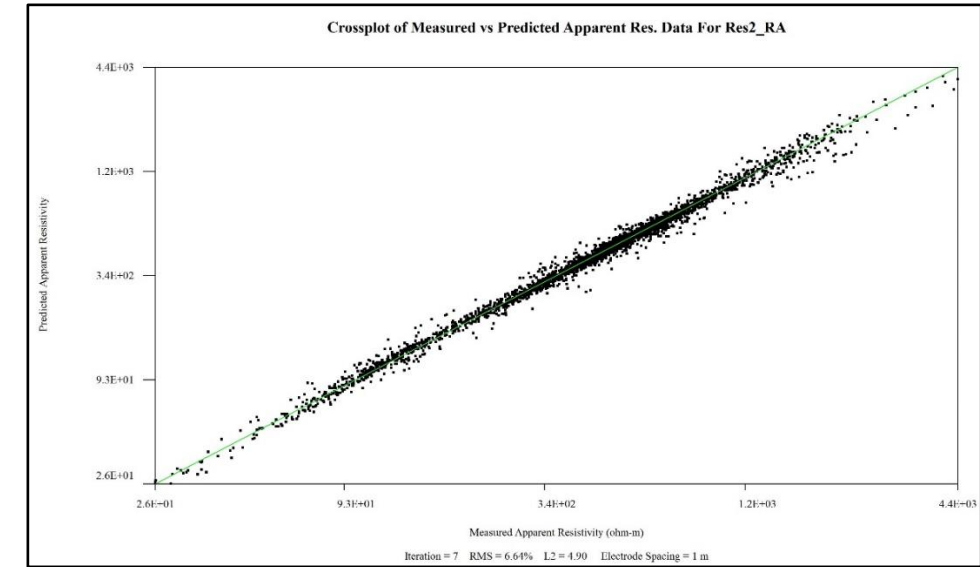
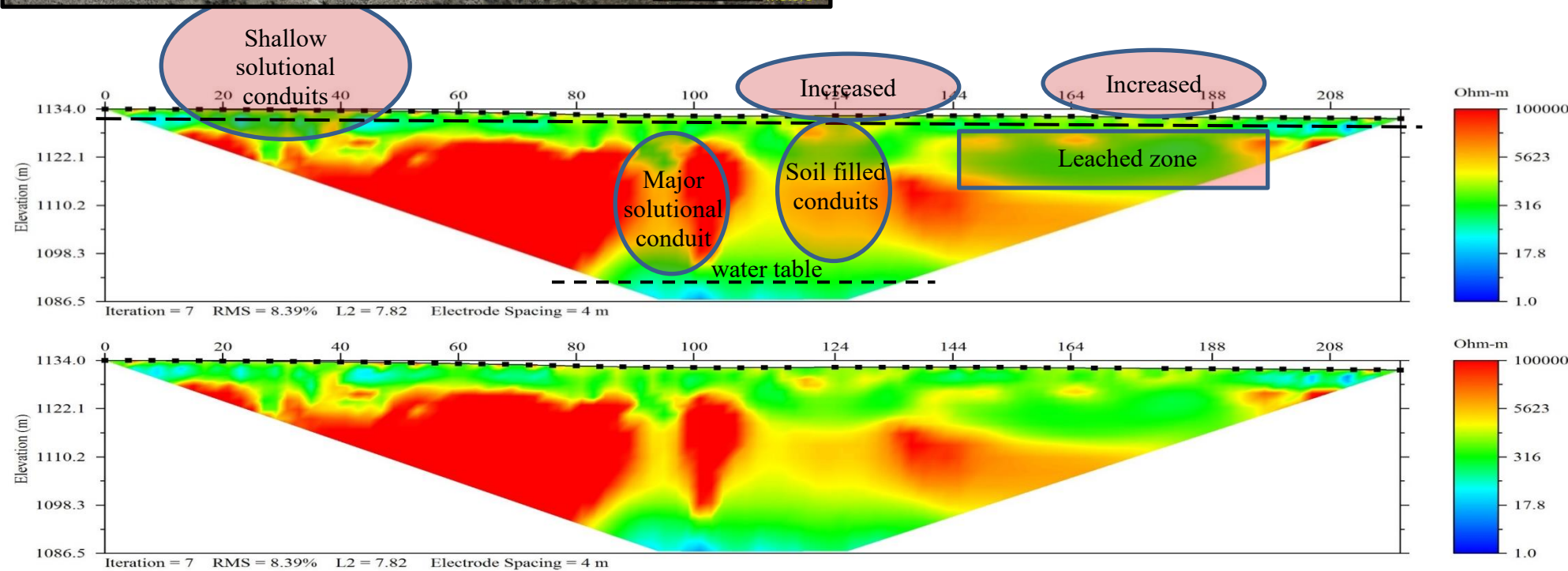
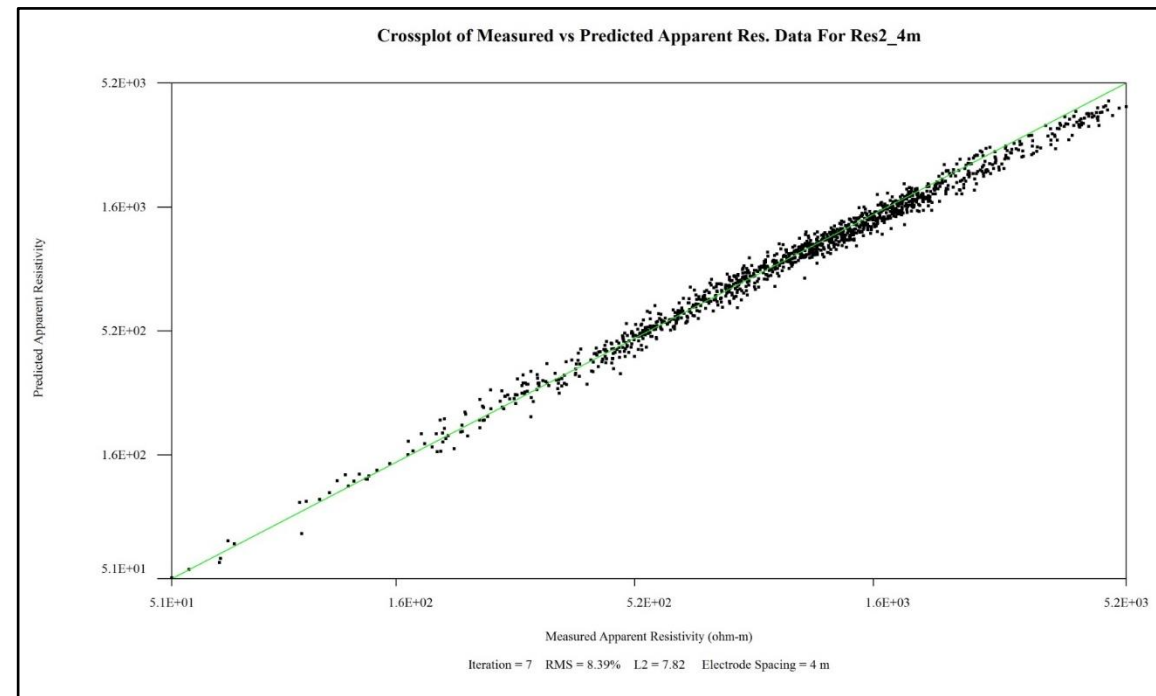


Figure C11: Survey site Res2. 56 electrode dipole-dipole array roll-along survey with 1-meter spacing (total length 112 meters). Note that maximum resistivity reading in inverted sections is 100k ohm-m. RMS error 6.64%.

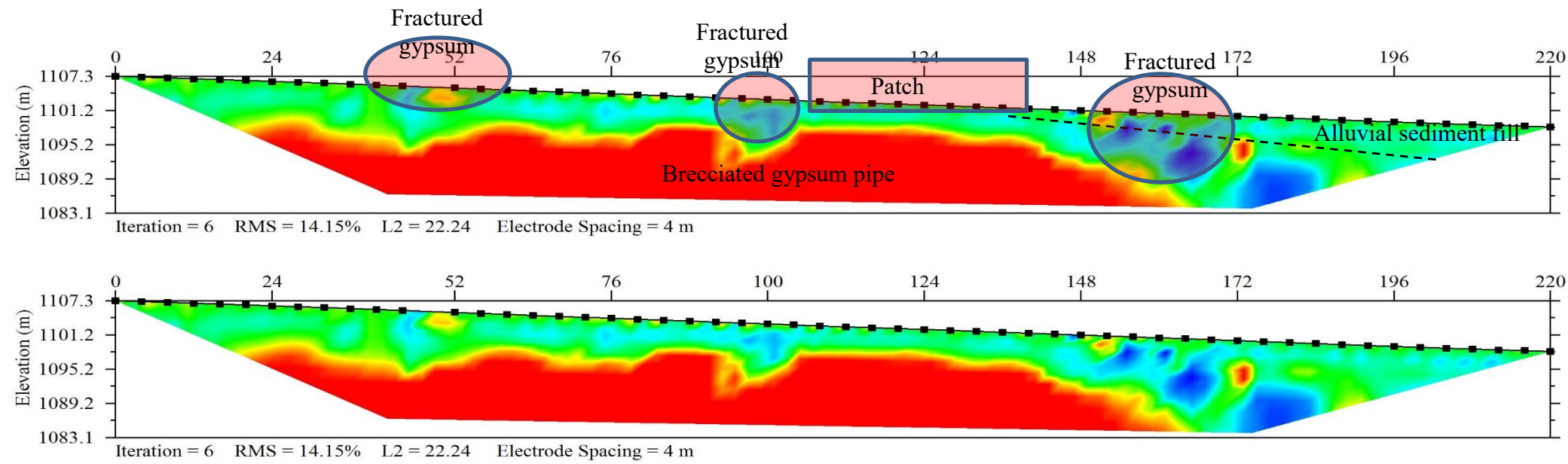
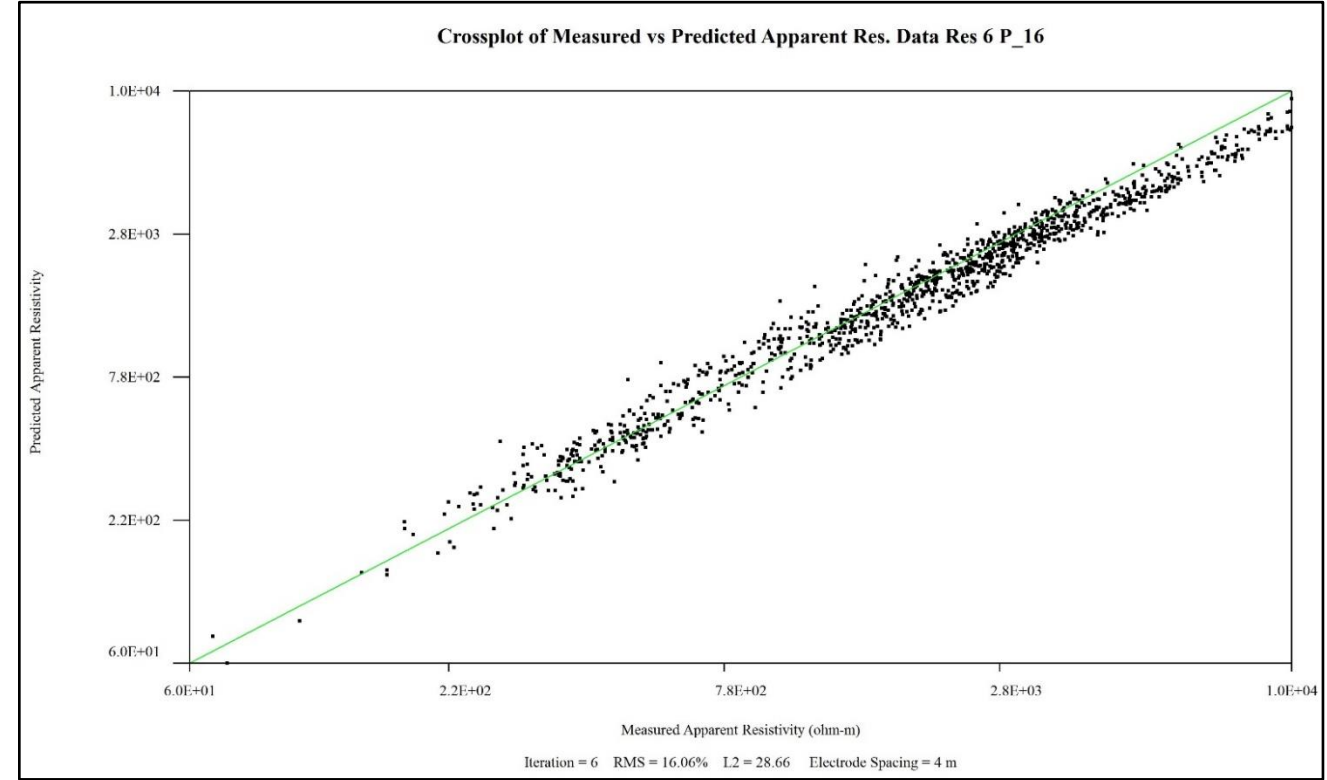


Description:

Excavation between 88 and 100 meters showed solutional conduits. Preferential dissolution resulted in the formation of conduits which were later filled with soil as a result of piping. Zones of higher resistivity in these regions are less saturated at depth and more porous.

Depth to gypsum bedrock begins at 1-2 meters (dashed line). Leached zones within the bedrock are displayed as regions with contrasting high/low resistivity. Extremely low resistivity at depth is likely the water table.

Figure C12: Survey site Res2. 56 electrode dipole-dipole array with 4-meter spacing (total length 224 meters). Note that maximum resistivity reading in inverted sections is 100k ohm-m. RMS error 8.39%



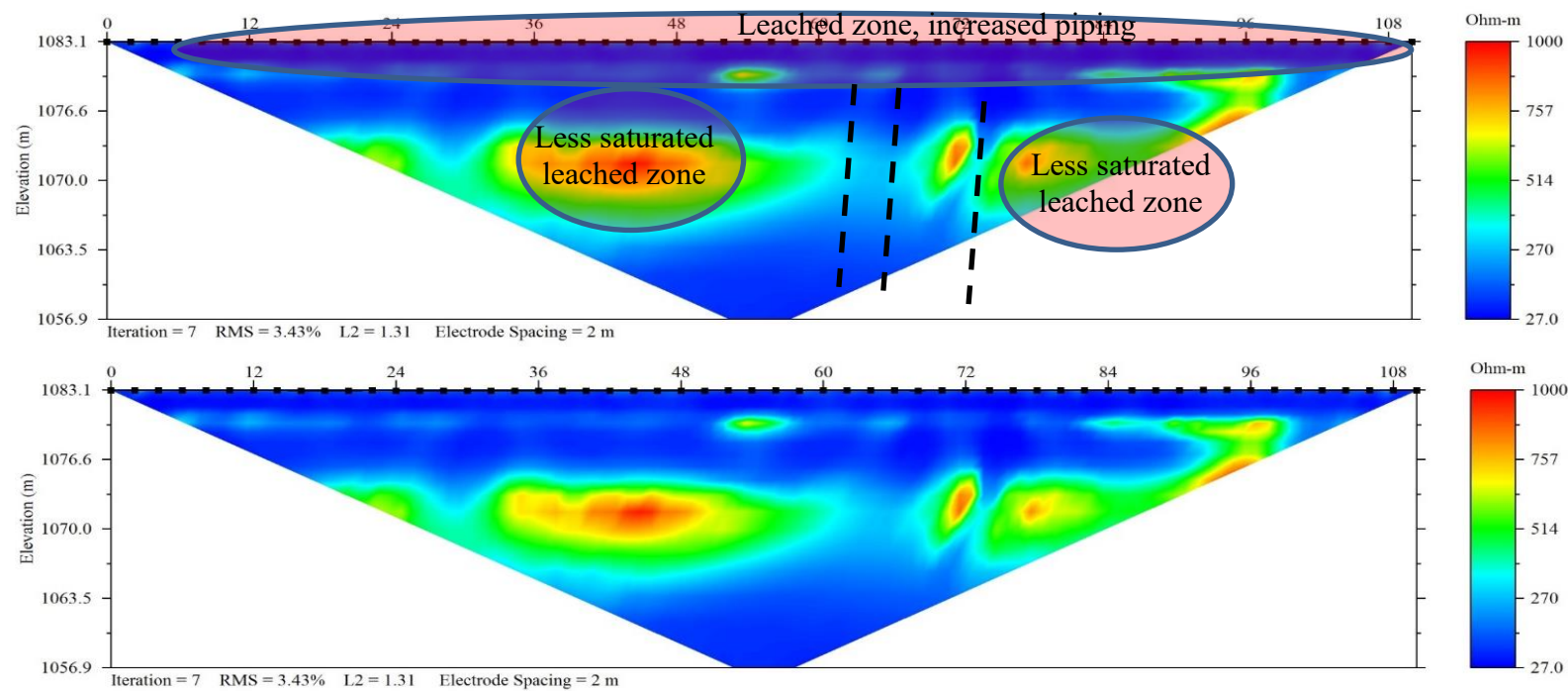
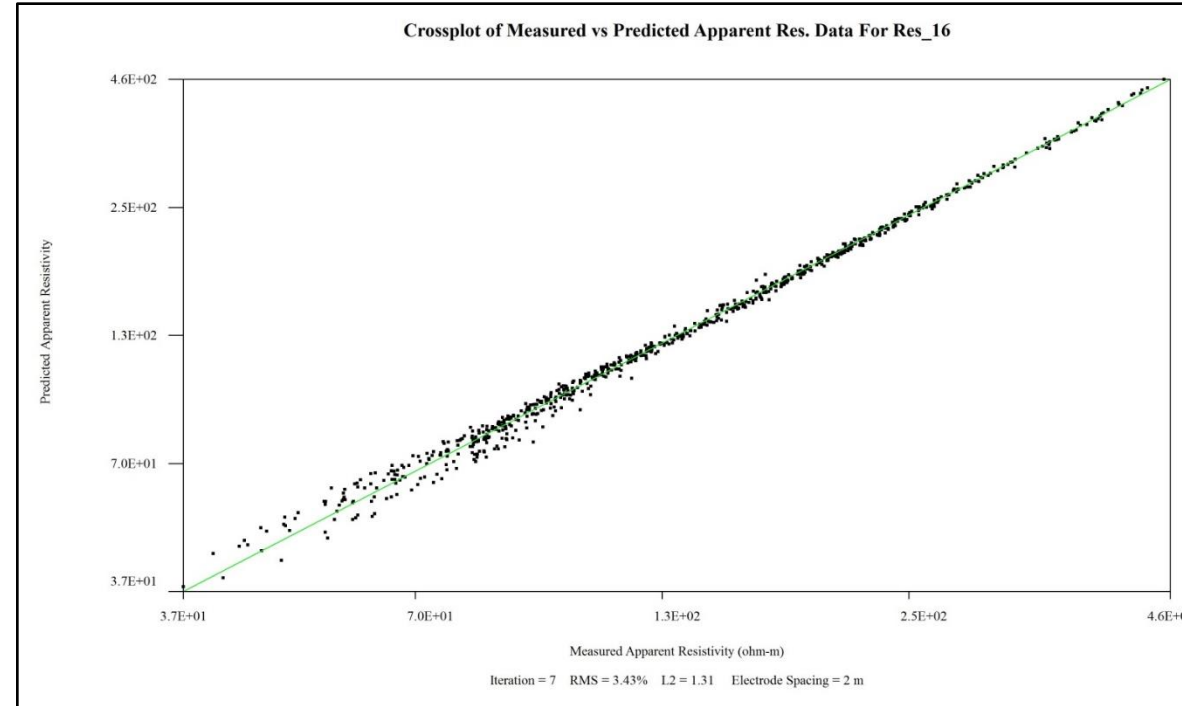
Description:

High permeability zones/fractured gypsum are circled. These are areas experience high moisture flux and alluvial sediment infill. Given the slope of the terrain these zones become saturated during heavy rainfall. High permeability zones are associated with uncemented regions on margin of large breccia pipe (fractured gypsum).

Ohm-m

100000
10946
1198
131
14.4

Figure C13: Survey site Res6_P16. 56 electrode dipole-dipole array with 4-meter spacing (total length 224 meters). Note that maximum resistivity reading in inverted sections is 100k ohm-m. RMS error 14.15%

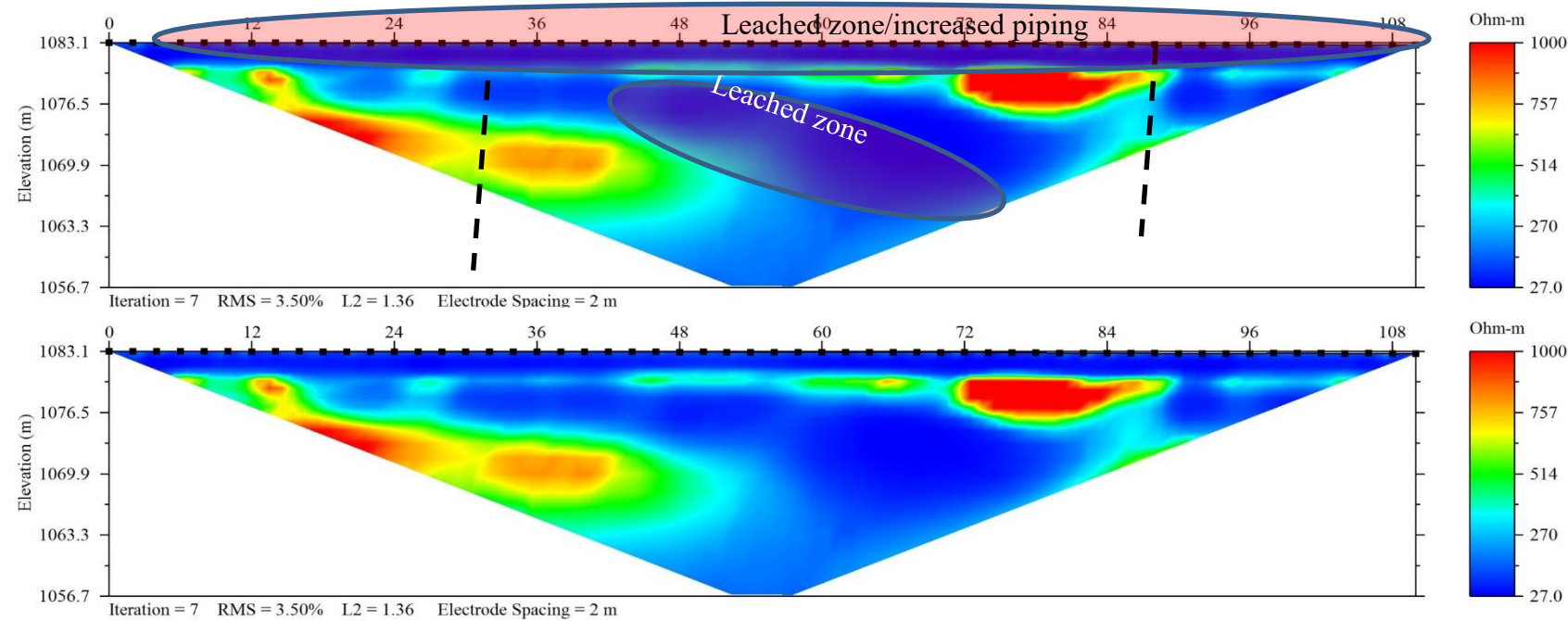
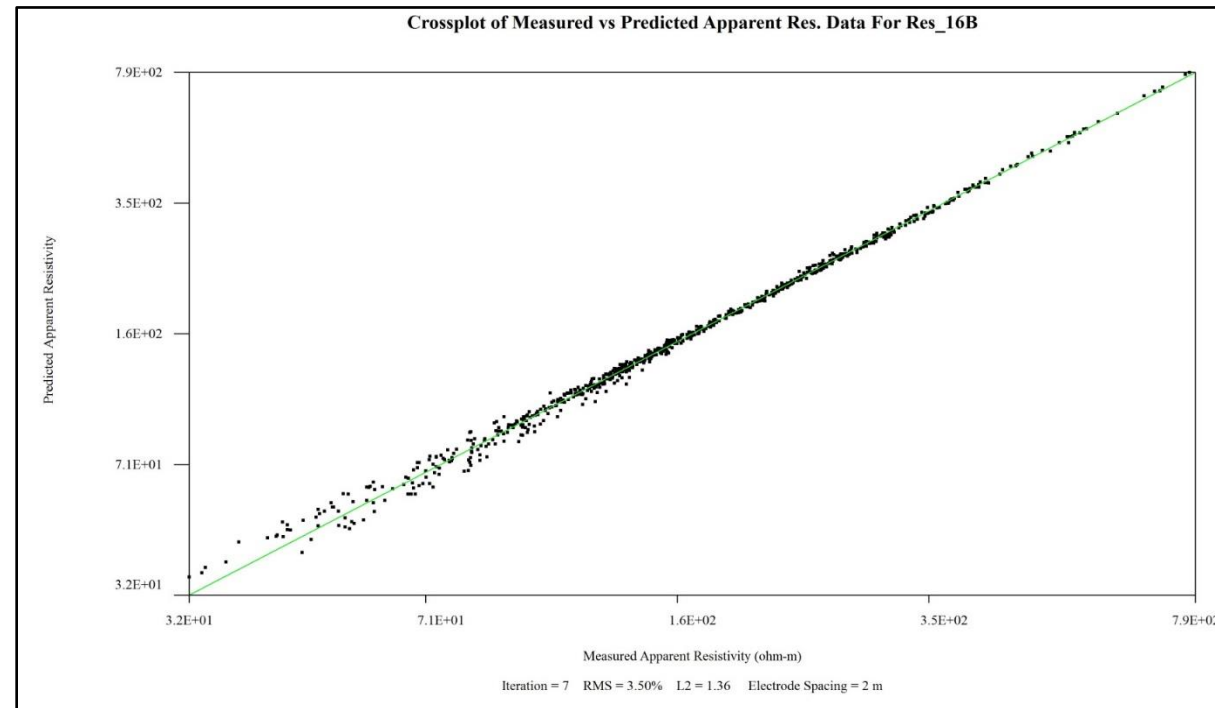


Description:

First half of 224-meter survey at site Res16_P13. Resistivity values in this area are relatively lower than other sites in this study. These low values indicate heavily leached, highly fractured gypsum that is saturated with water. High hydraulic gradient to the southwest where deeply incised arroyo occurs. Major fractures (dashed lines) provide vertical cross communication of fluids.

Site is in a low topographic gradient region and likely exhibits extended periods of ponding after major rain events. Due to ponding highly fractured bedrock is solutionally widened both along fractures and gypsum laminae. As a result, subsidence is common due to differential compaction of these leached horizons.

Figure C14: Survey site Res16_P13. 56 electrode dipole-dipole array with 2-meter spacing (total length 112 meters). Note that maximum resistivity reading in inverted sections is 1000 ohm-m. RMS error 3.43%

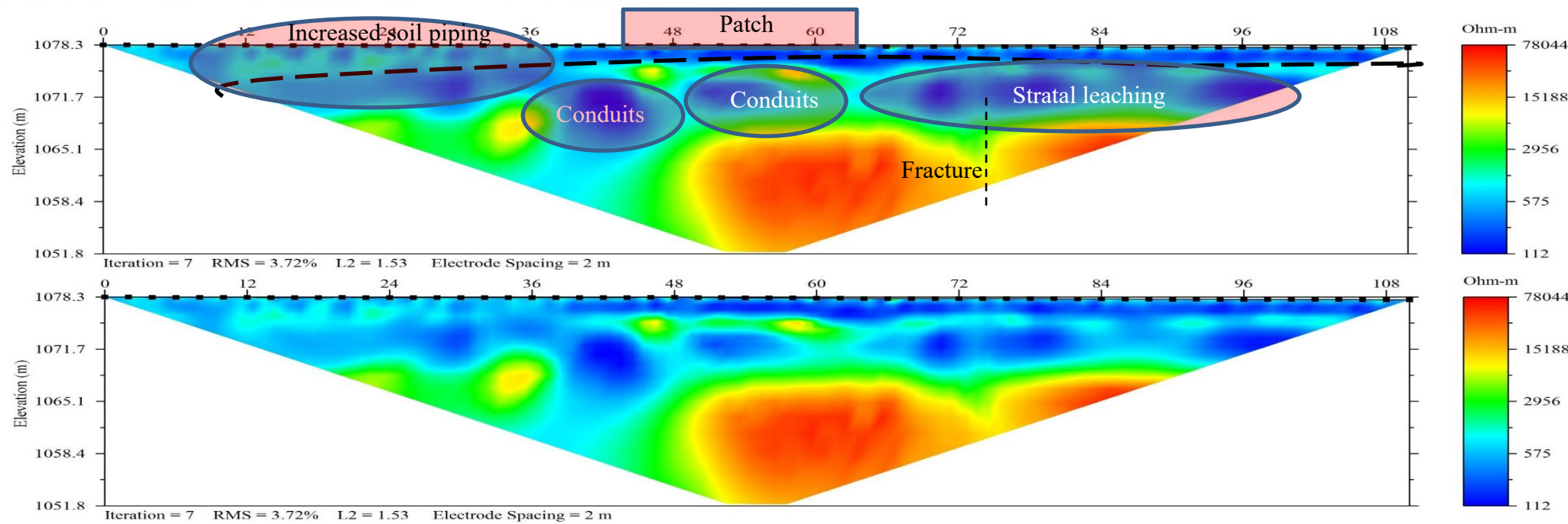
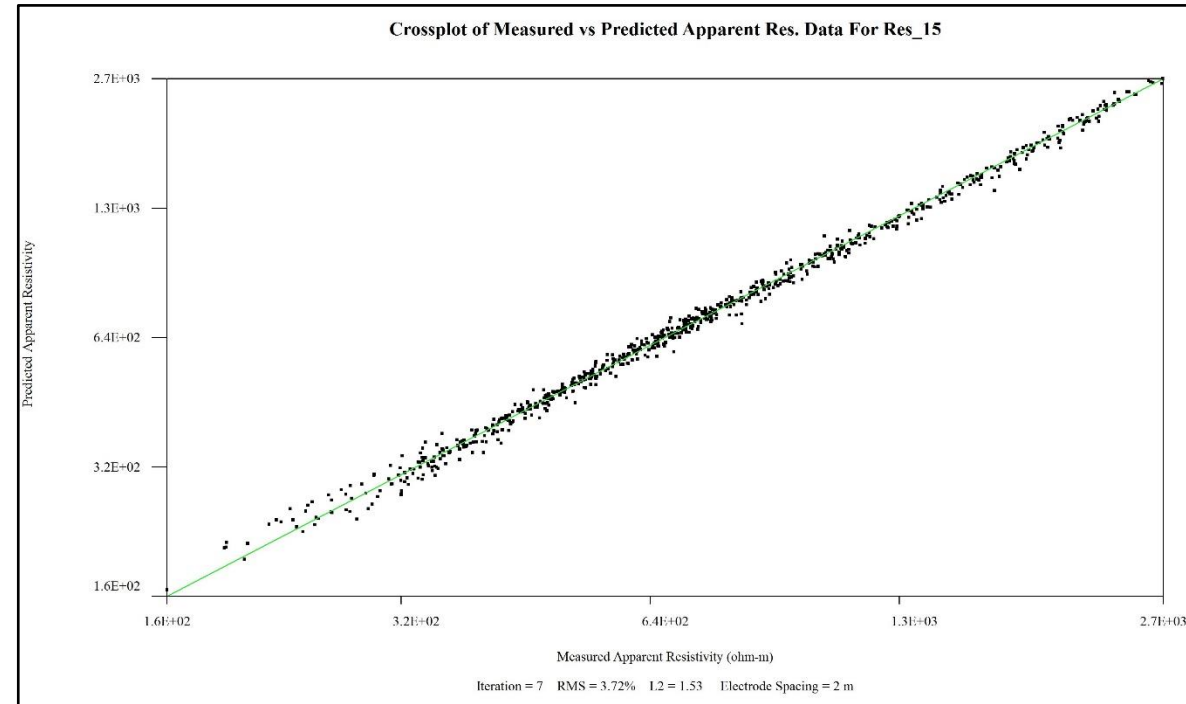


Description:

Second half of 224-meter survey at site Res16_P13 with 50% overlap. Resistivity values in this area are relatively lower than other sites in this study. These low values indicate heavily leached, highly fractured gypsum that is saturated with water. High hydraulic gradient to the southwest where deeply incised arroyo occurs promotes lateral migration of fluids. Major fractures (dashed lines) provide vertical cross communication of fluids.

High resistivity regions indicate poorly fractured regions. Large low resistivity region extending from top to bottom indicates highly leached vertical region of connectivity. Sloping low resistivity pattern to the southeast is likely associated with dominant groundwater flow direction.

Figure C15: Survey site Res16_P13. 56 electrode dipole-dipole array with 2-meter spacing (total length 112 meters). Note that maximum resistivity reading in inverted sections is 1000 ohm-m. RMS error 3.50%

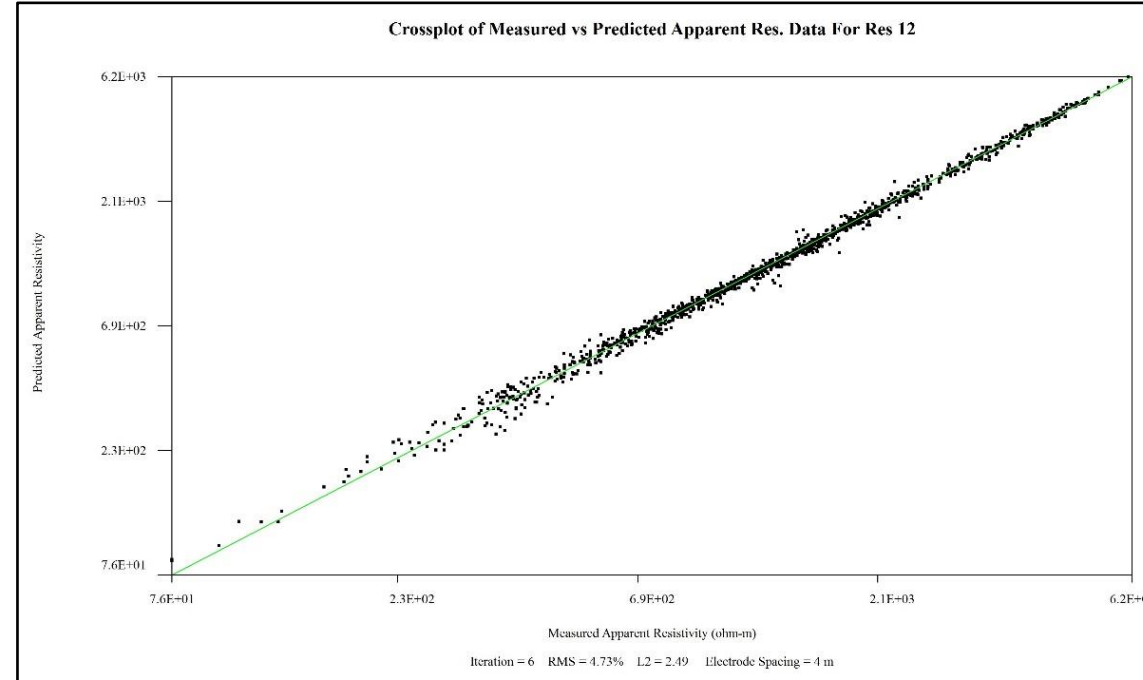


Description:

Shallow solutional conduits filled with soil that are located on edge of gypsic ridge. Thicker gypsic soil occurs to the northwest where increased soil piping is common. Solutional conduit development appears to be associated with fractures (thin dashed lines) and preferential lateral zone of dissolution.

Road subsidence likely more common at edge of ridge where thin soils are more readily transported into solution conduits. Variable moisture content in upper regions of bedrock exhibit lower resistivity values likely associated with stratal leaching (thick dashed line indicates approximate boundary between soil and rock).

Figure C16: Survey site Res15_P11. 56 electrode dipole-dipole array with 2-meter spacing (total length 112 meters). Note that maximum resistivity reading in inverted sections is 78,044 ohm-m. RMS error 3.72%



Description:

At shallow depths, (1-2 meters) leached zone with variably saturated indurated gypsic soil and rock, which is more prominent beneath patch, indicating that patch may be enhancing preferential lateral piping.

At depth 4-6 meters, fractured (dashed vertical lines) gypsum is indicated by alternating high/low resistivity which promotes vertical moisture flux.

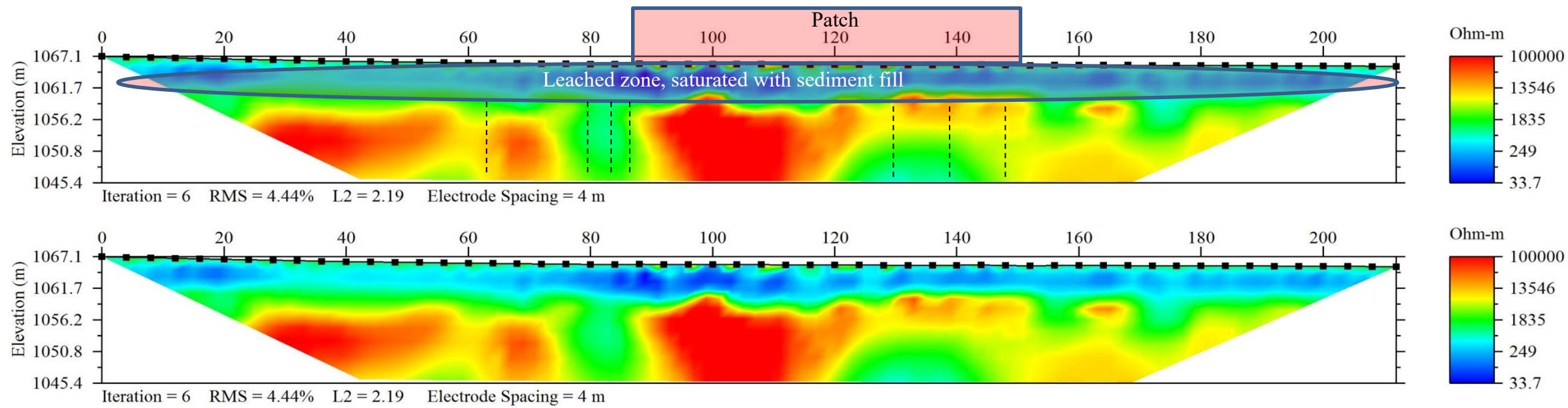
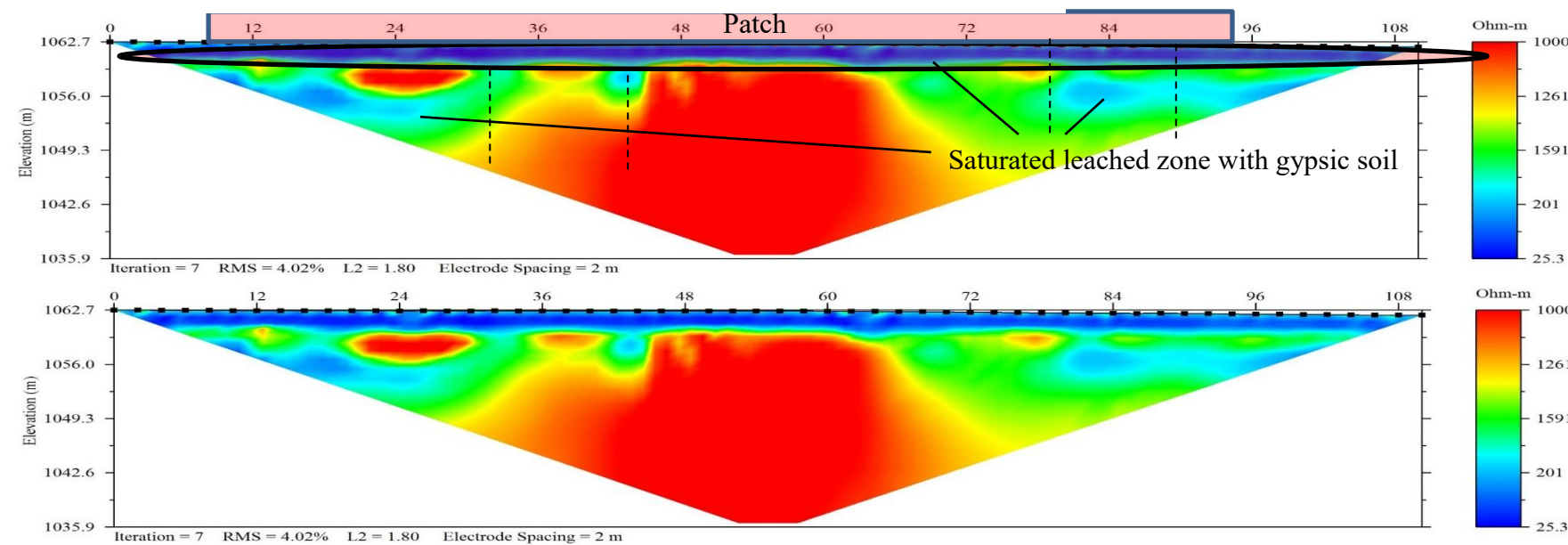
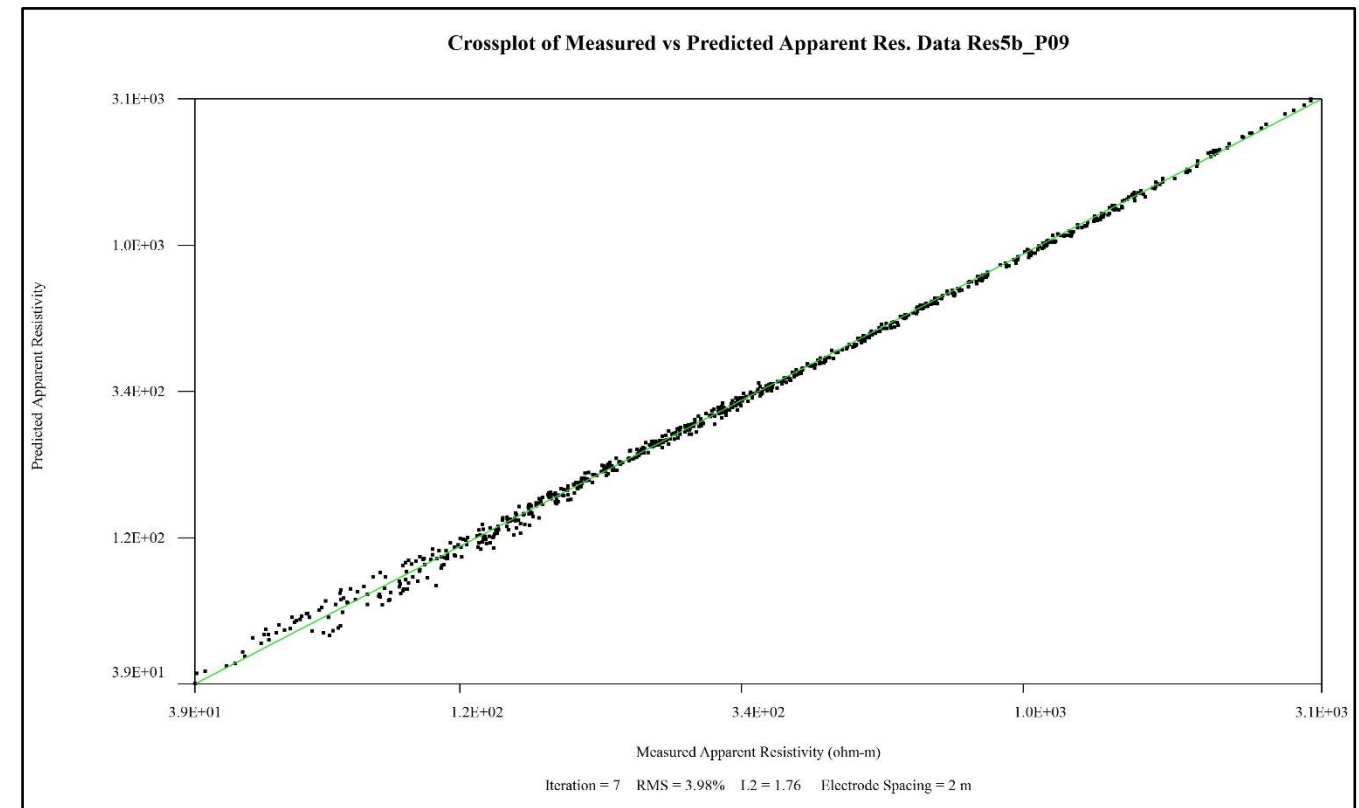


Figure C17: Survey site Res12_P10. 56 electrode dipole-dipole array with 4-meter spacing (total length 224 meters). Note that maximum resistivity reading in inverted sections is 100k ohm-m. RMS error 4.44%

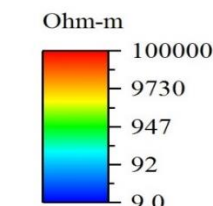
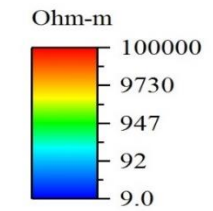
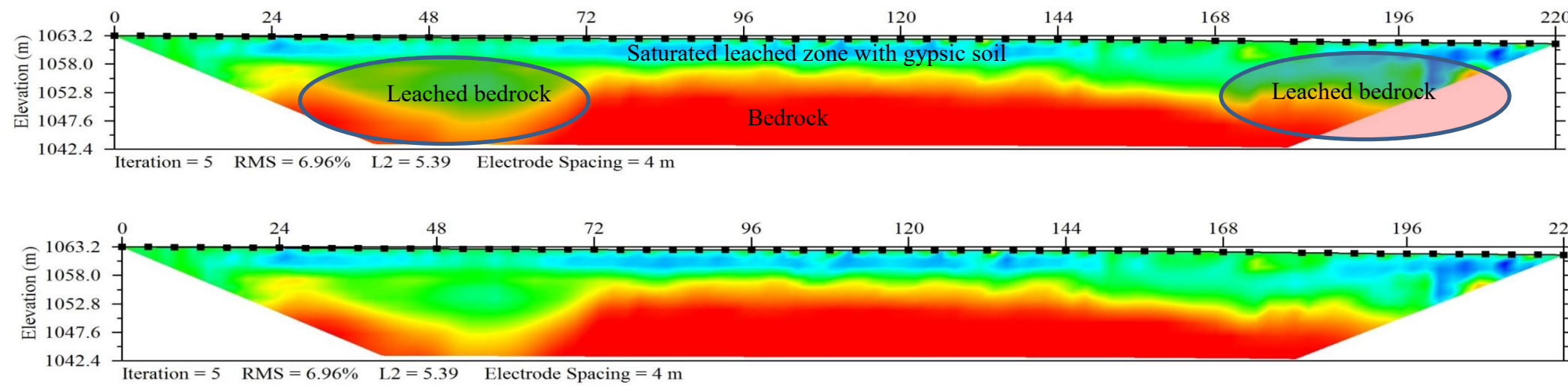
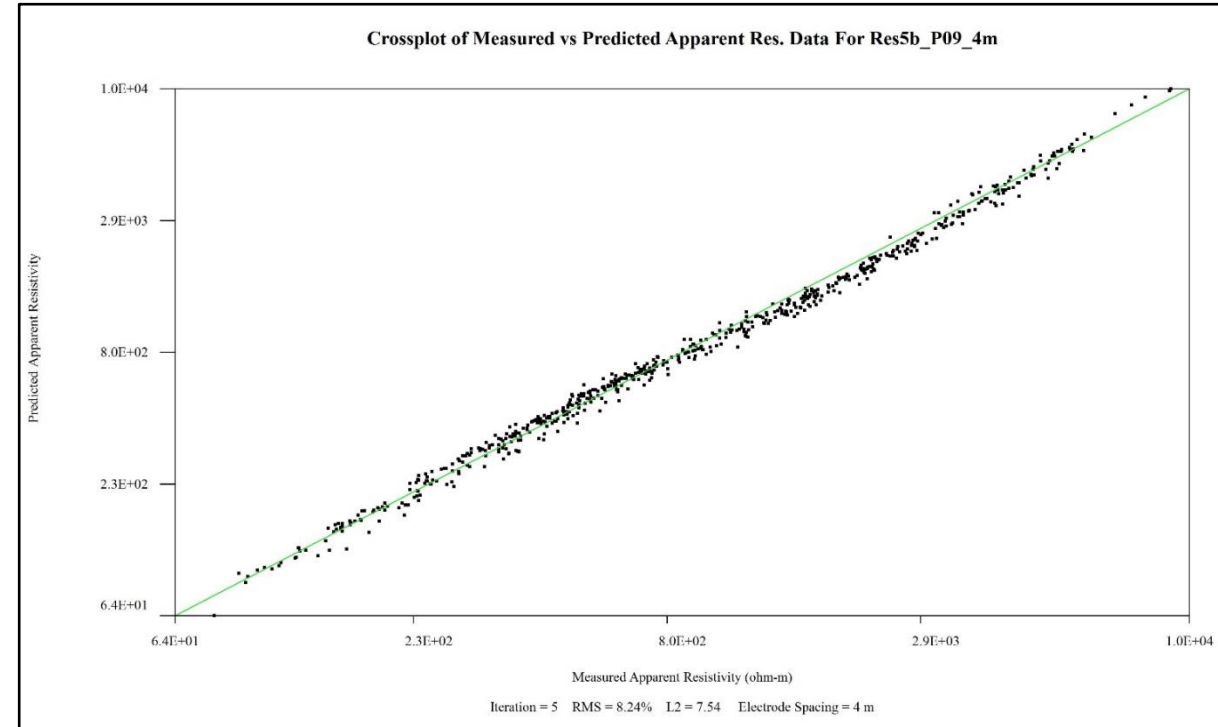


Description:

Leached gypsum at shallow depths highlighted by a continuous zone of low resistivity. Less saturated gypsum at depth indicated by moderately high resistivity. Highly resistive zones ($\geq 100k$ ohm-m) likely indicate competent/poorly fractured gypsum bedrock.

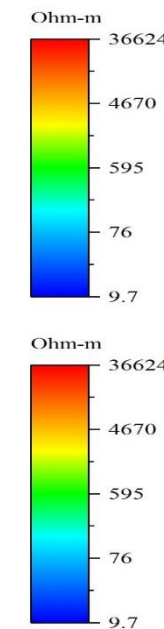
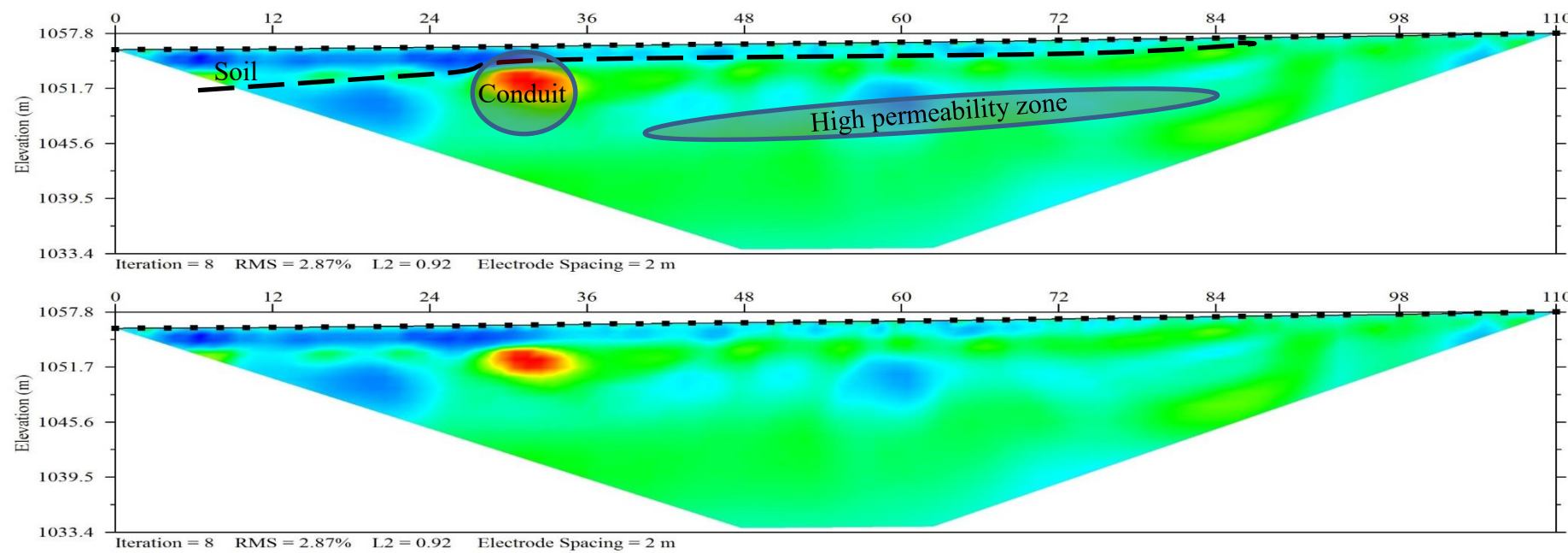
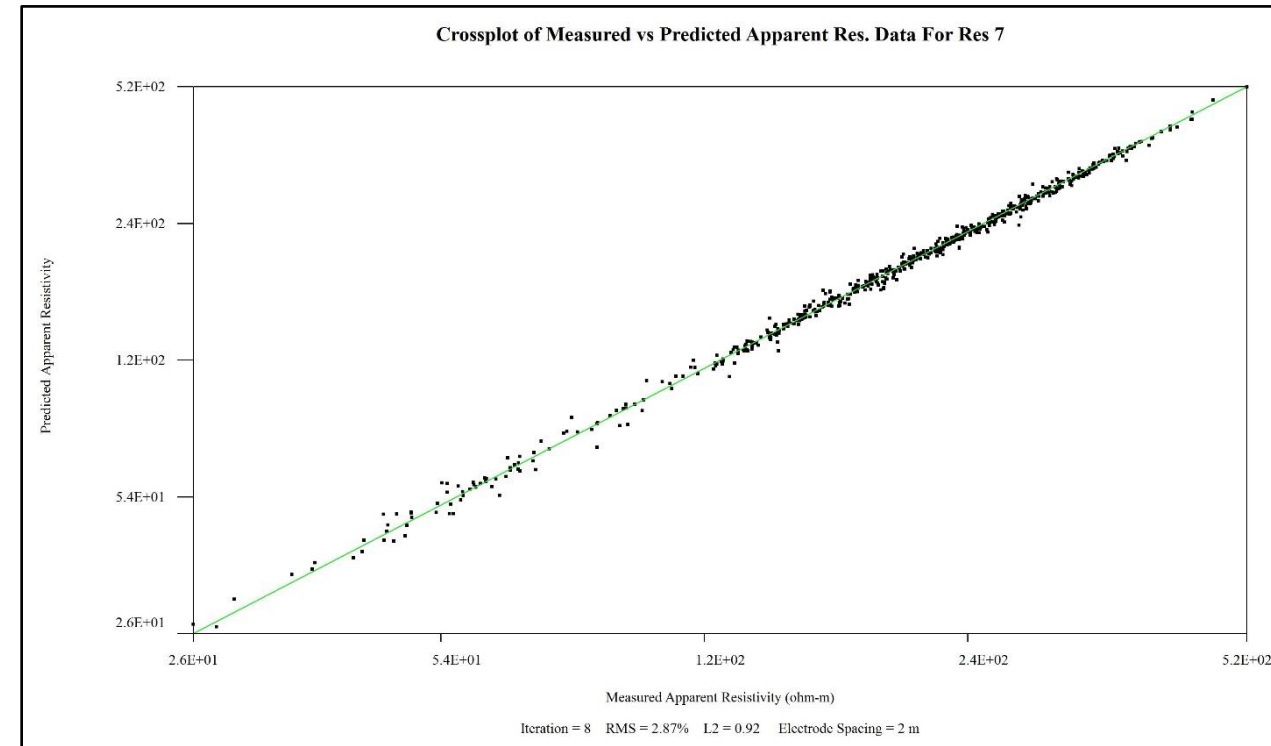
Vertical zones of lower resistivity likely associated with more significant fractures that provide cross communication pathways for fluids between upper and lower leached horizons. Differential leaching has resulted in irregular subsidence throughout this region of road.

Figure C18: Survey site Res5b_P09. 56 electrode dipole-dipole array with 2-meter spacing (total length 112 meters). Note that maximum resistivity reading in inverted sections is 100k ohm-m. RMS error 4.02%



Description:
 Leached gypsum at shallow depths highlighted by a zone of low resistivity. Less saturated gypsum at depth indicated by moderately high resistivity. Survey conducted on eastbound lane (4-meter spacing) with a survey length of 224 meters. Variable connectivity between upper and lower leached zones is not easily discerned because of resolution of data.

Figure C19: Survey site Res5b_P09. 56 electrode dipole-dipole array with 4-meter spacing (total length 224 meters). Note that maximum resistivity reading in inverted sections is 100k ohm-m. RMS error 6.96%. Survey conducted in eastbound lane.



Description:

Survey is located proximal to entrenched stream with thickening soil towards the northwest on margin of stream channel. Profile indicates increased moisture in soil regions with a sub-horizontal region of high permeability within bedrock. This permeable zone of bedrock likely indicates a horizon of minor leaching associated with local hydraulic gradient towards the stream.

Single isolated high resistivity region likely represents a small open solutional conduit proximal to the land surface. This feature probably exhibits limited hydraulic connectivity to the current hydrologic system.

Figure C20: Survey site Res7_P04. 56 electrode dipole-dipole array with 2-meter spacing (total length 112 meters). Note that maximum resistivity reading in inverted sections is 36.624 ohm-m. RMS error 2.87%



Description:

Resistivity line (Res4a_P02) was acquired with 4-meter spacing from west to east in the transitional zone between the Castile dominated gypsum plain to the Rustler Hills. Data indicate that secondary gypsum bodies occur beneath the road near sites of previous road failures. Data suggests that secondary gypsum bodies are dissolving and proximal surface soils are being piped into the void space created. Extreme low resistivity areas likely represent sulfate rich waters while surrounding region of moderate resistivity indicates zones of fractured Rustler limestone.

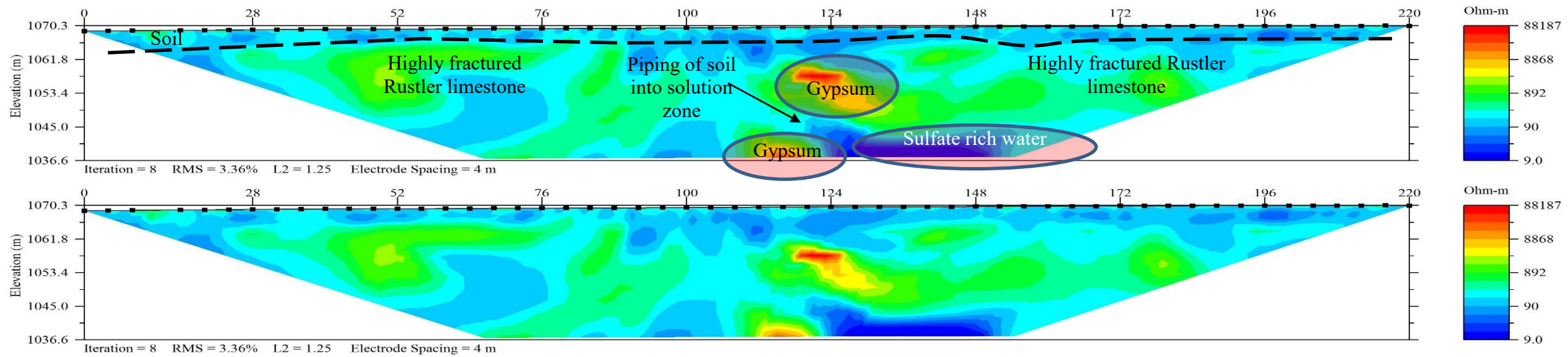
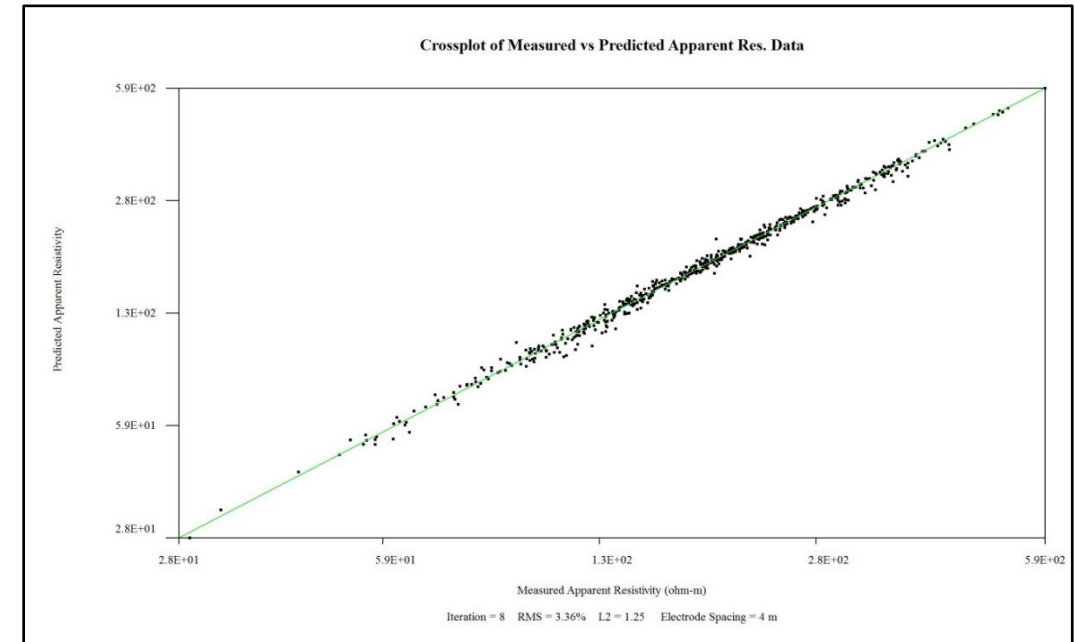
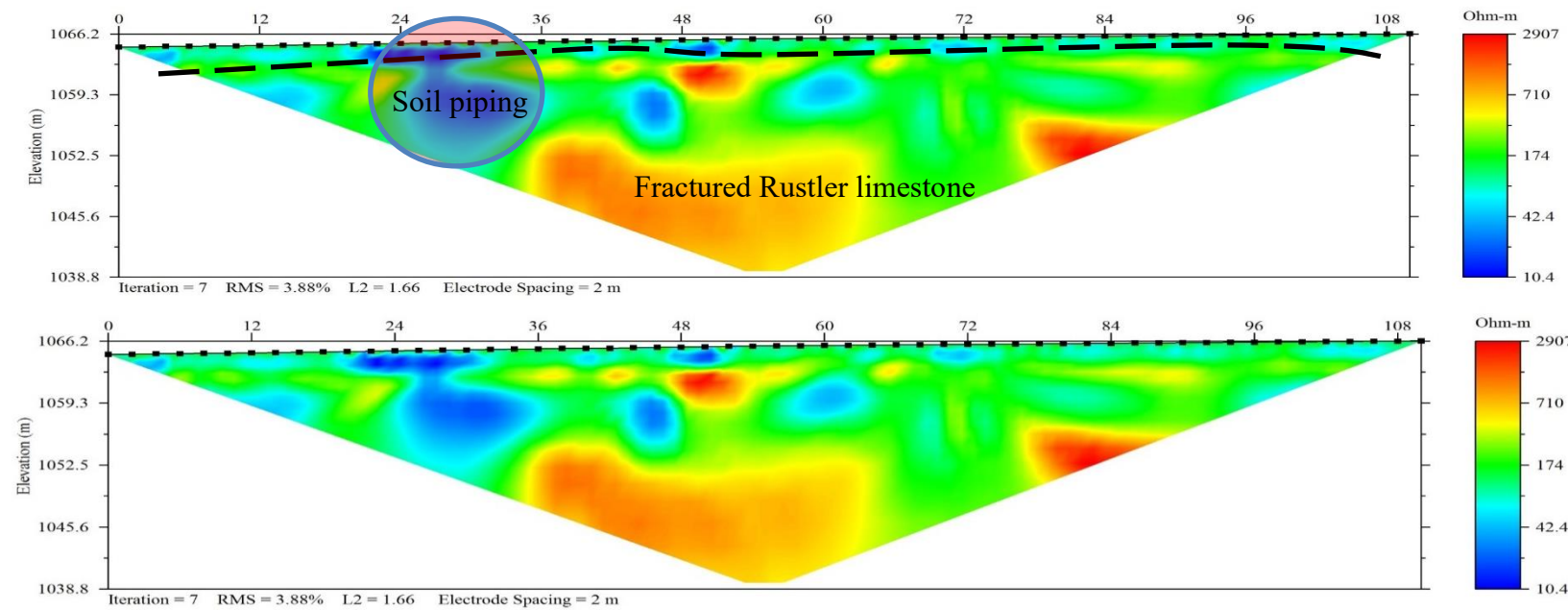
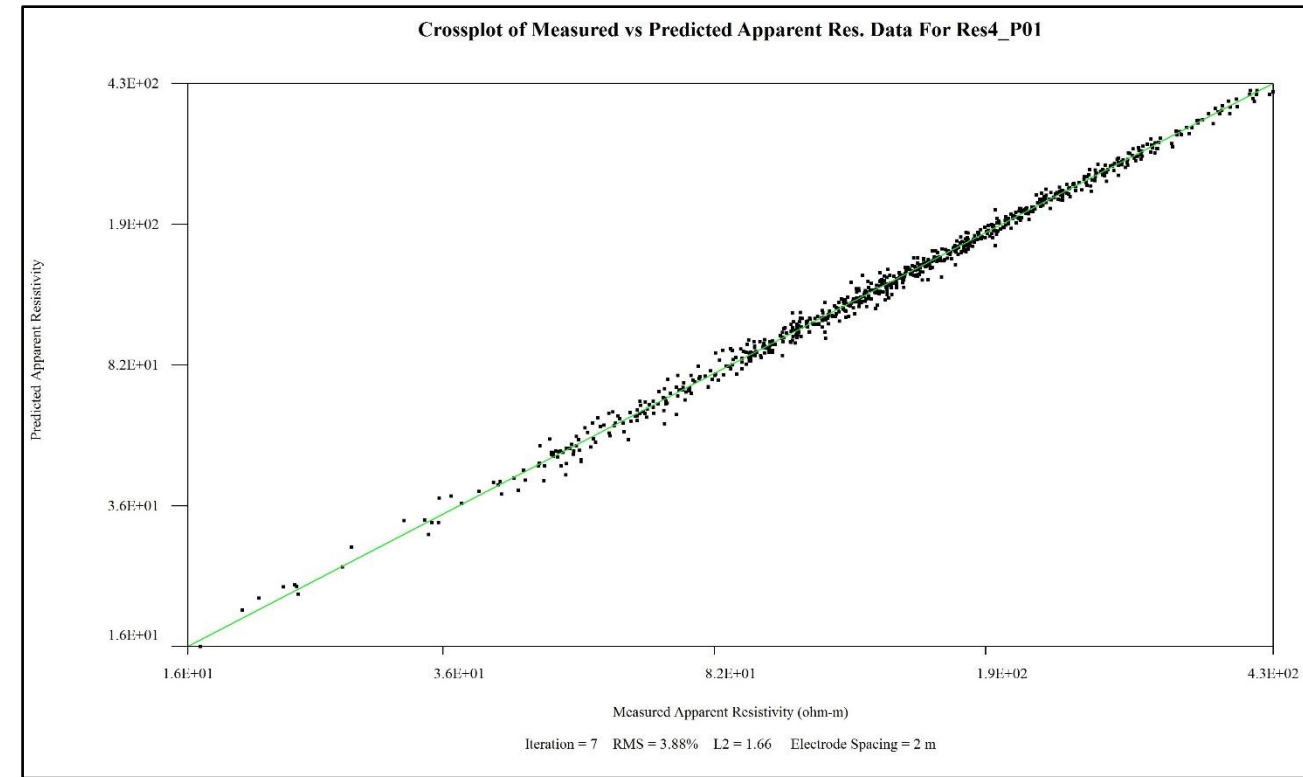


Figure C21: Survey site Res4a_P02. 56 electrode dipole-dipole array with 4-meter spacing (total length 224 meters). Note that maximum resistivity reading in inverted sections is 88,187 ohm-m. RMS error 3.36%



Description:

Site is located in region with thin soil over highly fractured Rustler limestone. Mid to high resistivity values in profile represent fractured rock with variable moisture content. Low resistivity regions appear to be areas of soil piping that retain greater moisture content. Piping is likely associated with solutional or fracture conduits at significant depth beyond the range of investigation.

Dashed line represents approximate boundary between soil and bedrock. Limited connectivity occurs between moisture rich soil and soil piping regions within fractured rock which limits surficial subsidence to isolated regions.

Figure C22: Survey site Res4_P01. 56 electrode dipole-dipole array with 2-meter spacing (total length 112 meters). Note that maximum resistivity reading in inverted sections is 2,907 ohm-m. RMS error 3.88%

VITA

Adam Majzoub graduated from Spring Woods High School in 2002 and attended Houston Community College soon afterwards. After deciding on a degree in earth sciences he attended the University of Houston and earned a Bachelor of Science in Geology in December of 2014 all while working part time as a waiter in a restaurant. In the fall of 2015 he was accepted at the Graduate School at Stephen F. Austin State University where he completed his Master of Science in Geology in December 2016.

Permanent Address: 1139 Murrayhill Dr
Houston, TX 77043

Style manual designation: Geological Society of America

This thesis was typed by Adam F. Majzoub